DYNAMICS OF THE SOLAR TACHOCLINE

Pascale Garaud

Trinity College
University of Cambridge

A dissertation
submitted for the degree
of Doctor of Philosophy at the
University of Cambridge
2000

Contents

DYNAMICS OF THE SOLAR TACHOCLINE

Preface

The work presented here is my original work except where specific reference is made to the work of others, and includes nothing which is the outcome of work done in collaboration.

Some of the work contained in this dissertation has been published, or is due to be published in refereed scientific journal. Material in Chapter 2 is going to be published in:

Garaud, P., 2001, *Latitudinal instability in the solar tachocline*, MNRAS, 2001, *in press*

Material in Chapter 3 has been published in:

Garaud, P., 1999, *Propagation of a dynamo field in the radiative interior of the sun*, MNRAS, **304**, 583-588

The material of Chapters 4 to 6 is being prepared for publication.

The summer of 1999 was spent participating in the Woods Hole Geophysical Fluid Dynamics Summer School (Woods Hole, MA). Aside from the lectures, I worked principally with Dr. G. Flierl on the subject of *Vortices in accretion disks*. This work was published in the proceedings of the summer school:

Garaud, P., Flierl, G. R. & Llewellyn-Smith, S. G., 1999, *Proceedings of the Woods Hole Geophysical Fluid Dynamics Summer School 1999*, ed. N. Balmforth, J.-L. Thieffault & C. Pasquero.

or can be found on **http://gfd.whoi.edu/proceedings/**

Acknowledgments

The work presented in this dissertation is the fruit of a little more than three years of the most exciting and delightful collaboration with my supervisor Douglas Gough. Douglas shared me with his exciting idea about the internal rotation of the sun, and entrusted me with the "formidable" task of developing it. I thank him for his trust, his patience, for his constant support and encouragements, for always leaving me all the freedom I needed to work at my own pace on the various subjects that would pique my interest, and yet always be there with an answer to all the problems I may encounter. And when occasionally he was not there, Nigel Weiss came to the rescue with his immense knowledge and experience of MHD problems; to Nigel also I am deeply grateful, and I look forward to continue working with both of them on the subject of the solar rotation.

This work would never have been possible without the financial support of PPARC, the Isaac Newton Trust, Trinity College and New Hall; they have all my gratitude, the results presented in this dissertation is their reward.

To my work colleagues, both in Cambridge and in Woods Hole I owe my thanks, and a lot of very good times. Takashi, Gunter, and Marc, Steve, Alastair at DAMTP, thank you for all the very fruitful discussions and for never losing your patience with me when I ask trivial questions. A strange complicity developed between me and my fellow students, Marcus, Margarida and Chris, and the secretaries, Jane, Anne and Di, through the sharing of tips on how to get hold of Douglas - thanks to all of them for helping me through this difficult task. And of course, I'll never forget Muon and her warm company.

A few years of my life were spent working on this dissertation. They saw the evolution of my scientific mind, but also the shaping of my character and personality. Through the best moments and the worse ones, through everyday's routine and events that changed my life, a few people were always around me, and for this I shall forever cherish the memory of these years. And through them I learnt so many things too: from my office-mate Mike, a lot about how men think, from Mukund, that vegetarian food can be so delicious. With my volleyball teams, I learnt (the hard way) everything about patience, stress and dealing with people – so my thoughts go to Jon for his help and encouragements throughout this last season. In Woods Hole, with David, Roberto, Claudia, George, Jean-Luc and all the others, I discovered just how good life – and work – can get. Thanks also to Russell, for always begin there to help me with my computer, and for great out-of-Cambridge experiences. And to the best of friends, Bong, Helen, Alex, Carl, Marta, thanks for sharing with me love and friendship, good wine, good times, and parts of your lives.

Finally, I thank my family. Despite the distance I know that my parents are always behind me and support my choices and my work, especially with endless supplies of french chocolate, BDs, and Christmas cookies. I hope one day they will find the time to visit Cambridge. And to JD, mon p'tit frère who grows more everyday, all my love. May this dissertation show him that doing a PhD can be a lot of fun.

Chapter 1

The rotating sun

As the predictions of days and seasons became essential to the development of civilization through agriculture, humanity started looking up to the sun less as a "god" and more as an object of science. Stone alignments at Carnac (France) are some the most ancient examples of solar studies in western civilization. Until only recently, the study of the sun beyond the prediction of its motion through the sky was often considered sacrilegious. Anaxagoras, around 430 BC, was exiled for suggesting (amongst other revolutionary ideas) that the sun was just a ball of fire, and evaluating its distance to be about 4000 miles from the surface - his insightful geometric analysis being flawed only by his belief that the earth was flat. Three hundred years later, Hipparchus set the first lower limit on the distance of the sun to the earth by trying to measure its parallax and failing to get an accurate measurement. He was the first to suggest, however, that the sun may be a very large distance away, and that its radius was correspondingly much larger than previously thought. The next fundamental discoveries concerning the sun waited seventeen centuries, the invention of the telescope and the theory of gravitation. In 1752, the French astronomer Lacaille used the transit of Venus across the solar surface as another parallax measurement and obtained the first reasonably accurate measurement of the distance of the sun. Using the theory of gravitation and the first measurements of the gravitational constant G carried out by Cavendish, the mass of the earth and consequently the mass of the sun were then determined for the first time.

Having determined the most "obvious" characteristics of the sun, scientists turned to the problem of energy production. It was soon realized that no chemical reaction in the solar material could provide

enough energy at the observed rate for any significant length of time. Kelvin and Helmholz suggested that the energy released by gravitational contraction could somehow be turned into heat, and provide the observed luminosity: they calculated that such a system would radiate for about 10^7 years. This timescale seemed satisfactory in the nineteenth century, but more recent estimates of the age of the earth and the solar system invalidated their theory. The final step towards our modern view of the sun was taken by Eddington (1926) who for the first time stated that the energy generation in the sun was principally due to the nuclear burning of hydrogen into helium (and subsequently to iron). From this point onwards, with the foundations of solar physics clearly laid out, there remained the task to gather all the necessary tools to construct the first global models of our sun.

1.1 A PHYSICAL VIEW OF THE SUN

The stepping-stones of the standard solar models are the following: the sun is a self-gravitating mass of gas (whose value $M_\odot$ is observationally determined), which produces energy through nuclear fusion within its core. Pressure gradient and gravitational attraction cancel at every point in the sun. Energy is transported radiatively or convectively towards the surface to yield the observed surface luminosity and radius. In order to model this more quantitatively, to a first approximation, the effects of rotation on its hydrostatic structure are neglected. Within this approximation, the sun can be considered to be spherically symmetric, and the equations of stellar evolution reduce to a simple set of evolution equations:

1. the hydrostatic structure equation:

$$\frac{\partial p_{\rm h}}{\partial r} = -\rho_{\rm h} \nabla \Phi_{\rm h} \ , \tag{1.1}$$

where $p_{\rm h}$ is the hydrostatic equilibrium pressure, and

$$\nabla^2 \Phi_{\rm h} = 4\pi G \rho_{\rm h} \ , \tag{1.2}$$

where G is the gravitational constant, and $\rho_{\rm h}$ is the local mass-

density of the fluid. This equation does not assume anything about the origin of the pressure, which can be due to gas-pressure, or turbulent pressure (in particular in the surface layers). This equation does not have an explicit time dependence: sound waves propagate through the sun in a few hours, and ensure that the hydrostatic equilibrium equation is always instantaneously satisfied.

2. the energy transport equation:

$$\frac{L_{\rm h}}{4\pi r^2} = F_{\rm rad} + F_{\rm conv} \ , \tag{1.3}$$

where L is the total luminosity generated within the sphere of radius r, and F is the energy flux through the sphere of radius r. The heat flux depends essentially on the principal mechanisms for heat transport at radius r. In a convectively stable region, heat is transported by photons; these have a short mean free path and are often absorbed and re-emitted by atoms in the gas. The heat flux therefore depends strongly on the temperature and density of the gas, (which determine the collision rates) and the atomic properties of the atoms (which determine the energy spectrum of the radiated photons). Assuming local thermodynamic equilibrium, the radiative heat flux can be rewritten as

$$F_{\rm rad} = -K_{\rm t} \frac{\partial T_{\rm h}}{\partial r} \ , \tag{1.4}$$

where $K_{\rm t}$ is the heat conductivity, and $T_{\rm h}$ the temperature. The heat diffusivity depends on the local properties of the gas through

$$K_{\rm t} = \frac{16\sigma_{\rm B} T_{\rm h}^3}{3\kappa\rho_{\rm h}} \ , \tag{1.5}$$

where $\sigma_{\rm B}$ is the Stefan-Bolzman constant and κ is the Rosseland mean opacity, which is obtained from atomic physics. When the local radiative heat flux is not sufficient to transport all the energy, a convective instability sets in which easily transports most of the heat to larger radii. Standard models of the convec-

tive heat flux are usually based on mixing length theory. Again, there is no explicit time dependence in this equation, as the heat transport timescale is much smaller than the nuclear generation timescale.

3. the energy generation equation

$$\frac{\partial L_{\rm h}}{\partial r} = 4\pi r^2 \rho_{\rm h} \left(\epsilon - T_{\rm h} \frac{\partial S}{\partial t} \right) \ , \tag{1.6}$$

where ϵ is the nuclear energy generation rate and S the entropy. Energy is principally generated by nuclear burning, which depends on the local temperature, density, chemical abundances, etc... The complex relation

$$\epsilon = \epsilon(\rho_{\rm h}, T_{\rm h}, X, Y, Z, ...) \ , \tag{1.7}$$

is obtained from nuclear physics.

4. the equation of state

$$p_{\rm h} = p_{\rm h}(\rho_{\rm h}, T_{\rm h}, X, Y, Z, ...) \ , \tag{1.8}$$

is extremely complex, as it results both from atomic effects and plasma effects. In particular, in the core regions relativistic effects and non-ideal gas effects (such as electron screening) come into play. The gradual ionization of all elements in the sun must be taken into account in the calculation of the mean molecular weight. In the convection zone and in surface layers in particular, the contribution of turbulent motions to the pressure must also be taken into account.

5. and finally a large number of equations of evolution for the abundances of chemical elements, as they are created or destroyed by nuclear reactions, and as they settle gravitationally with respect to one another.

Despite the complexity in the physics involved in deriving the model equations, the resolution of those equations is comparatively simple.

A "zero-age" main sequence model, which usually consists of a star with uniform initial chemical composition (X_0, Y_0, Z_0), can be evolved in time straightforwardly until the present age of the sun is reached, and the model parameters (such as initial element abundances, mixing length models) are varied until all observable quantities can be reproduced (luminosity, radius, etc...). The final solution yields a full present-day structure of a non-rotating sun-like star. Aside from the neutrinos flux measurements, however, first models of the sun had very little observational data with which to compare the numerical predictions. In particular, uncertainties in the models for convection, for instance, resulted in a large degeneracy of the possible solutions. These problems were soon overcome, however, with the development of a new powerful tool for observation of the *interior* of the sun: helioseismology.

1.2 A new observational method: helioseismology

In 1960, oscillatory motions were discovered in the upper atmosphere by measuring the variation in the Doppler shift of the spectral line Ba II (see Leighton et al. 1962). With a dominant period of roughly 5 minutes, the spectrum of these oscillations was subsequently found to be discrete, leading to the conclusion that these oscillations are trapped within a resonant cavity in the sun. These oscillations are predominantly sound waves, *p-modes*, excited near the surface by the turbulent motions of the convection zone. It was soon realized that the observations of these oscillations, and in particular of their frequencies, could provide information about the internal structure of the sun.

1.2.1 Elements of helioseismology

Waves trapped in a resonant cavity have a discrete frequency spectrum which depends essentially on the travel time between various points on the surface of the cavity, which in turn depends on the sound speed at all points. It is through the analysis of the wave equation that the relation between observed frequencies and the sound speed everywhere in the sun can be obtained. For the purpose of simply describing the

helioseismic method, it is sufficient to show a simplified derivation of the linearized adiabatic wave equation.

The equations for hydrostatic support describe the background stratification of the sun. The interaction with sound waves is described by perturbing the stellar structure equations and introducing the equations of motion. When the amplitude of the oscillations is small these equations can be linearized. The resulting linearized perturbation equations, when the fluid is undergoing a displacement field $\boldsymbol{\xi}$, are

$$\rho_{\rm h}\frac{\partial \boldsymbol{u}}{\partial t} = -\nabla p' - \rho'\nabla\Phi_{\rm h} - \rho_{\rm h}\nabla\Phi' \ , \tag{1.9}$$

$$\nabla^2\Phi' = 4\pi G\rho' \ , \tag{1.10}$$

where the quantities denoted by primes are Eulerian perturbations (i.e. perturbations to the background value at a fixed point). The velocity field $\boldsymbol{u}$ is related to the displacement field by

$$\boldsymbol{u} = \frac{\partial \boldsymbol{\xi}}{\partial t} \ , \tag{1.11}$$

which implies that the linearized mass conservation equation becomes

$$\rho' + \nabla\cdot(\rho_{\rm h}\boldsymbol{\xi}) = 0 \ . \tag{1.12}$$

Finally, the oscillations are assumed to be adiabatic (i.e. that no heat is gained or lost by displaced parcels of fluid during their motion), which implies that

$$\delta p = \Gamma_1\delta\rho = c_{\rm h}^2\delta\rho \ , \tag{1.13}$$

where δ denotes a Lagrangian perturbation (i.e. following the fluid), $c_{\rm h}^2$ is the hydrostatic sound-speed, and the first adiabatic exponent Γ_1 is given by

$$\Gamma_1 = \left(\frac{\partial p}{\partial \rho}\right)_s \ , \tag{1.14}$$

the derivative being taken at constant entropy s. The relation between the Eulerian and Lagrangian perturbation of a quantity f is

$$\delta f = f' + \boldsymbol{\xi} \cdot \nabla f_{\rm h} \ . \tag{1.15}$$

Combining equations (1.9) to (1.15) yields a unique differential relation for the displacement $\boldsymbol{\xi}$. Assuming that $\boldsymbol{\xi}$ varies as $\tilde{\boldsymbol{\xi}} e^{i\omega t}$ yields

$$-\omega^2 \rho_{\rm h} \tilde{\boldsymbol{\xi}} = -\nabla p' - \rho' \nabla \Phi_{\rm h} - \rho_{\rm h} \nabla \Phi' \ . \tag{1.16}$$

This equation can be solved subject to suitable boundary conditions to obtain the eigenfrequencies ω, which depend on the hydrostatic structure of the sun through the sound-speed $c_{\rm h}$. Separability of the displacement equations in the coordinates (r, θ, ϕ) implies that scalar quantities can be represented as

$$\psi_{nlm} = A_n(r) P_l^m(\theta) \, \cos(m\phi - \omega_{nlm} t) \ , \tag{1.17}$$

where $\psi \propto \nabla \cdot \tilde{\boldsymbol{\xi}}$ for instance.

Observations of the oscillations of the solar surface are carried out through intensity measurements (by the VIRGO photometers on board SOHO, for instance) or velocity measurements (Doppler shifts measurements on several photospheric lines, realized by the GONG and BiSON ground networks, or the MDI instruments on board SOHO for example). The inversion process, which consists in using the measured oscillation frequencies ω_{nlm} to infer the interior characteristics of the suns has been reviewed in detail by Gough (1985).

1.2.2 Helioseismic results derived from sound-speed inversions

The principal achievements of helioseismology using the sound-speed inversion methods described previously are the following:

1. the determination of the sound-speed (and hence the temperature) profile throughout the whole interior, which allows the calibration of the solar age, initial helium abundance (see the

review by Gough et al. (1996) for instance), and more specifically the microphysics of the solar models, such as the equation of state (e.g. the review by Däppen & Nyafonov, 2000), the opacities (Tripathy & Christensen-Dalsgaard, 1998) and the thermonuclear reaction rates (Morel et al. 1999, for example).

2. the measurement of the depth of the convection zone (e.g. Christensen-Dalsgaard et al. (1991)), which allows a preliminary calibration of convective mixing-length models. A careful analysis of the effect of convection dynamics on oscillation properties enabled Houdek et al. (2001) to calibrate mixing length models further with line-width measurements of the BiSON group (Chaplin et al. 2000).

3. the calibration of overshoot depth (Basu, 1997), which use the effect of sharp gradients of the sound speed on the acoustic frequencies.

4. an independent measurement of the solar radius, by looking at the size of the acoustic cavity of the oscillation modes (Schou et al, 1997).

Using all the helioseismic inversions, it is possible to build, for example, a solar model which provides the best possible fit to the observed sound-speed profile. The remaining discrepancy for the square of the sound speed, between the model and the observations, is shown in Fig. 1.1. Note how the discrepancies never exceed a few parts in a thousand. This extremely good fit shows that the standard solar models satisfactorily reproduce the physics of the solar interior. However, the error bars on the observed sound speed are much smaller than the remaining discrepancies, which suggests that additional information can be obtained from the sound speed inversion, and that the discrepancies truly represent a failure of the models, either in the initial assumptions, or in the micro- or macrophysics used. Failures in the microphysics may be due to inaccurate representations of the equation of state, the nuclear burning rates, or the opacities. Failure in the macrophysics may be due to insufficient understanding of convection, or surface effects. Finally, as it was pointed out initially by Elliott &

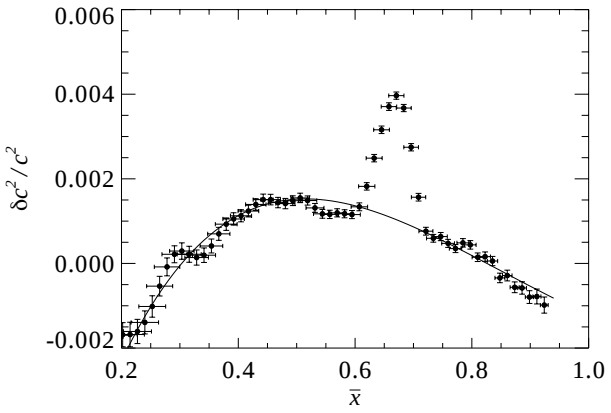

Figure 1.1: Difference between the model predictions and the observations for the square of the sound speed, as a function of radius. The vertical errorbars are derived from the errors on the data, whereas the horizontal errorbars represent the average width of the inversion kernels at the corresponding radius.

Gough (1999), part of the discrepancy with the observations may be due to some of the fundamental assumptions made in the standard solar models: the one which consists in neglecting all fluid motions in the sun, and in particular the rotation.

1.3 The solar rotation

The first published measurements of the solar rotation were performed by Carrington (1863), using the apparent motion of sunspots across the surface of the sun (Gallileo had already noted the drift of sunspot across the solar surface). Carrington hereby measured the inclination of the axis of rotation of the sun with respect to the ecliptic plane. Later, a similar technique was used to measure the variation of the solar surface rotation rate with latitude (Newton & Nunn (1951)). The results are usually represented in the following way:

$$\Omega(\theta) = \Omega_{\rm eq}(1 - a_2 \cos^2\theta - a_4 \cos^4\theta) \ , \ , \tag{1.18}$$

where Ω is the local angular velocity, θ is the colatitude and $\Omega_{\rm eq}$ is the equatorial angular velocity. Newton & Nunn's results (and other subsequent investigations) suggested that

$$\Omega_{\rm eq} \approx 2.89 \times 10^{-6} \text{ rad/s and } a_2 \approx 0.19 \ , \tag{1.19}$$

while a_4 remained undetermined through this method. Indeed, this coefficient can only be determined by careful observations of the rotation rate near the poles, a region where few sunspots ever appear. Measurements of the Doppler shift of photospheric emission near the limb (Snodgrass (1984)) suggest that

$$\Omega_{\rm eq} \approx 2.83 \times 10^{-6} \text{ rad/s} \ , a_2 \approx 0.1 \text{ and } a_4 \approx 0.18 \ . \tag{1.20}$$

Note the difference with the coefficients measured previously. These new measurements seem to suggest a rather faster rotation rate for the sunspots (near the equator) than that of the photosphere; this was attributed to a faster rotation rate at the depth from which the sunspots originate, a result which was later confirmed by helioseismic observations.

1.3.1 Development of rotational inversions

Only helioseismology can provide information on the internal rotational structure of the sun. The theory of stellar oscillations in a differentially rotating star was developed initially by Ledoux & Pekeris (1941), Cowling & Newing (1948) and Lynden-Bell & Ostriker (1967). Again, the full derivation of the theory is beyond the scope of this introduction, so only a simplified derivation which nonetheless captures the essential points is presented. For a comprehensive review of the subject, see the paper by Gough & Thompson (1991).

1.3.1.1 Perturbation equation in differentially rotating background

Assuming that the system is rotating with an angular velocity which depends on latitude and radius $\Omega(r,\theta)$. The velocity perturbation due to this azimuthal flow is now included in the perturbation, so that

$$\boldsymbol{u} = \boldsymbol{v}' + (\boldsymbol{\Omega} \times \boldsymbol{r}) \ , \tag{1.21}$$

where $\boldsymbol{\Omega} = \Omega(r,\theta)\hat{\boldsymbol{e}}_z$ and $\boldsymbol{v}'$ corresponds to the velocity perturbation due to the wave part only:

$$\boldsymbol{v}' = \frac{\mathrm{D}\boldsymbol{\xi}}{\mathrm{D}t} \ . \tag{1.22}$$

The operator $\mathrm{D}/\mathrm{D}t$ is now modified to take into account the advection of the perturbation by the azimuthal motion of the flow so that, for example:

$$\frac{\mathrm{D}\boldsymbol{\xi}}{\mathrm{D}t} = \frac{\partial \boldsymbol{\xi}}{\partial t} + \left[(\boldsymbol{\Omega} \times \boldsymbol{r}) \cdot \nabla\right] \boldsymbol{\xi} \ . \tag{1.23}$$

Putting equations (1.21) to (1.23) together with (1.9) yields

$$\rho_\mathrm{h} \frac{\partial^2 \boldsymbol{\xi}}{\partial t^2} + 2\rho_\mathrm{h} \left[(\boldsymbol{\Omega} \times \boldsymbol{r}) \cdot \nabla\right] \frac{\partial \boldsymbol{\xi}}{\partial t} = -\nabla p' - \rho' \nabla \Phi_\mathrm{h} - \rho_\mathrm{h} \nabla \Phi' \ . \tag{1.24}$$

The displacement equations are now slightly modified with the addition of a Coriolis force term $2\rho_\mathrm{h} \left[(\boldsymbol{\Omega} \times \boldsymbol{r}) \cdot \nabla\right] \frac{\partial \boldsymbol{\xi}}{\partial t}$.

1.3.1.2 Correction to the eigenfrequencies due to the effect of rotation

Instead of recomputing the full solutions of equation as well as their eigenfrequencies, it is easier to compute the correction to the eigenfrequencies deduced from (1.24) due to the rotation. In the non-rotating case, the eigenfrequencies follow the equation

$$-\omega^2 \boldsymbol{\xi} = \mathcal{F}(\boldsymbol{\xi}) \ . \tag{1.25}$$

If $\delta\omega$ is the correction due to the rotation then

$$-(\omega + \delta\omega)^2 \boldsymbol{\xi} = \mathcal{F}(\boldsymbol{\xi}) + \delta\mathcal{F}(\boldsymbol{\xi}) \ , \tag{1.26}$$

where

$$\delta\mathcal{F}(\boldsymbol{\xi}) = -2i\omega\rho_{\rm h} \left[(\boldsymbol{\Omega} \times \boldsymbol{r}) \cdot \nabla\right] \boldsymbol{\xi} \ , \tag{1.27}$$

is assumed to be a small perturbation on the non-rotating system. Since the solutions to equation (1.16) form an orthogonal basis, the corrections to the eigenfrequencies can be obtained by projecting (1.27) onto that basis, and using the variational principle, so that (Ledoux, 1951)

$$\delta\omega = i \frac{\int_V \rho_{\rm h} \boldsymbol{\xi}^* \left[(\boldsymbol{\Omega} \times \boldsymbol{r}) \cdot \nabla\right] \boldsymbol{\xi} {\rm d}V}{\int_V \boldsymbol{\xi}^* \boldsymbol{\xi} {\rm d}V} \ , \tag{1.28}$$

which can also be rewritten as, for the frequency splitting $\delta\omega_{nlm}$

$$\delta\omega_{nlm} = \int_0^{r_\odot} \int_0^{\pi} K_{nlm}(r,\theta) \Omega(r,\theta) r {\rm d}r {\rm d}\theta \ , \tag{1.29}$$

1.3.1.3 Inversion methods

There exist many currently used methods of inversion for the rotational splittings, which can roughly be grouped into two categories: the least-squares fitting methods, and the localized averaging methods.

Least square fitting methods work typically by calculating the frequency splittings corresponding to a piecewise bilinear angular velocity profile in a regular grid in the (r, θ) plane, and fitting them to the

observed splittings with a χ^2 minimization method. The χ^2-algorithm incorporates a penalty function to moderate the error in the fitting whilst penalizing profiles with large second derivatives in radial or latitudinal coordinates. This method was described in detail by Schou, Christensen-Dalsgaard & Thompson (1994).

The principle of the optimized localized averaging methods (OLA) is based on the fact that the frequency splittings are an average of the true rotation profile weighted by the kernel K_{nlm}. As a result, a judicious choice of a linear combination of the frequency splittings can yield a *localized* average of the true rotation profile provided the same linear combination of the kernels K_{nlm} yields a localized kernel:

$$< \Omega(r_0, \theta_0) >= \int_0^{r_\odot} \int_0^{\pi} K(r, r_0, \theta, \theta_0) \Omega(r, \theta) r \mathrm{d}r \mathrm{d}\theta \ , \tag{1.30}$$

where $K(r, r_0, \theta, \theta_0)$ is a function strongly peaked around the values of r_0 and θ_0, such that

$$K(r, r_0, \theta, \theta_0) = \sum_{nlm} a_{nlm} K_{nlm}(r, \theta) \ . \tag{1.31}$$

If such a function is found, then

$$< \Omega(r_0, \theta_0) >= \sum_{nlm} a_{nlm} \delta\omega_{nlm} \ . \tag{1.32}$$

It is beyond the scope of this introduction to discuss how the coefficients a_{nlm} are computed; for more detail the reader is referred to Gough & Thompson (1991).

1.3.2 Results

The first attempt at determining the interior angular velocity profile of the sun from rotational splittings was performed by Duvall et al. (1984) using the frequency splittings measured by Duvall & Harvey (1984). Schou et al. (1998) present recent measurements of the solar differential rotation with good accuracy and good spatial resolution

down to radii of about 0.6 $r_\odot$ and up to latitudes of about 70°. These are shown in Fig. 1.2. Four inversion methods are compared in this plot, using essentially the two different methods described in Section 1.3.1.3. These inversions call for the following comments:

1. the least-squares minimization methods provide relatively good spatial resolution, but are strongly affected by errors in the observational data, as well as the poor representation of the oscillations in the outer layers of the sun. There exist strong evidence that additional features, such as the "polar jet", could simply be artefacts of the inversion (Howe et al. 2000a).

2. the optimized localized averages methods tend to be free of such undesirable effects, but suffer from poorer spatial resolution than the least-square minimization methods.

Despite their intrinsic differences, the common features of the inversions which are therefore likely to be intrinsic to the true rotation profile are the following:

1. the convection zone is observed to undergo latitudinal shear, with little radial shear

2. the radiative zone is rotating nearly uniformly, with an angular velocity of about 93.5 % of the equatorial angular velocity

3. a thin shear layer separates these two zones: the solar *tachocline*

1.4 The solar tachocline

The solar tachocline is a very shallow shear layer located just below the base of the solar convection zone, in the convectively stable region. The convection zone imposes a latitudinal shear to the radiative zone, but this shear is observed to be quenched within a very short distance, leaving the radiative zone in a state of nearly uniform rotation. The resulting radial shear layer is the tachocline. It was first observed by Brown *et al* (1989). The terminology to describe this shear layer was first used in its present form by Spiegel & Zahn (1992), who constructed the word from the Greek roots $\tau\alpha\chi o\varsigma$ *tacho-*

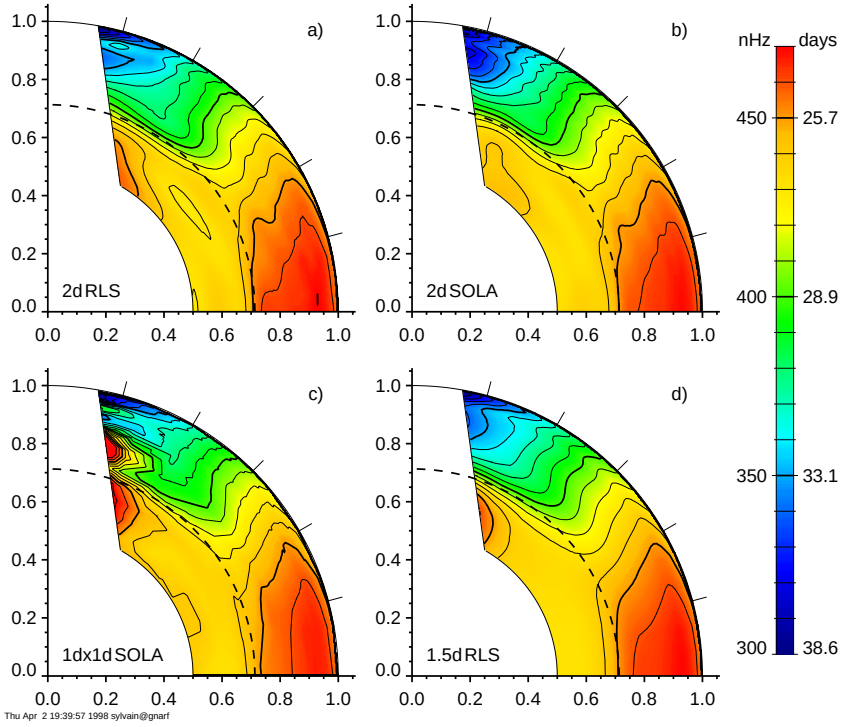

Figure 1.2: Inversion results for the angular velocity $\Omega/2\pi$ with radius and latitude, for 4 inversion methods. The dashed circle indicates the base of the convection zone, and the tick marks at the edge of the outer circle are at latitudes 15°, 30°, 45°, 60°, 75°. In such a display, the equator is the horizontal axis, and the pole the vertical axis, with the proportional radius labeled. The white area indicates the region in the sun where no reliable inference can be made with the current data. (Schou et al., 1998).

(velocity) and $\kappa\lambda\acute{\iota}\nu\epsilon\iota\nu$ *-cline* (turn, bend). Because of its intrinsic nature (i.e. a shear layer) and also because of its location (just below the convection zone, in a region of transition between two radically different backgrounds), the tachocline is the seat of some of the most interesting and complex phenomena occurring in the sun. It is therefore essential to gather as much observational information as possible concerning this region before attempting to model it.

1.4.1 Thickness of the solar tachocline

The determination of the thickness of the solar tachocline, Δ, still remains a controversial subject. Inversion methods yield (more or less) local averages of the angular rotation rate over a finite area which increases strongly with depth. In the region of the tachocline, the best inversions yield averages over a radial width of about 4% of the solar radius; the observations of the differential rotation can therefore not provide any direct reliable estimate of the width of the tachocline. Methods have been designed, in which a "profile" is guessed for the tachocline (i.e. an ansatz for the variation of the angular velocity with depth is chosen), and is then convoluted with the same averaging kernels that have been used for the inversions. Comparison of the convoluted profile with the inversions may provide a fairly reliable estimate of the width of the tachocline. The results are the following:

$$\begin{aligned} \Delta &\approx 0.05 r_\odot \pm 0.03 r_\odot \text{ (Corbard } et \text{ } al.\text{(1998)} \quad , \\ \Delta &\approx 0.05 - 0.1 r_\odot \text{ (Schou } et \text{ } al. \text{ (1998)} \quad . \end{aligned} \tag{1.33}$$

One can notice, however, the large error-bars on the results, which originate from the low resolution of the observations in that region.

A new indirect method has been suggested by Elliot & Gough (1999). Assuming the tachocline is in dynamical equilibrium, it can be shown (cf. later) that a large-scale circulation must exist in the tachocline, mixing chemical elements as well as angular momentum. This circulation becomes vanishingly small in the radiative zone. The overturning timescale is much smaller than the solar evolution timescale, so that the mixing can be assumed to be instantaneous. Elliot &

Gough showed that the mixing in the solar tachocline locally prevents the gravitational settling of helium, which results in a higher sound speed beneath the convection zone than what could be expected from standard solar models. This local discrepancy is indeed observed in the sound-speed data shown in Fig. 1.1. Comparison between a new model, which includes additional mixing below the convection zone over a depth Δ with the observations then yields the thickness of the mixed region, namely

$$\Delta = 0.019 r_\odot \pm 0.001 r_\odot \ . \tag{1.34}$$

The better quality of these results compared to those obtained previously originates from the fact that sound-speed inversions have much higher spatial resolution than the rotational splittings inversions. However, this result is highly dependent on the assumption that the tachocline is spherically symmetric. If its general shape deviates from a spherical shell whilst retaining the same thickness everywhere, the method overestimates the thickness of the tachocline by yielding an answer that is more related to the total deviation from a spherical shape than the true thickness. On the other hand, if the tachocline is more or less spherical but with large variation in thickness the method provides an estimate of the average width of the tachocline.

1.4.2 Position and shape of the solar tachocline

Recent interest has been given to the study of the position and shape of the solar tachocline; in particular, whether there exists a latitudinal variation of the position and width of the tachocline and whether the tachocline penetrates into the convection zone or not. Charbonneau et al. (1999) propose the following ansatz for the angular velocity throughout the sun

$$\begin{aligned} \Omega(r,\theta) &= \Omega_{\rm c} + \frac{1}{2}\left[1 + {\rm erf}\left(\frac{2(r - r_{\rm t}(\theta))}{\Delta(\theta)}\right)\right] \times \\ &\quad \left[\Omega_{\rm eq}(1 - a_2\,\cos^2\theta - a_4\,\cos^4\theta + b_1 r\,\sin\theta) - \Omega_{\rm c}\right] \end{aligned} \tag{1.35}$$

where Ω_c is the interior angular velocity, $\Delta(\theta)$ is the thickness of the tachocline, and $r_t(\theta)$ is the location of the centre of the tachocline. Both Δ and r_t may vary with latitude. By convoluting this expression with the inversion kernels, and comparing the results with the corresponding inversions, Charbonneau et al. obtain the following results:

1. the interior angular velocity is measured to be about

$$\frac{\Omega_c}{2\pi} = 430 \text{ nHz} \quad , \tag{1.36}$$

2. there is no statistically significant variation of the thickness of the solar tachocline; the thickness deduced from this method is

$$\Delta = 0.040 r_\odot \pm 0.013 \ , \tag{1.37}$$

3. there is a statistically significant variation of the position of the centre of the tachocline:

$$r_t(\text{ equator }) = 0.693 \pm 0.002 r_\odot \ , \tag{1.38}$$

$$r_t(\text{ latitude } 60^\circ) = 0.717 \pm 0.003 r_\odot \ , \tag{1.39}$$

   which seems to imply that the tachocline may be slightly prolate. Also, these results may suggest that part of the tachocline, in particular near the poles, lies in the convection zone (the base of the convection zone has been estimated to lie at a radius of $r_c = 0.713 r_\odot$, by Christensen-Dalsgaard et al. (1991)).

These results are consistent with earlier inference that the base of the convection zone might be prolate (Gough & Kosovichev, 1995). However, these results should be accepted with care: there is significant degradation of the spatial resolution with increasing latitude and depth. Once again, one can point out that such a method could not possibly resolve a tachocline of thickness lower than about $0.04 r_\odot$, hence the values described above; also, the observed increase in the radius of the centre of the tachocline with latitude may also be an artefact of the poor resolution near the poles.

1.4.3 Variability of the solar tachocline

After four years of nearly continuous observations with MDI on board SOHO, and with the GONG project, there are finally enough data to study the temporal variations of the solar differential rotation. Dynamical variations near the base of the convection zone have been studied by Howe et al. (2000b). The authors looked for temporal variations in the residuals between the observed rotation profile and a time average of the rotation profile over the past four years, at two different radii ($r = 0.63 r_\odot$ and $r = 0.72 r_\odot$) and three different latitudes (0°, 30° and 60°). They observed a statistically significant oscillation with an unexpected period of 1.3 yr, at both radii on the equator (0°) with anti-correlated phases. This could be associated with the presence of torsional oscillations in that region. No statistically significant oscillation was detected at higher latitudes. Again, this oscillatory feature could also be an artefact of the inversions.

1.4.4 Light-element abundances

The convection zone (and the tachocline) thoroughly mix chemical elements on a timescale much smaller than the nuclear evolution timescale. As a result, the abundances of chemical elements observed at the surface of the sun are constant throughout the convection zone down to the bottom of the tachocline. The observed depletion (or presence) of certain chemical elements (such as lithium, beryllium and boron) at the surface set strong constraints on the depth of the solar tachocline. The ratio R_a of the observed abundances at the surface of the sun compared to the abundances observed in the rest of the solar system are the following (Ross & Aller, 1976):

- $R_\mathrm{a}(\mathrm{Li}) = 0.0045$,
- $R_\mathrm{a}(\mathrm{Be}) = 0.4$.

The relatively weak depletion of beryllium (which is burnt at temperatures greater than 3×10^6 K, corresponding to radii below $0.61 r_\odot$), compared to the nearly complete depletion of lithium (which is burnt at temperatures greater than 2.5×10^6 K, corresponding to radii below $0.68 r_\odot$) suggest that the mixing in the tachocline must be very

efficient down to $0.68 r_\odot$, but strongly quenched below $0.61 r_\odot$. This result may also be used to set constraints on models of the tachocline (see Brun, Turck-Chièze & Zahn (1999) for example).

1.5 Dynamics of the solar tachocline

The interior rotation profile of the sun, as well as the related observations presented in Section 1.3 still remains partly unexplained.

1.5.1 Rotation in the convection zone

It is reasonable clear that the rotation profile of the convection zone results directly from the interaction between the rotation and the convective eddies, through anisotropic turbulent angular momentum transport. Near the top of the convection zone, the typical turnover timescale for the convective eddies is of order of a few minutes. This convective motion is hardly affected by the rotation. On the other hand, near the base of the convection zone the typical turnover timescale is comparable to the period of rotation of the sun, which implies that the convective eddies are strongly influenced by rotation. In particular, eddies acquire a non-vanishing helicity which in turns implies that the Reynolds stresses due to convective motions become strongly anisotropic. This anisotropy is believed to be at the origin of the differential rotation in the convection zone. Different approaches have been suggested to study this theory.

Kitchatinov & Rüdiger (1993) (and following papers by the same authors) developed a semi-analytical phenomenological theory in which they prescribe the Reynolds stresses as

$$\begin{aligned} \overline{u_i u_j} &= \begin{pmatrix} \overline{u_r^2} & 0 & 0 \\ 0 & \overline{u_\theta^2} & 0 \\ 0 & 0 & \overline{u_\phi^2} \end{pmatrix} - \sin\theta \begin{pmatrix} 0 & 0 & \nu_{\rm v} r \frac{\partial \Omega}{\partial r} \\ 0 & 0 & \nu_{\rm h} \frac{\partial \Omega}{\partial \theta} \\ \nu_{\rm v} r \frac{\partial \Omega}{\partial r} & \nu_{\rm h} \frac{\partial \Omega}{\partial \theta} & 0 \end{pmatrix} \\ &+ \Omega \sin\theta \begin{pmatrix} 0 & 0 & \Lambda_{\rm v} \\ 0 & 0 & 0 \\ \Lambda_{\rm v} & 0 & 0 \end{pmatrix} , \end{aligned} \tag{1.40}$$

in which the three terms are respectively,

1. a standard isotropic term
2. an anisotropic term which results from the differential rotation, which is based on the expression for the simple isotropic case but with different vertical and horizontal transport coefficients $\nu_{\rm v}$ and $\nu_{\rm h}$.
3. an anisotropic term which results purely from the distortion of the convective eddies, and is present even when the system has no differential rotation. The coefficient $\Lambda_{\rm v}$ has to be calibrated.

Although fairly successful in reproducing the qualitative features of the rotation profile in the convection zone, this theory still fails to provide a self-consistent model for the interaction between convection and rotation, in particular when the nonlinear interaction of the rotation with a meridional circulation are taken into account.

A more straightforward method consists in a Direct Numerical Simulation of the bulk of the convection zone, solving the full system of compressible, non-axisymmetric equations of motion and energy transport equations. Such a system has been solved by Miesch et al. (2000). The simulations reproduce well the equatorial acceleration within the convection zone, as well as the typical range of azimuthal velocities attained by the system between the equator and the pole, but fails to explain the observed independence of the latitudinal shear with radius. This discrepancy of the simulations with the observations is likely to be due to the low Reynolds number of the simulations, which fails to take into account the coupling between convection and rotation on small scales, and lead to a poor determination of the turbulent Reynolds stresses.

However, these models present good qualitative (if not quantitative) explanations of the rotation profile within the convection zone. In particular, it is reasonable to assume that the rotation profile within the convection zone is hardly affected by the dynamics of stably stratified regions below it; and, as a result, it is also reasonable to assume

that the differential rotation of the convection zone can be taken as a robust boundary condition for the fluid motions within the radiative zone.

1.5.2 Models for the tachocline

The discovery of the tachocline raises many fundamental questions.

Why is the radiative zone rotating nearly uniformly? This striking observational result is clearly the proof that some previously unexpected dynamical phenomena are in play within the radiative zone. In Chapter 2, (and, to some extent, in Chapter 6 it will be shown that the rotation of a self-gravitating and thermally stratified fluid body normally drives a meridional circulation, which in turns advects angular momentum and changes the rotation profile of the fluid *away* from uniform rotation. Moreover, the convection zone is imposing a latitudinal shear to the top of the radiative zone, which would propagate all the way to the centre of the sun were only simple isotropic viscous forces taken into account (see Section 2.2.1).

Why is the radiative zone rotating with the observed value of 93% of the equatorial velocity in the convection zone? The simple remark that the interior rotation rate is very close to the surface rotation rate proves that there must be a strong dynamical connection between the radiative zone and the convection zone, as the convection zone is gradually spun down by the solar wind. Indeed, observations suggest that young stars rotate from 10 to 100 times faster that solar type stars (Skumanich (1972) for instance); the very fast rotation of most young stars is related to the conservation of angular momentum as the protostar contracts. It is now widely accepted that magnetic braking is the mechanism responsible for the gradual decrease in angular velocity of a star as it evolves along the main sequence. The braking of the star is due to the magnetic torque exerted by the stellar wind as it expands out into the interstellar medium, and acts efficiently only when a deep outer convection zone is present in the star. Unless the radiative zone is dynamically connected to the convection zone, it has no mean of

slowing down its fast initial rotation. However, helioseismic observations show that the angular velocity of the radiative zone is close to the average angular velocity observed in the convection zone, which confirms the necessity for a strong dynamical connection. Note that the typical timescale for magnetic braking is about 7×10^{10} years at the present age of the sun. Since it is expected that the dynamical timescale in the tachocline is of order of 10^6 yr it is reasonable as a first approximation to neglect the solar spin-down, and assume that the dynamics of the tachocline and the interior are in a steady state on that timescale.

Why is the tachocline so thin? What mechanisms maintain such a structure? Assuming that the radiative interior is in a steady state, the observed rotation profile is necessarily the result of a subtle balance of forces moderating the transport of angular momentum. It will be shown that both the uniform rotation of the interior and the qualitative and quantitative properties of the tachocline can be explained only by the presence of strongly enhanced *latitudinal* angular-momentum transport just below the convection zone. The various possibilities for angular-momentum transport in that region will be introduced in Chapter 2. These will be systematically discussed in Chapter 2 and Chapter 3.

Is this shear layer dynamically stable? In Chapter 2, only the purely hydrodynamical angular-momentum transporters will be considered. In particular, the most natural angular-momentum transporters are turbulent Reynolds stresses, where the turbulence is assumed to be driven by shear instability in the tachocline. This idea, which was originally proposed by Spiegel & Zahn (1992) will be discussed, as well as the stability of the shear in the tachocline, in order to assess whether the tachocline may indeed support turbulent motions.

What is the influence of magnetic fields in the solar interior? In Chapter 3, another class of models will be described, in which the uniform rotation of the interior is explained by the presence of a large-scale magnetic field through the law of isorotation of Ferraro. The ques-

tion of the origin of magnetic fields in the radiative zone is discussed, and lower limit estimates for primordial field are derived. Another possible origin for magnetic fields in the interior is a dynamo field, generally assumed to be created near the base of the convection zone by the interaction of turbulent motions, shear and small scale magnetic fields. The inward diffusion of this dynamo field, and how it may influence the tachocline and the radiative interior, will be studied. The complexity of MHD models is enormous, principally because of the problems of advection of magnetic fields by flows within the tachocline, and the intrinsic nonlinearity of the Lorentz forces. Previous models have failed in reproducing this complexity, either by using oversimplifying assumptions, or, when taking into account all the relevant physics of the tachocline, by failing to propose a solution to the mathematical model. These models and their limitations will be discussed.

Can a self-consistent model for **all** *the observations described previously be found?* In order to go beyond these previous analyses, an intermediate model will be presented, progressively building on the complexity of the system. This new model studies numerically the full nonlinear interaction between a large-scale magnetic field and fluid motions in the radiative zone of the sun when a shear is imposed from the "surface" by the convection zone. In order to do so, preliminary assumptions are necessary, such as incompressibility and axisymetry of the system. The model, the assumptions upon which it is based, and the numerical procedures adopted for studying it are presented in detail in Chapter 4. The numerical solutions are presented in Chapter 5 and extensively tested against theory and other numerical solutions. In particular, boundary layer analyses are presented which represent the solution well for low viscosity and magnetic diffusivity near the boundaries. The relevance of this new model will be discussed by comparing the numerical predictions with the observations. The effects of stratification and energy transport in the tachocline are believed to play an important role in the dynamics of the tachocline (Gough & McIntyre, 1998). It is therefore necessary to drop the assumption of incompressibility; this step is taken in the final Chapter, which

presents and discusses the modified equations and new boundary conditions, before revealing the latest results on the subject of the interior rotation profile of the sun.

Chapter 2

Hydrodynamical models of the tachocline

Early models of the sun have nearly always assumed the sun to be spherically symmetric (i.e. non-rotating and without magnetic field or any other bulk forces that may drive large-scale motions). This assumption was necessary, because the study of the effects of large-scale flows (rotation, meridional circulation ...) on the hydrostatic structure of the sun proves extremely difficult. However, the "non-rotating hydrostatic structure of the sun" as reviewed by Christensen-Dalsgaard et al. (1996) for instance, is observationally verified to be a good approximation to the true hydrostatic structure, which suggests that the effects of rotation, for instance, can indeed be assumed to be a very small perturbation to the hydrostatic equilibrium reference model (see Section 1.2.2). Moreover, in most cases (except that of the Eddington-Sweet timescale) the typical dynamical timescales are comparable with or smaller than the thermal timescale, and so as far as those fluid motions are concerned the hydrostatic structure of the sun can be considered to be in a steady state. These two assumptions will be at the heart of all the following models of the solar *rotation*.

In order to start building models of the solar rotation, the general equations of motion for an axisymmetric fluid in a frame of reference rotating with angular velocity Ω_c will be introduced, and the relevance of possible approximations to the problems studied will be discussed. From these equations, it will be shown how the maintenance of the tachocline relies on the subtle balance of angular momentum below the convection zone. The purely hydrodynamical models of the tachocline that have been proposed so far will then be presented and discussed.

2.1 General equations of hydrodynamics in a rotating frame

In order to construct models of the solar rotation, it is essential to lay out the fundamental equations of fluid dynamics which will be used, as well as the basic assumptions. In the following work, the effect of rotation are always assumed to be a small perturbation on the hydrostatic structure of the sun, so that the fluid motions are slow, and the oblateness of the sun is neglected. The hydrostatic background quantities are assumed to be in a steady state for these fluid motions. The Boussinesq approximation is used to study the effects of compressibility of the fluid, which is based on the assumption that the typical sound travel-time within the region is much shorter than the typical turnover time of the motions, and that the layer is shallow compared to the density scale-height. Within these approximations, the sound waves are "filtered out" (the time derivative of the density fluctuation in the mass continuity equation is neglected), and the total pressure perturbation is assumed to be much smaller than the density or temperature perturbations (if a large pressure perturbation is present, it is very quickly evened out by the sound waves - only provided that the buoyancy cannot balance the pressure perturbation, which is why the layer must be shallow). Within these approximations, the equations are written as

1. the mass continuity equation

$$\nabla\cdot(\rho_{\rm h}\boldsymbol{u}) = 0 \ , \tag{2.1}$$

   where $\rho_{\rm h}$ is the hydrostatic equilibrium density, and $\boldsymbol{u}$ is the velocity.

2. the momentum equation

$$\begin{aligned} & \rho_{\rm h}\left(\frac{\partial \boldsymbol{u}}{\partial t} + \boldsymbol{u}\cdot\nabla\boldsymbol{u} + \dot{\boldsymbol{\Omega}}_{\rm c}\times\boldsymbol{r} + 2\boldsymbol{\Omega}_{\rm c}\times\boldsymbol{u} + \boldsymbol{\Omega}_{\rm c}\times(\boldsymbol{\Omega}_{\rm c}\times\boldsymbol{r})\right) \\ = \ & -\nabla p' - \rho'\nabla\Phi_{\rm h} + \rho_{\rm h}\nu\nabla^2\boldsymbol{u} \ , \end{aligned} \tag{2.2}$$

   where t is the time, p' is the pressure perturbation, ρ' is the

density perturbation, $\Phi_{\rm h}$ is the hydrostatic equilibrium gravitational potential, ν is the molecular or radiative viscosity.

3. the energy equation

$$\rho_{\rm h} T_{\rm h} \frac{\partial s'}{\partial t} + \rho_{\rm h} T_{\rm h} \boldsymbol{u} \cdot \nabla s = \nabla \cdot (K_{\rm t} \nabla T') \ , \tag{2.3}$$

s' is the specific entropy perturbation, s is the total specific entropy $s = s_{\rm h} + s'$, T' is the temperature perturbation, and $K_{\rm t}$ is the thermal conductivity. The full entropy is kept in the advection term because in the region of the base of the convection zone the hydrostatic equilibrium entropy gradient is close to 0, but the perturbation may have a non-negligible entropy gradient.

4. the equation of state: a simple perfect-gas law is sufficient for this discussion, so that

$$p = \frac{\mathcal{R} \rho T}{\mu_{\rm m}} \ , \tag{2.4}$$

where $\mu_{\rm m}$ is the mean molecular weight, and $\mathcal{R}$ is the gas constant. This becomes, in the Boussinesq approximation,

$$\frac{p'}{p_{\rm h}} = \frac{\rho'}{\rho_{\rm h}} + \frac{T'}{T_{\rm h}} \approx 0 \tag{2.5}$$

These equations are now studied in more detail, trying to emphasize the most important phenomena concerning the effects of rotation on the structure of the sun.

2.1.1 Angular momentum transport

One of the most important equations in the case of rotating fluids is the angular momentum conservation equation. In a spherical coordinate system (r, θ, ϕ), where $\boldsymbol{u} = (u_r, u_\theta, u_\phi)$, one can write $\boldsymbol{u} = \overline{\boldsymbol{u}} + \boldsymbol{u}'$, where $\overline{\boldsymbol{u}}$ is the azimuthal average of $\boldsymbol{u}$ and $\boldsymbol{u}'$ a non-axisymmetric per-

turbation. The angular momentum density is defined here as

$$L = \rho r^2 \sin^2\theta\Omega \ , \tag{2.6}$$

where Ω is the angular velocity defined so that $\overline{u_\phi} = r \sin\theta\Omega$. In the following work, the bars above the azimuthally averaged parts are dropped in order to simplify the notation. The primes always denote the perturbations. Combining the mass continuity equation with the azimuthal component of the momentum equation yields

$$\begin{aligned} \frac{\partial L}{\partial t} &+ \nabla\cdot\big(L\boldsymbol{u} + \rho r \sin\theta < u'_\phi \boldsymbol{u}' > - \rho r^2 \sin^2\theta\nu\nabla\Omega \\ &- r \sin\theta B_\phi \boldsymbol{B} - r \sin\theta < B'_\phi \boldsymbol{B}' >\big) = 0 \ . \end{aligned} \tag{2.7}$$

The term in brackets represents the flux of angular momentum, carried respectively by the following transporters of angular momentum: macroscopic advection, microscopic advection (Reynolds stresses), viscous stresses and magnetic stresses (Lorentz stresses) (both macroscopic and microscopic).

Microscopic advection represents the advection of angular momentum by small-scale flows, as opposed to macroscopic advection, which represents advection by a large-scale circulation. Microscopic advection corresponds to the transport of angular momentum by Reynolds stresses, and could be due to:

1. turbulence (or random small scale flows): although stably stratified, the tachocline may be subject to several types of instability which might lead to turbulence. These instabilities involve shear instability (both in the radial and latitudinal direction), magnetic instability, or overshoot.

2. waves: strictly periodic waves (acoustic waves, gravity waves or torsional waves) exchange no net flux of angular momentum with their background medium. However, wave damping or excitation may result in a net flux of angular momentum (Plumb & McEwan (1978), for example).

Molecular and radiative viscosity are extremely small in the sun. However, the associated stress may be important if no other stresses are present, or in the case of boundary layers.

Magnetic fields redistribute angular momentum along their field lines. This effect can be very important (provided the amplitude of the field is large enough), and can act on very large scales. Two terms can be identified, as in the case of advection: a macroscopic term, and a microscopic term (which may be due to magnetic instabilities or MHD waves). These will be discussed in detail in the following chapters.

2.1.2 The thermal wind equation

The thermal wind equation is derived from the curl of the momentum equation: in the purely hydrodynamical case,

$$\frac{\partial \boldsymbol{\omega}}{\partial t} + \nabla\times((2\boldsymbol{\Omega}_\mathrm{c} + \boldsymbol{\omega}) \times \boldsymbol{u}) = -\frac{1}{\rho_\mathrm{h}^2}\nabla p \times \nabla\rho + \nu\nabla^2\boldsymbol{\omega} \ , \qquad (2.8)$$

where $\boldsymbol{\omega} = \nabla\times\boldsymbol{u}$. If the system is in a steady state, the azimuthal component of this equation describes how vorticity is created by the baroclinicity of the flow. This "thermal wind" term drives a circulation provided the isopycnal surfaces differ from the isothermal surfaces. This is the case when the fluid is rotating: the centrifugal force due to the rotation of the sun changes the hydrostatic equilibrium by stretching the isopycnal surfaces into oblate spheroids. However, the thermal stratification retains more easily its spherical structure due to the heat diffusion term in the energy equation. This therefore leads to the baroclinicity of the star; thermal gradients along isopycnal surfaces drive a circulation in order to advect the excess heat. This phenomenon is called the Eddington-Sweet circulation (Sweet (1950)) and occurs even when the star is rotating uniformly.

The timescale for such a circulation is

$$\tau_\mathrm{ES} = \frac{\tau_\mathrm{KH}|\nabla - \nabla_\mathrm{ad}|}{\lambda} \ , \qquad (2.9)$$

where $\tau_{\rm KH}$ is the Kelvin Helmholtz timescale, λ is the ratio of the centrifugal to gravitational forces $\lambda = \Omega_\odot^2 r_\odot^3 / GM_\odot$, and $\nabla - \nabla_{\rm ad} = pN^2/\rho g^2$. Deep in the radiative interior, this timescale is extremely long, of order of $\tau_{\rm ES} = 10^{12}$ y. It is therefore usually neglected as a dynamical phenomenon, simply by omitting the $\mathbf{\Omega}_{\rm c} \times \mathbf{\Omega}_{\rm c} \times \mathbf{r}$ term in the momentum equation. However, in regions where the buoyancy frequency vanishes, a much larger velocity is needed in order to carry the same heat flux. This phenomenon was first described by Mestel (1953), and applies in particular to the region near the bottom of the convection zone, where convective overshoot produces a region of near-adiabatic stratification. Since the depth of the overshoot region still remains undetermined, it is unclear whether this effect has a significant influence on the dynamics of the radiative interior or not.

2.2 The first model of the tachocline

The main characteristic of the solar differential rotation that models will have to explain is the very sharp transition from the latitudinal shear observed in the convection zone to the uniform rotation of the radiative interior. Assuming that the tachocline is not merely a temporary feature, it is a good approximation to consider its dynamical and hydrostatic structure to be in a steady state. The observed differential rotation in the tachocline can therefore be regarded as the result of a subtle dynamical equilibrium between various angular momentum transporting processes. Amongst the transporters of angular momentum described in Section 2.1.1, only three may possibly be used in a realistic hydrodynamical model of the tachocline: advection, wave transport and turbulence (viscous transport can straightforwardly be neglected). These three possibilities will be considered and discussed in this chapter, leaving the case of the magnetic stresses to the following chapters.

The first model of the tachocline to be developed was proposed by Spiegel & Zahn (1992). It is based on the dynamical interaction between strongly anisotropic turbulence and large-scale advection. The main ideas and the assumptions of the model are presented in the fol-

lowing sections, as well as the relevance of the results to observations of the solar tachocline.

2.2.1 Anisotropic turbulence

Given a rotating sphere with isotropic viscosity (molecular or turbulent) subject to a strong latitudinal shear at its surface, it is easy to show that the shear would propagate all the way to the centre of the sphere. Indeed, to a first approximation, let's consider the sphere to be composed of incompressible fluid, and assume that $u_r \ll u_\phi$ and $u_\theta \ll u_\phi$. The momentum equation then reduces to

$$\nu(\nabla^2 u)_\phi = 0 \ , \tag{2.10}$$

(the approximation consists in neglecting the meridional circulation, assumed to be much slower than the azimuthal flow), where ν is the isotropic component of the Reynolds stresses. This implies that the latitudinal shear at the surface is indeed quenched, but on a lengthscale which corresponds only to the typical lengthscale of the applied shear, and is in any case independent of the value of the turbulent viscosity within the sphere.

Despite the approximations made in this example, the basic result remains unchanged should these be dropped, and leads to the following conclusion: if only isotropic Reynolds stresses are taken into account, the shear imposed at the top of the radiative zone by the convection zone propagates all the way to the centre of the sun. This result has been studied in more detail by Spiegel & Zahn (1992) and Elliott (1997), who studied the propagation of a latitudinal shear into an initially uniformly rotating, isotropically viscous radiative zone. They showed that the thickness of the tachocline would increase with time in the following way:

$$\Delta \approx (t/t_{\rm ES})^{1/4} r_{\rm c} \ , \tag{2.11}$$

where $t_{\rm ES}$ is a *local* Eddington-Sweet timescale (as opposed to the one given in equation (2.9)) given by

$$t_{\rm ES} = \left(\frac{N}{2\Omega_{\rm c}}\right)^2 \frac{r_{\rm c}^2}{K_{\rm t}} \ , \tag{2.12}$$

With the values for these parameters described in Appendix A, the tachocline would be expected to have a thickness of about 200,000 km at the present age of the sun. Spiegel & Zahn conclude that the only way to explain the much smaller observed value of the thickness of the tachocline is by requiring that the viscous angular momentum transport be anisotropic, with a much larger flux in the latitudinal direction than in the radial direction. This can be achieved by assuming that the viscous transport occurs through microscopic advection by turbulence in the tachocline.

Spiegel & Zahn argue that if the tachocline is assumed to lie mostly in the stably stratified zone (an assumption which seems to be confirmed by observations, see Section 1.4.2), then turbulent motion in the radial direction is strongly constrained by the buoyancy restoring force. As a result, the turbulence is expected to be mostly two-dimensional, on spherical shells.

Spiegel & Zahn parameterize the turbulent angular momentum transport accordingly by taking the normal isotropic formula for the viscous angular momentum transport, but assuming two different values for the viscosity in the vertical ($\nu_{\rm v}$) and in the horizontal ($\nu_{\rm h}$) direction:

$$\boldsymbol{F}_\nu = r^2 \, \sin^2\theta \left(\nu_{\rm v} \frac{\partial \Omega}{\partial r} \hat{\boldsymbol{e}}_r + \nu_{\rm h} \frac{1}{r} \frac{\partial \Omega}{\partial \theta} \hat{\boldsymbol{e}}_\theta\right) \ , \tag{2.13}$$

where $\boldsymbol{F}_\nu$ is the viscous angular momentum flux. They also assume that $\nu_{\rm v} \ll \nu_{\rm h}$ in order to suppress radial angular momentum transport.

2.2.2 The model and its results

2.2.2.1 Approximations

Spiegel & Zahn consider a compressible, axisymmetric, steady-state, system. The frame of reference is rotating with the interior angular velocity Ω_c, and perturbations are denoted by $\tilde{\Omega} = r\ \sin\theta u_\phi$. Spiegel & Zahn neglect the oblateness of the sun (which is equivalent to dropping the centrifugal force term), and linearize the momentum equation by neglecting u_r and u_θ compared to u_ϕ, and in turn neglecting $\tilde{\Omega}$ compared to Ω_c (as a result, only the gradients of the perturbation $\tilde{\Omega}$ appear in the equations). The background stratification of the tachocline is also neglected, and average values of the hydrostatic profiles of temperature, density, thermal conductivity etc. within the tachocline are used (see Appendix A).

2.2.2.2 Boundary conditions

All perturbed quantities should vanish when approaching the core of the sun. The angular velocity perturbation is imposed at the edge of the convection zone as given by

$$\Omega_{cz}(\theta) = \Omega_{eq}(1 - a_2\ \cos^2\theta - a_4\ \cos^4\theta)\ , \tag{2.14}$$

where Spiegel & Zahn choose to take $a_2 = 0.14$ and $a_4 = 0.16$. The temperature perturbation is required to be continuous through the boundary, which in turn implies that the radial derivative of the angular velocity must be continuous through the boundary too (through the thermal wind equation). Since little radial shear is observed in the convection zone, Spiegel & Zahn assume that $\frac{\partial\tilde{\Omega}}{\partial r} = 0$ at the boundary.

2.2.2.3 Results

Using these approximations and boundary conditions as well as the previously described ansatz for turbulent angular-momentum transport, Spiegel & Zahn calculate analytically the structure of the tachocline. Solutions exist for which all perturbations (in temperature and angular velocity) vanish as depth increases. The typical lengthscale

for the decay of the shear is

$$\Delta = \frac{3\pi}{2\mu_4}\left(\frac{\Omega_c}{N}\right)^{1/2}\left(\frac{K_t}{\nu_h}\right)^{1/4} , \tag{2.15}$$

with $\mu_4 = 4.933$. Using the values given in Appendix A for these parameters, and an estimated thickness for the tachocline of $\Delta = 0.019 r_\odot$, one can derive the required amplitude of the turbulent viscous transport coefficient

$$\nu_h = 6 \times 10^5 \text{ cm}^2 \text{ s}^{-1} , \tag{2.16}$$

which is somewhat higher than what could be expected from turbulent motions in the tachocline, but not wholly unreasonable. By requiring that no net torque is exerted at the top of the tachocline, Spiegel & Zahn estimate the value of the interior rotation rate to be 90% of the value observed at the equator.

2.2.3 Discussion ...

2.2.3.1 ... of the results

The main result obtained by Spiegel & Zahn is the prediction of the angular velocity of the radiative interior, which they evaluate to be 90% of the equatorial value. Observations, on the other hand, suggest that the interior rotates at roughly 93.5 % of the equatorial value (Schou et al. (1998)). This discrepancy is more significant than it may first appear. Indeed, assuming that there exists no net torque between the radiative zone and the convection zone, the interior rotation rate is necessarily a weighted average of the rotation rate of the base of the convection zone. Reasonable models of the dynamical connection between the radiative zone and the convection zone differ only by the angular momentum transporters proposed; hence they all have a different weighing function, but must necessarily predict a value for Ω_c that is between the angular velocity of the equator (Ω_{eq}) and that of the poles ($\sim 0.7\Omega_{eq}$), and unless unexpected importance is given to

the poles, it is more likely that models would yield a value like

$$0.85\Omega_{\rm eq} \lesssim \Omega_{\rm c} < \Omega_{\rm eq} \ . \tag{2.17}$$

Hence a good model should be able to predict the interior rotation rate to a much better accuracy than that proposed by Spiegel & Zahn.

2.2.3.2 ... OF THE ASSUMPTIONS

The model presented by Spiegel & Zahn has the main advantage of providing mostly analytical results; this is due mainly to the linearization of the equations, which allows the separation of variables in the solutions. This assumption proves to be partly justified only: the circulation velocities are indeed very small compared with the rotational velocities, but on the other hand, the angular velocity perturbation $\tilde{\Omega}$ is not necessarily small compared with the background angular velocity $\Omega_{\rm c}$. In fact, at the bottom of the convection zone, boundary conditions near the poles require that $\tilde{\Omega} \simeq 0.2\Omega_{\rm c}$.

The second major assumption comes from the parameterization of the turbulent viscosity, which is very simple but purely phenomenological. The results are intrinsically dependent on the parameterization used; in fact Spiegel & Zahn's main result, namely the strong suppression of the latitudinal shear by the turbulent viscosity, could have been expected since the parameterization of the turbulent stresses is one that would naturally smooth out any angular-velocity gradient. It is now well known, however, that such a parameterization cannot accurately reproduce the effects of two-dimensional turbulence (see, for instance, Gough & McIntyre (1998) or studies of two-dimensional instabilities by Garaud (2001), and also Section 2.3).

2.3 STABILITY ANALYSIS OF THE LATITUDINAL SHEAR IN THE TACHOCLINE

The model proposed by Spiegel & Zahn concerning the turbulent angular-momentum transport does not contain a self-consistent explanation of the origin of the turbulence in the tachocline. Indeed, the

suggestion that the latitudinal and radial shear in the tachocline may be unstable and therefore lead to turbulence was not verified. More recently, Charbonneau, Dikpati & Gilman (1999) (hereafter CDG99) performed a two-dimensional linear analysis of latitudinal shear instability in a spherical shell; the two-dimensional nature of the instability is particularly well justified in the convectively stable radiative zone (and in the tachocline) by the inhibition of any radial motion due to the strong buoyancy restoring force. Unfortunately, a linear analysis alone cannot give any information about the development of the instability, and in particular whether the unstable modes saturate or continue growing and interact with each other. For this reason, it seems important to develop the model proposed by Charbonneau, Dikpati & Gilman further, taking into account in particular the nonlinear interaction of the modes with the background angular velocity in the tachocline. The results of the linear analysis are first analysed and discussed, before introducing the weakly nonlinear formalism.

2.3.1 Summary of the linear analysis results

The question of linear stability of the latitudinal shear observed in the sun has already been addressed, first by Watson (1981) and later by Dziembowski & Kosovichev (1987) and CDG99. Only an outline of the linear analysis and its results is presented here. The vertical motion of the fluid is neglected, and the instability is assumed to take place on a spherical shell. This assumption applies well to the solar radiative zone, where the buoyancy restoring force inhibits all but the slowest radial motions. The perturbations are assumed to be solenoidal, and the fluid is inviscid. The calculation is performed in the spherical coordinate system (r, θ, ϕ), on a shell of unit radius. The velocity field $\mathbf{u}$ is decomposed into its azimuthally averaged part and the perturbation: $\mathbf{u} = \overline{\mathbf{u}} + \mathbf{u}'$. The eigenvalue equation for the perturbation is

$$\left(\frac{\overline{u_\phi}}{\sqrt{1-\mu^2}} - c_m \right) \mathcal{L}_m \psi_m = \psi_m \frac{\mathrm{d}^2}{\mathrm{d}\mu^2} \left(\sqrt{1-\mu^2}\overline{u_\phi} \right) \ , \qquad (2.18)$$

where $\mu = \cos\theta$, ψ_m is the amplitude of the stream function for the azimuthal mode of order m, defined as

$$\boldsymbol{u}' = \nabla\times(\psi\hat{\boldsymbol{e}}_r) \text{ with } \psi = \sum_m \psi_m(\mu)e^{im(\phi - c_m t)} , \tag{2.19}$$

where $\hat{\boldsymbol{e}}_r$ is the unit vector in the radial direction, c_m is the complex growth rate of the mode, and $\mathcal{L}_m$ is the linear operator defined by

$$\mathcal{L}_m\psi_m = \frac{\mathrm{d}}{\mathrm{d}\mu}\left((1-\mu^2)\frac{\mathrm{d}\psi_m}{\mathrm{d}\mu}\right) - \frac{m^2}{1-\mu^2}\psi_m . \tag{2.20}$$

The functions ψ_m must satisfy appropriate boundary conditions. Because of the invariance of equation (2.18) under the transformation $\mu \to -\mu$, the solutions can be represented as a linear combination of symmetric and antisymmetric modes. Symmetric modes, with propagation speed $c_{m,\mathrm{s}}$ are such that $\mathrm{d}\psi_m/\mathrm{d}\mu = 0$ on the equator ($\mu = 0$) and antisymmetric modes, with propagation speed $c_{m,\mathrm{a}}$, have $\psi_m = 0$ on the equator. Regularity at the poles requires that $\psi_m = 0$ at $\mu = \pm 1$. The periodicity of the system requires that the values of m be integers. Because of the functional form of $\mathcal{L}_m$, however, the eigensolutions of equation (2.18) for m and $-m$ are complex conjugates, as are their corresponding growth rates. By convention, the growing modes are chosen to have $m > 0$, whereas the decaying modes have $m < 0$.

General results on this instability were derived by Watson (1981). In particular, Watson derived a necessary condition for instability: that the latitudinal shear can be unstable only if there exists a maximum in the potential vorticity of the system, which is analogous to the well known Rayleigh inflexion-point theorem (Rayleigh, 1880).

Some of the growing solutions are presented by CDG99 for $m = 1$ and $m = 2$, for symmetric and antisymmetric modes. Their results call for the following remarks:

1. By using a three-parameter polynomial fit to the helioseismic inversions of the solar rotation profile in the region of the tachocline,

and calculating its stability, CDG99 concluded that the latitudinal shear in the tachocline is likely to be *stable* to any perturbation. However, the system is observed to be very close to the marginal stability limit (where $\mathrm{Im}(c_m) \to 0$), so that slight differences in the inversions lead to rather different conclusions concerning the stability of the system. In particular, CDG99 deduce from their calculations that only slightly higher within the convection zone (around $0.72 r_\odot$, instead of the assumed position for the tachocline of $0.713 r_\odot$), the rotation profile is unstable to linear horizontal perturbations. It is an often ignored fact that all inversion methods yield *averages* of the angular velocity that extend over a finite region, rather than the true value at a given point. As a result, because the tachocline is not radially resolved by the inversion method, it is likely to undergo a larger shear than observed in the inversions, and hence could be unstable. It is therefore more realistic to use the rotation profile observed only slightly higher in the convection zone as a model for the latitudinal shear in the tachocline.

The commonly used three-parameter fit to the mean zonal (azimuthal) velocity $\overline{u_\phi}$ is:

$$\overline{u_\phi} = \Omega_{\mathrm{eq}} \sqrt{1-\mu^2} (1 - a_2 \mu^2 - a_4 \mu^4) \ , \tag{2.21}$$

where Ω_{eq} is the equatorial angular velocity. For the region near the bottom of the convection zone (at $r = 0.75 r_\odot$), comparison with the observations yields (see CDG99)

$$a_2 \approx a_4 \approx 0.15 \text{ and } \Omega_{\mathrm{eq}} \approx 2.84 \times 10^{-6} \mathrm{s}^{-1} \ , \tag{2.22}$$

(whereas CDG99 used values of a_2 and a_4 closer to 0.1 and 0.05 respectively). In what follows, time is measured in units of $[t] = 1/\Omega_{\mathrm{eq}} \approx 4$ days, so that Ω_{eq} in equation (2.21) is replaced by unity.

2. Linear stability analysis of the particular rotation profile given by the parameter values in (2.22) indicates that three modes are

unstable, namely the $m = 1$ and $m = 3$ symmetric modes, and the $m = 2$ antisymmetric mode. Their respective growth rates are

$$\begin{aligned} \mathrm{Im}(c_{1,\mathrm{s}}) &= 1.68 \times 10^{-2} \\ 2\mathrm{Im}(c_{2,\mathrm{a}}) &= 1.35 \times 10^{-2} \\ 3\mathrm{Im}(c_{3,\mathrm{s}}) &= 1.77 \times 10^{-3} \ , \end{aligned} \tag{2.23}$$

which correspond to growth times of about 240 days, 300 days and 6 years respectively.

3. Although growing and decaying solutions are formally the only ones that lead to a net flux of angular momentum, other solutions can also be found which have a null growth rate, and oscillate with a period of a few years. Moreover, there exist singular solutions, which are also neutrally stable; the oscillation period of these modes varies continuously between the value of the rotation period of the pole, and that of the equator. As a result, there is a critical layer in the flow where the rotation period of the background flow equals $\mathrm{Re}(c)$ and equation (2.18) has a regular singularity. These singular solutions cannot usually be found by standard numerical methods; in any case, the linear approximation formally breaks down within the critical layer. The non-linear behaviour of waves in a critical layer has been extensively studied in the case of linear shear flows (see for instance the work of Killworth & McIntyre (1985), Haynes (1989) or Andrews, Holton & Leovy (1987) for an introductory analysis); it is usually found that waves evolve strong non-linear spiral structures and finally break within the critical layer, locally mixing the potential vorticity.

4. CDG99 pointed out that the behaviour of the rotation profile near the poles could have a strong influence on the stability of the system. It was shown by Schou et al (1998) that the actual solar rotation profile deviates significantly from the power law expansion given by equation (2.21) near the poles in the surface layers (around $r = 0.995 r_\odot$). One might ask whether

this property affects the stability of the system if it persists throughout the convection zone and into the tachocline (a fact which, unfortunately, cannot be verified yet). It is therefore interesting to study the effect of a slowly rotating pole, under the working assumption that it is present also in the region of the tachocline.

2.3.2 Formalism and numerical algorithm for the weakly nonlinear analysis

The weakly non-linear formalism consists mainly of neglecting the direct coupling between the modes, yet keeping the non-linear coupling of each mode with the background shear. This method is commonly used in atmospheric dynamics, to study the interaction of waves with the general atmospheric circulation (see Matsuno (1971) for instance). It is justified when the amplitudes of the modes remain small throughout their non-linear evolution, which can be verified only *a posteriori*. However, because the tachocline is observed to be very close to marginal stability, the linear growth rates of the modes are very small, so that, at least initially, the amplitudes of the modes can be assumed to remain small. The evolution of the background azimuthal velocity experiencing the shear instability is then given by (CDG99)

$$\frac{\partial \overline{u}_\phi}{\partial t} = \frac{1}{\sqrt{1-\mu^2}} \frac{\partial}{\partial \mu} \left[(1-\mu^2) \sum_{m>0}^{\infty} im \left(\psi_m \frac{\partial \psi_m^\star}{\partial \mu} - \psi_m^\star \frac{\partial \psi_m}{\partial \mu} \right) e^{2m\mathrm{Im}(c_m)t} \right] , \quad (2.24)$$

where $\psi_m^\star$ is the complex conjugate of ψ_m. Only modes that are unstable (i.e. for which $\mathrm{Im}(c_m) > 0$) contribute to the sum in equation (2.24), since for $\mathrm{Im}(c_m) = 0$, $\psi_m = \psi_m^\star$.

Assuming that equation (2.24) appropriately describes the non-linear evolution of the system in the case of small-amplitude perturbations (this assumption is discussed in more detail in Section 2.3.6), the weakly non-linear evolution of the modes and the background state

can be obtained by iterating the following steps:

1. calculation of the unstable eigenfunctions and eigenvalues for a given rotation profile, using equation (2.18),

2. evolution of the rotation profile in time according to equation (2.24) using an Euler centred time-stepping scheme,

3. updating the amplitude of the perturbation using

$$\psi_m(\mu = 0, t + \delta t) = \psi_m(\mu = 0, t)e^{-imc_m\delta t} \tag{2.25}$$

for the symmetric modes, and

$$\frac{\partial \psi_m}{\partial \mu}(\mu = 0, t + \delta t) = \frac{\partial \psi_m}{\partial \mu}(\mu = 0, t)e^{-imc_m\delta t} \tag{2.26}$$

for the antisymmetric modes.

2.3.3 Results

The results of the weakly non-linear evolution of the rotation profile of the tachocline are presented in this section. In order to separate the contributions of the different modes of oscillation, Sections 2.3.3.1 and 2.3.3.2 present separately the evolution of two modes of oscillation, and their interaction with the background rotation profile. Section 2.3.4 then presents the results when the combined action of all modes is taken into account. Section 2.3.5. presents the results of the weakly non-linear evolution of a system that mimics the slow rotation of the poles, as observed near the surface of the sun. These results, as well as the validity of the weakly non-linear algorithm, are then discussed in Section 2.3.6

The rotation profile described by equation (2.22) has three linearly unstable modes, the $m = 1$ and $m = 3$ symmetric modes and the $m = 2$ antisymmetric mode. The weakly non-linear evolution of two of these modes is presented here for each mode separately, in order to illustrate more clearly some of the specific features of the non-linear interaction of the perturbation and the background flow.

2.3.3.1 The $m = 1$ symmetric mode

The results of the non-linear evolution of the $m = 1$ symmetric mode and its influence on the background rotation profile are presented in Fig. 2.1. The initial conditions for this calculation are:

- $u'_\theta = \epsilon \overline{u}_\phi$ at the equator, with $\epsilon = 10^{-4}$,
- the initial rotation profile is described by equation (2.22).

It is found that for such an initial amplitude, an acceptable time-step for the simulation is $\delta t = 5 \times 10^{-3}$. These results call for the following comments:

1. Fig. 2.1a represents the evolution of the real and imaginary parts $c_{1,\mathrm{s}}$. Note the decay of the growth rate $\mathrm{Im}(c_{1,s})$ of the mode with time, which shows the non-linear saturation process. The calculation had to be stopped when $\mathrm{Im}(c_{1,\mathrm{s}}) < 2 \times 10^{-3}$ because the mode became too nearly singular to compute. The real part of $c_{1,\mathrm{s}}$ on the other hand remains approximately constant throughout the evolution of the system. The background state approaches marginal stability (i.e. a system with vanishing growth rate and Reynolds stresses). Defining the time-scale for saturation to be the typical time required for the growth rate to drop by a factor of 2, it is observed that for an initial amplitude of $\epsilon = 10^{-4}$, $\tau = 135$ (which corresponds to about 540 days). The variation of the saturation time-scale with initial amplitude is shown in Fig. 2.2

2. The Reynolds stresses, transporters of angular momentum, are represented in Fig. 2.1b. Note how these are concentrated near 60°, which corresponds to the latitude of the maximum of potential vorticity of the background flow (see Fig. 2.1d). The Reynolds stresses are proportional to the square of the amplitude of the eigenfunction, and, after a period of increase, begin decreasing with time despite the increase in the amplitudes of both the real and imaginary parts of the eigenfunction, as given by equations (2.25) and (2.26). This effect is due to $\mathrm{Im}(c_m) \to 0$: when $\mathrm{Im}(c) = 0$, the real and imaginary part of the eigenfunctions are solutions to the same equation with the same boundary

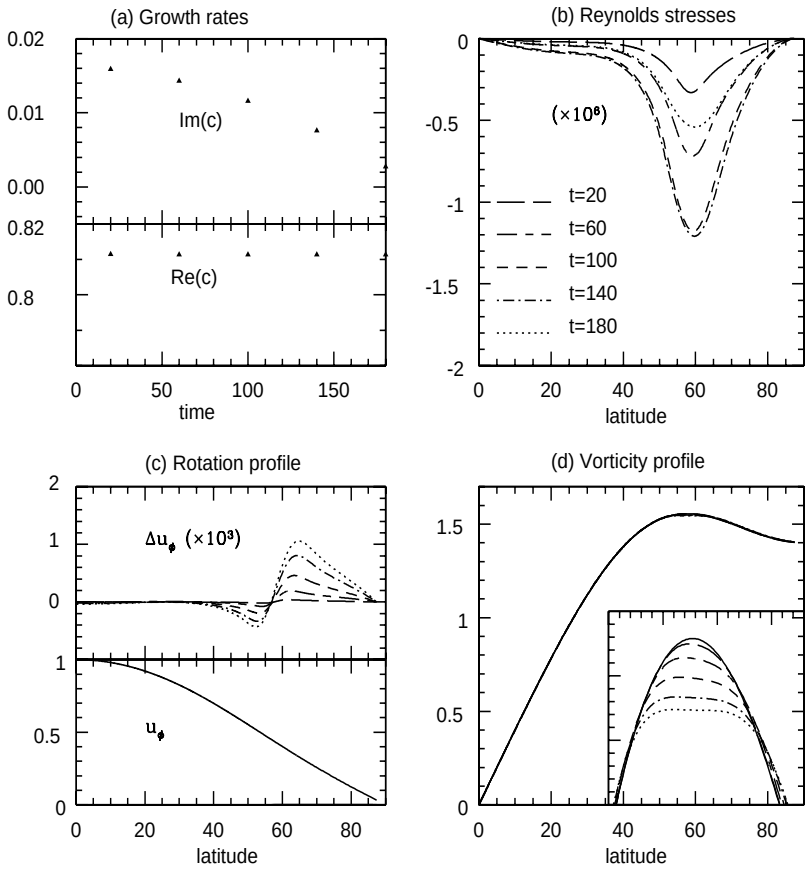

Figure 2.1: Evolution of the $m = 1$ symmetric mode of the perturbation and the background rotation profile with time, for the initial conditions described in Section 2.3.3.1. (a) Real and imaginary parts of the complex growth rate. (b) Reynolds stresses ($\times 10^6$) for 5 successive dimensionless times with line style coding as shown. (c) Rotation profile: the lower box contains the actual rotation profile, for 5 different times, but the deviation from the original rotation profile is too small to be seen. In the top box, the actual deviation ($\times 10^3$) is plotted for 5 different times (same line-style coding as before). (d) Vorticity profile: the main box contains the vorticity profile for 5 different times (same line-style coding as before), and the inset is an enlargement of the region of the maximum of the vorticity curve. The solid line represents the initial vorticity profile.

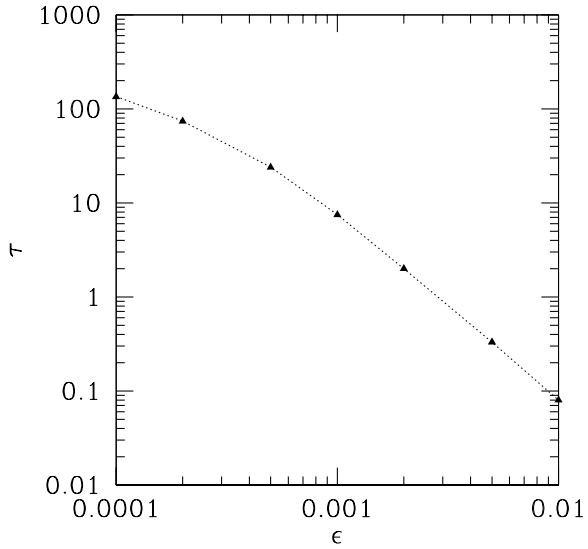

Figure 2.2: Saturation time-scale τ as a function of initial amplitude ϵ of the $m = 1$ symmetric mode.

conditions, so that $\psi_m \to \psi_m^\star$. As a result, the Reynolds stresses in equation (2.24) also tend to zero.

3. The evolution of the initial rotation profile due to the perturbation is shown in Fig. 2.1c. The bottom curve is the actual rotation profile at each time, but the deformation due to the instability is too small to be seen. The deviation from the initial rotation profile is shown in the top half of the panel, and takes the form of a localized increase in the azimuthal velocity of the flow around a latitude of about 60°; however, being very small, this increase only results in a slight localized flattening of the zonal velocity profile. The flattening process slows down with time.

4. The saturation mechanism can best be understood from Fig. 2.1d. The evolution of the radial component of vorticity (which is proportional to the potential vorticity of the flow) is shown here; the inset shows an enlargement of the region near the potential-vorticity maximum. Since the existence of the maximum has an important role to play in the excitation mechanism of the instability (Rayleigh (1880), Watson (1981)) it is not surprising that the slow erosion of the vorticity maximum due to the instability, as observed in Fig. 2.1, acts to stabilize the system and leads it towards a state of marginal stability. Note that, as expected from any two-dimensional flow, the total potential vorticity is conserved; the perturbation merely redistributes it from the position of the maximum towards the pole and the equator.

2.3.3.2 The $m = 2$ antisymmetric mode

The results of the non-linear evolution of the $m = 2$ antisymmetric mode and its influence on the background rotation profile are presented in Fig. 2.3. The initial conditions for this calculation are:

- $u'_\phi = \epsilon \overline{u}_\phi$ at the equator, with $\epsilon = 10^{-4}$,
- the initial rotation profile is described by equation (2.22).

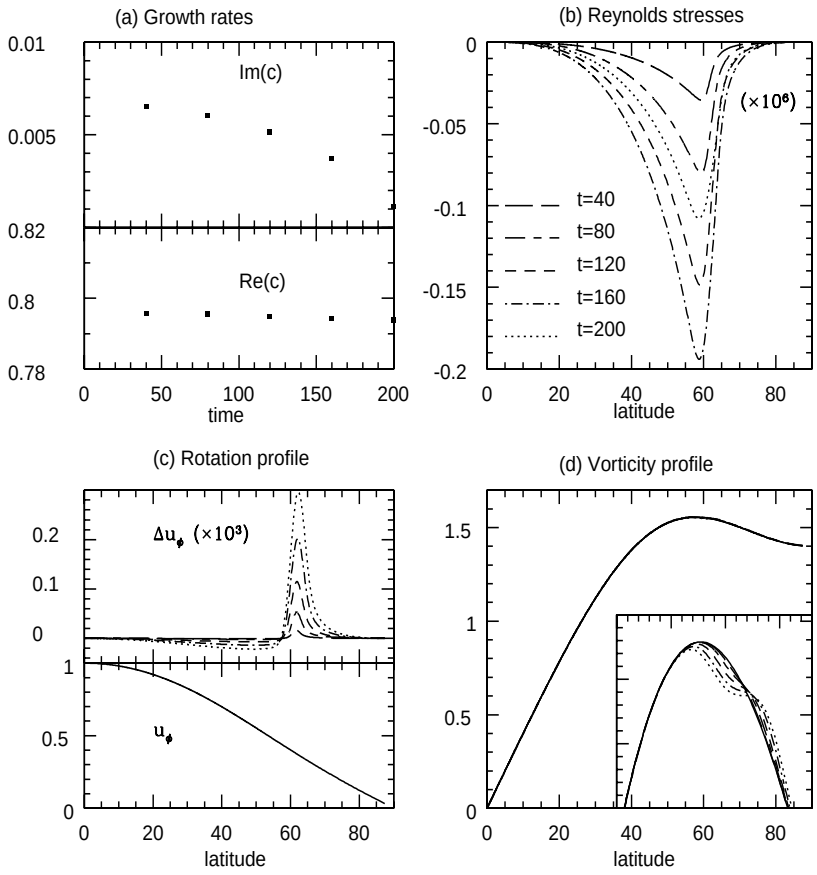

Figure 2.3: Evolution of the $m = 2$ antisymmetric mode of the perturbation and the background rotation profile with time, for the initial conditions described in Section 2.3.3.2. The panels are similar to those presented in Fig. 2.1, applied to the $m = 2$ mode. The various quantities have been plotted at 5 different dimensionless times, with line style coding as shown in panel (b). Note the change in the vertical scale in panels (b) and (c).

The results for the $m = 2$ mode are similar to those presented for the $m = 1$ mode. Note however the two main differences: firstly, the growth rate for the $m = 2$ mode is smaller than that of the $m = 1$ mode (Fig. 2.3a), which leads to smaller values of the Reynolds stresses at a given time t (Fig. 2.3b). As a result, the influence of this mode on the background rotation profile is much smaller than for the previously shown $m = 1$ mode (Fig. 2.3c). Secondly, the action on the vorticity occurs at a different latitude, creating a step-like feature in the vorticity profile (Fig. 2.3d). However, because this also affects the vorticity maximum, saturation still occurs (as seen in Fig. 2.3a and 2.3b) but on a longer time-scale. In this case, the instability is observed to evolve on a time-scale of about $\tau = 580$ (which corresponds to about 6.3 years) for the initial amplitude used in this calculation. The marginally stable state eventually reached by the system is different from the one obtained in the case where the $m = 1$ mode was evolved.

2.3.4 All modes

The results of the non-linear evolution of the perturbation and its influence on the background rotation profile are presented in Fig. 2.4. The initial conditions for this calculation are:

- the initial rotation profile is described by equation (2.22),
- $u'_\theta = \epsilon \overline{u}_\phi$ at the equator for the symmetric modes,
- $u'_\phi = \epsilon \overline{u}_\phi$ at the equator for the antisymmetric modes,

where $\epsilon = 10^{-4}$.

In this final plot, all the modes have been taken into account. Starting with similar amplitudes for linearly unstable $m = 1$, $m = 2$ and $m = 3$ modes, the stability of other modes to the evolved rotation profile is checked regularly: none of these modes becomes unstable. Note that because the growth rates of the $m = 2$ and $m = 3$ modes are much smaller than that of the $m = 1$ mode, the effect of the instability on the background rotation profile is dominated by the $m = 1$ mode.

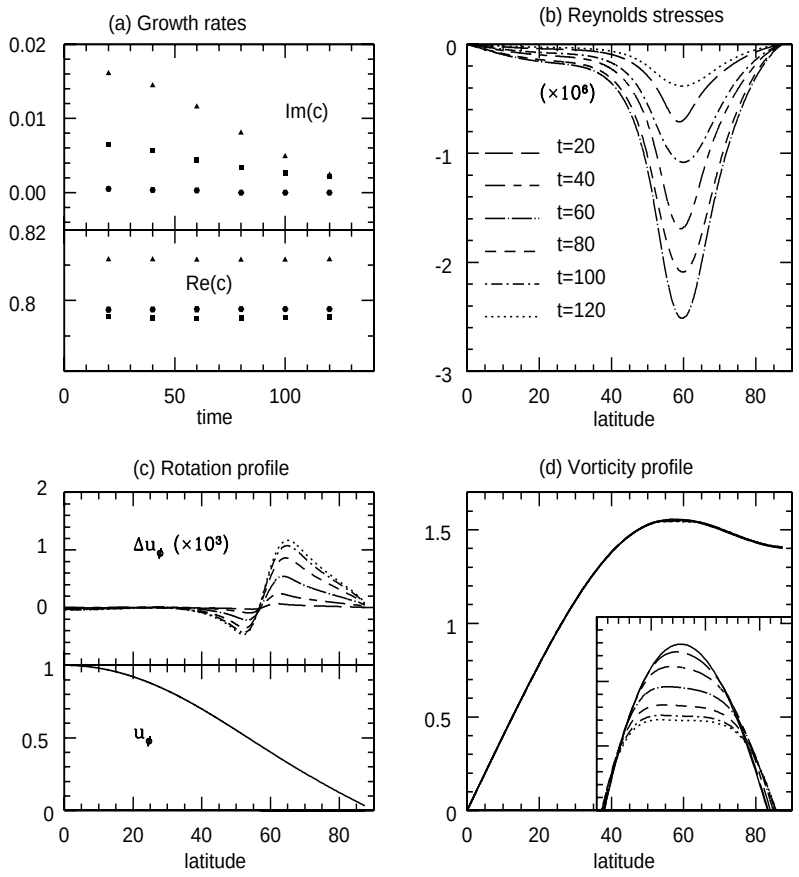

Figure 2.4: Evolution of the perturbation and the background rotation profile with time, for the initial conditions described in Section 2.3.4. The diagrams are the similar to those presented in Fig. 2.1, with the line style coding as shown in panel (b). Note that in panel (a), triangles represent the $m = 1$ mode, squares the $m = 2$ mode and circles the $m = 3$ mode.

The instability tends to a state of marginal stability on a time-scale of about $\tau = 80$; again, this marginally stable state is different from the one obtained in Sections 2.3.3.1 and 2.3.3.2 where only one mode (either $m = 1$ or $m = 2$) was taken into account.

2.3.5 Effect of a slowly rotating pole

It has been observed by Schou *et al.* (1998) that the rotation rate near the poles deviates significantly (by more than 10%) from the usual power law expansion described in equation (2.21), in the surface layers of the sun. Unfortunately, owing to degradation of the resolution with both depth and with latitude it is not possible yet to check whether this slow rotation persists deeper in the convection zone. Theories and numerical simulations have so far failed to explain this phenomenon through purely hydrodynamical effects. It is therefore possible that this rotation profile may have a much deeper origin, and persist throughout the convection zone and the tachocline. Assuming this to be the case, the aim of this section is to study the effect of a slowly rotating pole on the stability of the tachocline to latitudinal shear instability.

The initial rotation profile studied now is based on the observations of the solar rotation profile near the surface (at $r = 0.9875 r_\odot$), and is adapted from the results of Schou et al. (1998). A good three-parameter fit is given by

$$\Omega_{3-\mathrm{fit}}(\theta) = 1.014(1 - 0.115\ \cos^2\theta - 0.178\ \cos^4\theta)\ , \qquad (2.27)$$

in units of Ω_{eq} as given by equation (2.22). The residual between this expression and the observed angular velocity as given by Schou et al. (1998) is shown in Fig. 2.5, in the same units. The total amplitude of the residual at the poles is not known. In order to test quantitatively the influence of a slowly rotating pole, several fits to the residual have

been tested; they are given by

$$\begin{aligned}
\text{Model 0: } \Omega_{\rm res} &= 0 \ , \\
\text{Model A: } \Omega_{\rm res} &= 3.3 \times 10^{-2} (\tanh^5(1.8\pi\theta) - 1) \ , \\
\text{Model B: } \Omega_{\rm res} &= 4.4 \times 10^{-2} (\tanh^{3.5}(1.7\pi\theta) - 1) \ , \\
\text{Model C: } \Omega_{\rm res} &= 5.5 \times 10^{-2} (\tanh^4(2\pi\theta) - 1) \ .
\end{aligned} \tag{2.28}$$

The initial rotation profiles given by $\Omega_0 = \Omega_{3-\rm fit} + \Omega_{\rm res}$ for the four models are evolved using the weakly non-linear algorithm. As in the previous section, the initial conditions for the perturbation are:

- $u'_\theta = \epsilon \overline{u}_\phi$ at the equator for the symmetric modes,
- $u'_\phi = \epsilon \overline{u}_\phi$ at the equator for the antisymmetric modes,

where $\epsilon = 10^{-4}$. The results are shown in Fig. 2.6. This plot shows the deviations from the initial background rotation profiles, given by Models 0, A, B and C at the dimensionless time $t = 120$ (for which the system in all cases is close to saturation). Model 0 has no dip in the polar rotation rate, and the corresponding results are very close to those presented in Section 3.2, despite the change of the coefficients a_2 and a_4 used for the three parameter fit. As CDG99 suggested, the instability depends more on the total shear (i.e. $a_2 + a_4$) than on the respective values of these coefficients. The main effect of a slowly rotating pole is to introduce a second increase in the azimuthal velocity of the background flow, at a latitude of about 80°. The slower the polar rotation, the larger the increase (above the initial value) in angular velocity near the poles.

2.3.6 Discussion

The results described above are now discussed, with relevance to observations, and the problem of angular-momentum transport in the solar tachocline. The validity of the weakly nonlinear algorithm is also discussed.

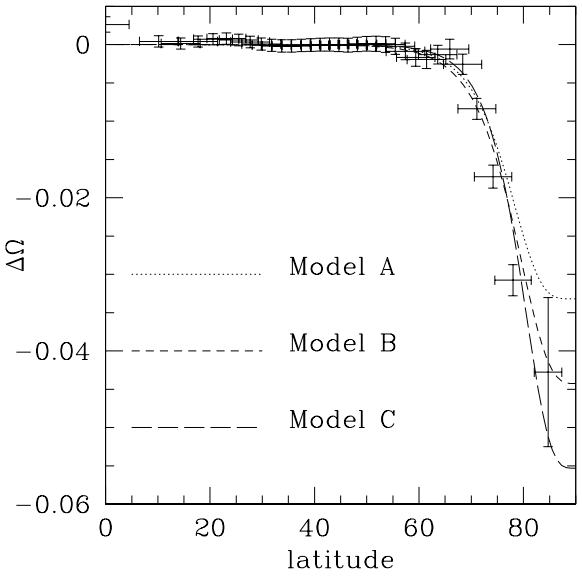

Figure 2.5: Variation with latitude of the residual between the observed rotation profile at a radius of $0.9875 r_\odot$, and the three-parameter fit given by equation (2.27), in dimensionless units. The vertical error-bar represent the error on the rotation rate, and the horizontal one the width of the averaging kernel (which gives insight into the resolution of the data).

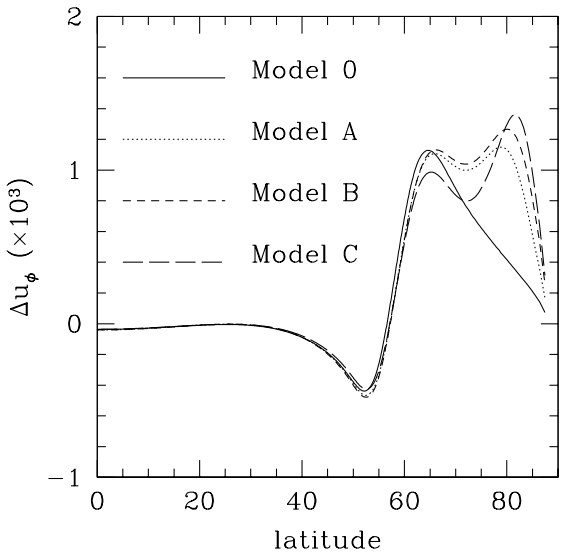

Figure 2.6: Deviation from the background rotation profile as a function of latitude at the dimensionless time $t = 120$, for models 0, A, B, C and D.

Watson, in 1981, showed that a latitudinal shear on a spherical shell can only be unstable to two-dimensional perturbations provided there exists a *sufficiently strong* maximum in the background potential vorticity. If this is the case, the growing or decaying eigenmodes of the perturbations are traveling Rossby waves, oscillating with a frequency $m\mathrm{Re}(c_m)$ which takes values between the background rotation period of the pole and that of the equator. The waves redistribute potential vorticity down-gradient, and gradually erode the potential vorticity maximum. This process slowly stabilizes the system, which can be seen for instance in the decay of the growth rate with time.

The growth rate is intrinsically linked with the Reynolds stresses, and as $\mathrm{Im}(c_m) \to 0$, $\psi_m \to \psi_m^\star$, so that the right-hand side of equation (2.24) tends to 0: the system is asymptotically driven towards a state of marginal stability. The typical time-scale τ for the saturation of the background flow is shown as a function of the initial amplitude of the perturbation in Fig. 2.2. It is common in astrophysics to assume that the marginally stable state reached by a system after the saturation of an instability is unique. This is usually the case when the stability criterion is local, as it is in convective instability, for example. On the other hand, when the instability criterion is global, marginally stable states are usually not unique; the results presented in this paper illustrate this phenomenon. The marginally stable state reached by the system depends on the initial rotation profile as well as the initial spectrum of amplitudes of the modes, but is independent of the total power of the perturbation for a given initial rotation profile. The stable states need *not* be states of monotonically increasing/decreasing potential vorticity; in fact, there exist many rotation profiles containing a maximum in potential vorticity which are *stable* to latitudinal shear instability (see Watson (1981) and CDG99). It could be argued that the system takes an infinitely long time to reach the marginally stable states, but this is only an artefact of the weakly non-linear approximation. As the system approaches a marginally stable state, the perturbation eigenfunctions become more and more singular and the linear approximation locally breaks down near the critical latitudes.

By analogy with linear shear flow analysis (see for instance Haynes 1989), one can assume that the Rossby waves eventually break within the critical layer due to their non-linear evolution, locally mixing potential vorticity and therefore completing the saturation process.

Helioseismic inversions are usually able to obtain only the axisymmetric, north-south symmetric rotation profile. In those cases only the background flow $\overline{u_\phi}$ (which is by definition axisymmetric) can be detected. In all the cases studied, the state of marginal stability reached by the system deviates only very slightly from the original state, with a total deviation of no more than 0.2 % of the original angular velocity given by the three-parameter fit. Such a small variation could not be detected by helioseismic inversions. The effect of a slowly rotating pole has also been studied. It has been shown that the resulting marginally stable state contains an additional enhancement of the angular velocity at a latitude of about 80°. However, the global stability properties of the system are hardly changed: the saturation time-scale remains similar, and the average amplitude of the deviation from the initial rotation profile does not exceed 0.2%. These results suggest that the solar rotation profile might actually be in a state of marginal stability. The adjustment of the background rotation profile to the shear instability occurs on a time-scale no longer than that of other angular-momentum transporting processes (such as a large-scale meridional circulation, and possibly magnetic stresses); as a result, although this instability is not dominant in the *overall* determination of the final steady-state profile, it may force the system, at all times, to remain close to a state of marginal stability.

2.3.6.2 Discussion of the validity of the weakly nonlinear algorithm

The weakly non-linear algorithm presented here, and in particular the equation (2.24) for the evolution of the background flow, is valid only provided the background flow evolves on a time-scale that is much larger than the period of oscillation of the perturbation. Since typically $\mathrm{Re}(c)$ is of order of unity, it is essential that $\tau \gg 1$. Comparing this condition with the results presented in Fig. 2.2 shows that the

weakly non-linear algorithm can be applied, roughly speaking, only to perturbations of amplitude ϵ smaller than 10^{-3}.

The main difficulty in studying the inviscid latitudinal shear flow instability arises from the presence a critical layer in the flow, at a latitude for which the phase speed of the wave is equal to the velocity of the background flow: $\overline{u_\phi} = c_m\sqrt{1-\mu^2}$ when c_m is real. At this point the eigenvalue equation has a regular singularity; the critical layer leads to the existence of a continuum of singular, neutrally stable eigenmodes. The weakly non-linear *algorithm* presented in this paper is proposed as an alternative to a more rigorous weakly non-linear theory (see, for example, Drazin & Reid, 1981, chapter 7): it allows one to make full use of the results of linear theory and provides a relatively easy method of calculating the weakly non-linear interaction of the modes with the background rotation profile, whereas standard weakly non-linear theory can formally not be used because of the interaction between the continuum of neutrally stable singular modes and the discrete unstable ones. The addition of viscosity (albeit vanishingly small) would simplify the *mathematical* problem, since the critical layer is then replaced by a viscous boundary layer, and the continuum of neutral modes is replaced by a discrete spectrum of either growing or decaying modes. In that case, the results of weakly non-linear theory and those provided through the algorithm presented in this paper can be shown to be similar *provided* that the system is sufficiently close to marginal stability, and that the bifurcation to instability is supercritical. The first condition is likely to be fulfilled by the solar rotation profiles studied in Sections 2.3.4 and 2.3.5. The second condition would guarantee that the system remains subcritically stable to finite-amplitude perturbations. Both these conditions can be verified only by studying the full non-linear theory of this shear flow, which is beyond the scope of this paper (one might note that there exist subcritical instabilities in plane and cylindrical Couette flow, which is similar but not completely analogous to the flow considered here).

2.3.7 Conclusion

Spiegel & Zahn (1992), in an attempt at explaining the rotation profile in the region of the solar tachocline, suggested that the observed latitudinal shear in that region may be unstable, and through the resulting anisotropic turbulence, sustain an enhanced latitudinal flux of angular momentum.

In order to check whether latitudinal shear instability may indeed lead to the required angular momentum flux in the tachocline, a weakly non-linear algorithm was constructed, which allows the study of the evolution of a background rotation profile undergoing two-dimensional latitudinal shear instability. The linear stability of the system depends on the global characteristics of the shear and in particular the total difference between the angular velocity of the equator and that of the poles. The existence of a sufficiently pronounced maximum in the potential vorticity is a necessary condition for instability. The linear eigenmodes of the perturbation can be identified as Rossby waves, and transport vorticity down-gradient. As a result, the vorticity maximum is "eroded" by the weakly non-linear evolution of the perturbation, which slowly leads to the saturation of the instability, and drives the system towards a state of marginal stability. There exists a continuum of marginally stable states, and these have two important features: they have null Reynolds stresses, which leads to no net flux of angular momentum, and in the case of the tachocline, they induce a deviation from the observed rotation profiles parameterized by equation (2.21) which is less than 0.2 %; such a small deviation could not be detected helioseismically. It seems likely that the tachocline is essentially in a state of marginal stability with regard to latitudinal shear instability.

This study suggests that the latitudinal shear instability cannot be solely responsible for the observed rotation profile in the region of the tachocline, and the uniform rotation of the interior: another mechanism must also be involved, which could be attributed to Lorentz stresses (Gough & McIntyre, 1998). However, most angular-momentum transporting processes appear to act on time-scales not significantly

shorter than the characteristic time-scale for the saturation of this shear instability and the convergence of the background rotation profile towards a marginally stable state. As a result, although probably insignificant in the determination the overall shape and evolution of the angular rotation profile, the Reynolds stresses due to latitudinal shear instability could still play an important role in keeping the system, at all times, close to a marginally stable state.

2.4 Gravity wave damping model

Another way of obtaining efficient angular momentum transport throughout the radiative zone without chemical mixing below $r = 0.61 r_\odot$ is through the propagation and damping of gravity waves (Schatzman (1993)). This mechanism is especially important in the terrestrial atmosphere, where it is thought to be responsible for the Quasi-biennial Oscillation, in a similar way as the propagation and damping of gravity waves in a rotating tank result in the emergence of bands, rotating alternatively in a prograde and retrograde fashion (Plumb & McEwan, 1978). Zahn, Talon & Matias (1997), Kumar & Quataert (1997) and more recently Kumar, Talon & Zahn (1999) therefore suggested that gravity waves dissipation may be a way of explaining the spin-down of the radiative zone of the sun.

Their idea is the following: gravity waves are excited at the base of the convection zone by large-scale convective eddies. Since these waves are evanescent in the convection zone, they can only propagate inwards, into the radiative zone. The angular momentum balance implied by the propagation of the waves is simply given by:

$$\frac{\partial}{\partial t}\left(\rho r^2 \sin^2\theta \Omega\right) = -\nabla\cdot(\rho r \sin\theta u_\phi \boldsymbol{u}) \,, \tag{2.29}$$

where $\boldsymbol{u}$ is now the Lagrangian displacement velocity of the wave, and u_ϕ its azimuthal component. In the radiative zone, the waves are thermally damped, and gradually release their energy and angular momentum. The damping (and therefore the angular momentum release) essentially depends on the frequency of the waves, with a

faster damping for lower frequencies. Since the waves are excited in a rotating frame, prograde and retrograde waves are excited with the same amount of energy, with the same frequency but opposite propagation direction. If these waves were traveling in a uniformly rotating medium, they would release nearly the same amount of angular momentum but in opposite directions, therefore resulting in little net angular momentum flux. However, if a wave propagates into a medium which rotates with a higher angular velocity for example, the local frequency of the wave is Doppler shifted compared to its original frequency with:

$$\tilde{\omega} = \omega - m\tilde{\Omega} \ , \tag{2.30}$$

where m is the azimuthal order, ω is the initial frequency of the wave, $\tilde{\omega}$ is the frequency in the new frame, and $\tilde{\Omega}$ is the local angular velocity of the background flow relative to that of point where the gravity wave was excited. Since the Doppler shifts of prograde and retrograde waves are different (i.e. m is positive for prograde waves, and negative for retrograde waves), they are damped within a different scaleheight, resulting locally in a non-zero angular momentum flux.

Zahn, Talon & Matias (1997), Kumar & Quataert (1997), and Kumar, Talon & Zahn (1999) proposed that such a mechanism could explain the global spin-down of the radiative interior following the braking of the convection zone due to the solar wind. This might indeed be a possibility in a global sense, since gravity waves do provide a strong dynamical coupling between the two zones. However, since gravity-waves damping tend to enhance any pre-existing shear rather than quench it, it is difficult to explain how such a mechanism could lead to the observed uniform rotation in the radiative zone.

2.5 Conclusion

In this chapter, the various hydrodynamical possibilities of angular momentum transport in the sun have been inspected, which might be responsible for the very fast quenching with depth of the latitudinal differential rotation imposed by the convection zone on the radiative zone. Conservation of angular momentum, in the purely hydrody-

namical case, necessarily results from a balance between large-scale advection and Reynolds stresses; the Reynolds stresses originate either from microscopic advection by turbulence or waves. Only models which may conform to the light-element abundances observations have been given serious consideration (global circulation models were rejected on the grounds that they would lead to the complete depletion of lithium and boron, which is not observed in the sun).

The case of turbulent Reynolds stresses was studied by Spiegel & Zahn (1992); they found that the observed thickness of the tachocline, of about 2 % of the solar radius, immediately rules out the possibility of isotropic Reynolds stresses. Angular momentum transport must be far more efficient in the latitudinal direction than in the radial direction, otherwise the latitudinal shear would propagate all the way to the centre of the sun. Spiegel & Zahn therefore proposed a model in which turbulence is essentially two-dimensional, and lead to highly anisotropic Reynolds stresses; they suggest that latitudinal or radial shear instability may be responsible for the maintenance of turbulence in the tachocline. Their model however fails in two respects:

1. Two-dimensional inviscid motion is known to conserve (and therefore transport) potential vorticity rather than angular momentum. Spiegel & Zahn however ignored this fact in their parameterization of the angular momentum transport in the tachocline; their results are therefore "spurious" in the sense that two-dimensional turbulence would not lead to the quenching of differential rotation, as they claim, but would rather sustain it.

2. Study of the latitudinal shear instability within the tachocline reveals that the shear is close to marginal stability; nonlinear evolution of the instability shows that the differential rotation quickly converges to a state of marginal stability, which sustains no net angular momentum flux (Garaud, (2001), and Section 2.3). Spiegel & Zahn's suggestion that turbulence in the tachocline may be sustained by latitudinal shear instability is therefore unlikely to be true.

The case of angular momentum transport by waves was also inspected, and it was shown that gravity waves leads to the enhancement, rather than the quenching, of any differential rotation beneath the convection zone. Although this mechanism might indeed be responsible for the dynamical connection between the radiative zone and the convection zone as the convection zone is spun-down by the solar wind, it is hard to see how it could explain alone the structure of the solar tachocline or the uniform rotation of the radiative zone.

Looking at the failure of the many hydrodynamical models proposed to explain altogether the interior rotation of the sun, the structure of the tachocline and the observed light-element abundances leads to the same conclusion as Gough (1997) and Gough & McIntyre (1998), namely that there seems to be no purely hydrodynamical model capable of explaining the solar interior rotation.

Chapter 3

MHD models of the tachocline

3.1 Introduction to MHD

Magnetohydrodynamics studies the dynamical interaction between magnetic fields and fluid motions in a conducting plasma. Magnetic fields affect fluid motions through the Lorentz force, whereas fluid motions affect magnetic fields through the advection equation. The MHD equations of motion in the Boussinesq approximation are therefore changed to the following form:

$$\nabla\cdot(\rho_{\rm h}\mathbf{u}) = 0 \ , \tag{3.1}$$

$$\begin{aligned}&\rho_{\rm h}\left(\frac{\partial \boldsymbol{u}}{\partial t} + \boldsymbol{u}\cdot\nabla\boldsymbol{u} + \dot{\boldsymbol{\Omega}}_{\rm c}\times\boldsymbol{r} + 2\boldsymbol{\Omega}_{\rm c}\times\boldsymbol{u} + \boldsymbol{\Omega}_{\rm c}\times(\boldsymbol{\Omega}_{\rm c}\times\boldsymbol{r})\right)\\ = \ &-\nabla p' - \rho'\nabla\Phi_{\rm h} + \boldsymbol{j}\times\boldsymbol{B} + \rho_{\rm h}\nu\nabla^2\boldsymbol{u} \ ,\end{aligned} \tag{3.2}$$

$$\rho_{\rm h}T_{\rm h}\frac{\partial s'}{\partial t} + \rho_{\rm h}T_{\rm h}\boldsymbol{u}\cdot\nabla s = \nabla\cdot(K_{\rm t}\nabla T') \ , \tag{3.3}$$

$$\frac{p}{p_{\rm h}} = \frac{T}{T_{\rm h}} + \frac{\rho}{\rho_{\rm h}} \ , \tag{3.4}$$

$$\frac{\partial \boldsymbol{B}}{\partial t} = \nabla\times(\boldsymbol{u}\times\boldsymbol{B}) - \nabla\times(\eta\nabla\times\boldsymbol{B}) \ , \tag{3.5}$$

$$\nabla\cdot\boldsymbol{B} = 0 \ . \tag{3.6}$$

It has been known for a long time that even a very small magnetic field can have a significant influence on a rotating fluid. Owing to the large electric conductivity in the sun (in particular in the stably stratified regions), the timescale for ohmic decay $\tau_{\rm d}$ is usually much larger than any dynamical timescale. In that case, the fluid can be considered to be a perfect conductor, and the magnetic field lines may be assumed to be frozen in the fluid. This has important consequences, and leads in particular to the law of isorotation of Ferraro (1937), which states

that the angular velocity of axisymmetric, perfect MHD fluids in a steady state must be constant along magnetic field lines, that is

$$(\boldsymbol{B} \cdot \nabla)\boldsymbol{\Omega} = \mathbf{0} \ . \tag{3.7}$$

Mestel (1953) and Cowling (1957) were the first to suggest the relevance of this effect in the case of the sun. Mestel & Weiss (1987) showed that values as small as $10^{-3} - 10^{-2}$G should be capable of suppressing any rotational shear deep in the solar interior, taking into account various magnetic instabilities. Assuming that a large-scale magnetic field of that intensity may indeed exist in the radiative zone, this would provide the most natural explanation for its observed uniform rotation. It is therefore important to assess the question of the possible origins and intensity of magnetic fields within the radiative zone, before setting up an MHD model for the tachocline.

3.2 Origin of magnetic fields in the solar interior

The existence of an interstellar field suggests a lower limit of 10^{-6}G for the field in the radiative zone of the sun. In order to improve on such an estimate, two possibilities may be considered: either the field can be regarded as primordial (more precisely, as a legacy of the pre-main-sequence evolution of the sun), pervading the interior and slowly diffusing into the convection zone, or else it results from the inward diffusion of the field produced by a dynamo located in the vicinity of the interface between the radiative and convective zones.

3.2.1 Primordial field

Assuming that the collapse of a molecular cloud into a protostar conserves magnetic flux, the presence of a very large poloidal field in the core of the protostar can easily be explained. However, through the subsequent fully convective Hayashi phase, most of this relic flux is likely to be destroyed by turbulent convection. It is therefore difficult to predict the intensity of the magnetic field immediately after the Hayashi phase: if the retreat of the convection zone is sufficiently fast, a small fraction of this extremely large flux could remain in the

radiative core. In the case of the sun, the magnetic diffusion time out of the radiative zone is of order of the age of the sun (see Section 3.2.2) or larger, which suggests that a primordial field may still subsists in that region. Recent work by Dudorov *et al.* (1989), following this scenario, gives estimates of a few Gauss for the poloidal field, and from $10^4 - 10^6$G for the toroidal field in the radiative zone. Also, steady dynamo action during the Hayashi phase may actually keep the magnetic flux within the star to a significantly high level throughout the Hayashi phase.

Various estimates of the strength of the primordial field can be found in the extensive review by Mestel & Weiss (1987); they range from a few G to 10^5G for the poloidal field in the solar core. Other recent estimates are based on different approaches: Hinata (1986) proposes that the propagation of Alvén waves from the convection zone to the radiative zone implies the presence of "a few-thousand-Gauss complicated magnetic field with a spectrum $B(k)$= const $k^{1/3}$"; Boruta (1996) suggested that observations of the asymmetry in the solar cycle may provide more stringent limits on the intensity of a poloidal field in the core, and derived an upper limit of about 30 G. In any case, this review seems to suggest that it is not unreasonable to expect a field of order of 1 G or more in the solar radiative zone.

3.2.2 Dynamo penetration

It is often believed that magnetic fields in the sun (and in particular magnetic flux tubes) are permanently created by a dynamo process. The dynamo action results from the interaction between small-scale turbulence, differential rotation and large-scale magnetic fields. Small-scale turbulence with a finite helicity (which is usually the case in a rotating fluid, provided the Rossby number is sufficiently large) can twist azimuthal fields into poloidal fields. Differential rotation then stretches the poloidal field in the azimuthal direction; this whole process might then result in exponential growth of a small seed field, until saturation occurs. The most favourable conditions for the existence of a dynamo occur at the base of the convection zone, which contains

both turbulence and strong radial shear. Assuming such a dynamo indeed exists, the question is then, how far down may the magnetic field propagate?

The dynamo field at the base of the convection zone cannot be observed directly. However, flux tubes originating from this region rise buoyantly and appear at the surface, yielding valuable information about the amplitude fluctuations and the spatial distribution of the field. It is observed that the surface magnetic field undergoes an aperiodic cycle with a mean period of 22 years, and is also subject to significant amplitude fluctuations. A strictly periodic field could not propagate far into the radiative zone, since each half period would be cancelled almost exactly by the next one, leaving a signal that is exponentially damped within the skin depth $l = \sqrt{2\eta/\omega}$ (where η is the diffusivity of the medium and ω the frequency of the cycle), which is roughly 4 km. However, random fluctuations in amplitude or phase do not cancel completely, and can therefore diffuse into the radiative interior as a random walk process, as first proposed by Mestel & Weiss (1987).

The diffusion of the random component of the field, will first be studied. This can be addressed without discussing the issue of the amplitude of the dynamo field since the diffusion problem is intrinsically linear.

3.2.2.1 Diffusion of random fluctuations

The radiative zone is first assumed to have a constant magnetic diffusivity η_0 (the value of η_0, and the relaxation of the assumption that η_0 be constant, will be discussed later), and all kinds of fluid motion are neglected. With these approximations, the magnetic induction equation reduces to a diffusion equation:

$$\frac{\partial \boldsymbol{B}}{\partial t} = \eta_0 \nabla^2 \boldsymbol{B} \ . \tag{3.8}$$

Only the propagation of the poloidal field $\boldsymbol{B}_{\rm p}$ will be considered. Although dynamical coupling would normally prevent the toroidal and poloidal fields from decaying independently, this discussion will follow that of Mestel & Moss (1983) in adopting the approximation of a freely diffusing poloidal field. Then the variation of the toroidal field will be determined by the solution for the poloidal field, by requiring that the magnetic field should be force-free. The toroidal field will not be considered here however, since only the poloidal field can enforce uniform rotation. Hence one can set $\boldsymbol{B} = \boldsymbol{B}_{\rm p}$ in equation (3.8).

The dynamo field at the base of the convection zone, which is used as a boundary condition for the diffusion process in the radiative interior, is presumed to have a dipolar variation, and its amplitude is B_0. The case of a higher multipolar configuration is treated later; the results are qualitatively similar. The time variation of the "boundary field" should represent only the fluctuations of the cycle, since the periodic component is damped within a skin depth of about 4 km. Also, for simplicity, only the amplitude fluctuations will be taken into account, on the grounds that treating the phase fluctuations as well would lead to a very similar result, although the calculation is less easy to carry out. In this simple model, the fluctuations in the field imposed at the boundary will be modeled with a series of step-functions, of constant amplitude and length, but of random sign:

$$\sum_{n=0}^{N} X_n B_0 \Theta(t - n\delta)\Theta[\delta - (t - n\delta)] \ , \tag{3.9}$$

where δ=11 years, B_0 is the average amplitude of the deviation from sinusoidal variation, Θ is a Heaviside function, and the random variable X_n is a Bernoulli variable which can take the values -1 or $+1$. This process is comparable to a random walk process. Finally, the field at the boundary is assumed to lie predominantly in the latitudinal direction. It is not possible, since $\boldsymbol{B}$ is solenoidal, to impose both the radial and latitudinal components of the field at the boundary. The latitudinal direction has been chosen mostly for reasons of simplicity; it is indeed mathematically easier to impose the amplitude of

B_θ as a boundary condition than the amplitude of B_r. The restriction has no significant influence on the final result.

The foregoing remarks and assumptions justify the following boundary condition, expressed with respect to spherical polar coordinates (r, θ, ϕ):

$$B_\theta(r_c, \mu, t) = \sum_{n=0}^{\infty} X_n B_0 \Theta(t - n\delta)\Theta[(n+1)\delta - t]\sqrt{1-\mu^2} \ , \quad (3.10)$$

where B_θ is the latitudinal component of the magnetic field, $\mu = \cos\theta$, $r_c \simeq 5{\times}10^{10}$ cm is the radius of the radiative zone; the spatial variation $\sqrt{1-\mu^2}$ is that appropriate to a dipole field. The radial component of the field B_r must be left unspecified.

Diffusion of a step-function field

Linearity of the problem ensures that the final solution can be obtained by considering the propagation of a single step-function term, and then adding together many such solutions with the corresponding delays.

The boundary condition used can therefore be simplified for the moment to

$$B_\theta(r_c, \mu, t) = B_0 \Theta(t)\Theta(\delta - t)\sqrt{1-\mu^2} \ , \quad (3.11)$$

which describes how at $t = 0$, a latitudinal field is applied to the boundary of the initially magnetic-free radiative zone. Using Chandrasekhar's (1956) formalism for an axisymmetric system, the poloidal field $\boldsymbol{B}$ is represented in terms of the potential P:

$$\boldsymbol{B} = \nabla{\times}(r \ \sin\theta P \hat{\boldsymbol{e}}_\phi) \ . \quad (3.12)$$

Substitution into equation (3.8) then gives

$$\frac{\partial^2 P}{\partial r^2} + \frac{4}{r}\frac{\partial P}{\partial r} + \left(\frac{1-\mu^2}{r^2}\right)\frac{\partial^2 P}{\partial \mu^2} - \frac{4\mu}{r^2}\frac{\partial P}{\partial \mu} = \frac{1}{\eta_0}\frac{\partial P}{\partial t} \ . \quad (3.13)$$

The boundary conditions of the problem allow a separation of variables into

$$P(r,\mu,t) = R(r,t)G(\mu) \ . \tag{3.14}$$

The components of the field then depend on R and G in the following way:

$$B_r = -R(r,t)\frac{\partial}{\partial\mu}\left[(1-\mu^2)G(\mu)\right], \tag{3.15}$$

$$B_\theta = -G(\mu)\sqrt{1-\mu^2}\frac{1}{r}\frac{\partial}{\partial r}\left[r^2R(r,t)\right] \ , \tag{3.16}$$

and equation (3.13) can be separated into the following equations for $R(r,t)$ and $G(\mu)$:

$$(1-\mu^2)\frac{\partial^2 G}{\partial\mu^2} - 4\mu\frac{\partial G}{\partial\mu} = -\lambda^2 G \ , \tag{3.17}$$

$$\frac{\partial^2 R}{\partial r^2} + \frac{4}{r}\frac{\partial R}{\partial r} - \frac{1}{\eta_0}\frac{\partial R}{\partial t} = \frac{\lambda^2}{r^2}R \ . \tag{3.18}$$

Equation (3.17) is the eigenvalue equation for the Gegenbauer polynomial $C_k^{(3/2)}(\mu)$ with eigenvalue $\lambda^2 = k(k+3)$, where k is a non-negative integer.

The complete solution is therefore given by

$$P(r,\mu,t) = \sum_{k=0}^{\infty} A_k R_k(r,t) G_k(\mu) \ , \tag{3.19}$$

where $G_k(\mu) = C_k^{(3/2)}(\mu)$ and R_k satisfies equation (3.18). Since the boundary condition for a dipole configuration is given by equation (3.11), in the light of equation (3.16) it follows straightforwardly that only $G_0(\mu)$ is non-zero, and that

$$G(\mu) = G_0(\mu) = 1 \text{ with } \lambda_0 = 0 \ . \tag{3.20}$$

Hence, for the dipole configuration, the problem is greatly simplified, and there remains only one equation to solve, namely

$$\frac{\partial^2 R}{\partial r^2} + \frac{4}{r}\frac{\partial R}{\partial r} - \frac{1}{\eta_0}\frac{\partial R}{\partial t} = 0 \ , \tag{3.21}$$

with boundary condition

$$\frac{1}{r}\frac{\partial}{\partial r}\left[r^2 R(r,t)\right]\Big|_{r=r_c} = -B_0\Theta(t)\Theta(\delta - t) \ . \tag{3.22}$$

This problem can be solved using the Laplace transform method (described for instance by Carslaw & Jaeger (1959)). The solution must be split into two distinct time intervals: $t \leq \delta$ and $t > \delta$. For times t smaller than the duration δ of the step-function the solution corresponds simply to the inward diffusion of constant magnetic field on the surface of the sphere (see also Carslaw & Jaeger (1959)). However, that solution is not relevant for this study, since only times of order of the age of the sun are being considered. For $t > \delta$ the solution is:

$$\begin{aligned} P(r,\theta,t) &= 2B_0\left(\frac{r_c}{r}\right)^{3/2} \\ \times &\sum_{i=1}^{\infty} \frac{J_{3/2}(j_i\frac{r}{r_c})\exp\left(-j_i^2\frac{t}{\tau}\right)\left[\exp\left(j_i^2\frac{\delta}{\tau}\right)-1\right]}{(j_i^2+2)J_{3/2}(j_i)} \ , \end{aligned} \tag{3.23}$$

where $\tau = r_c^2/\eta_0$ is the diffusion timescale, and the coefficients j_i are the solutions of

$$j_i J_{1/2}(j_i) = J_{3/2}(j_i) \ . \tag{3.24}$$

The j_i can be obtained numerically, and the first five are listed in Table 3.1.

Finally, the field in the interior is given by

$$\frac{B_r}{\cos\theta} = 4\sum_{i=1}^{\infty} D_i(t)\left(\frac{r_c}{r}\right)^{3/2} J_{3/2}\left(j_i\frac{r}{r_c}\right) \ , \tag{3.25}$$

Table 3.1: The eigenvalues j_i for $i \leq 5$, given to 10^{-5} accuracy.

i	j_i
1	2.74370
2	6.11676
3	9.31661
4	12.48593
5	15.64386

$$\frac{B_\theta}{\sin\theta} = 2\sum_{i=1}^{\infty} D_i(t) r_{\rm c}^{3/2} \left[\frac{J_{3/2}(j_i \frac{r}{r_{\rm c}})}{r^{3/2}} - \frac{j_i}{r_{\rm c}} \frac{J_{1/2}(j_i \frac{r}{r_{\rm c}})}{r^{1/2}} \right] , \qquad (3.26)$$

where $D_i(t)$ is the following function of time:

$$D_i(t) = B_0 \frac{\exp\left(j_i^2 \frac{\delta}{\tau}\right) - 1}{(j_i^2 + 2) J_{3/2}(j_i)} \exp\left(-j_i^2 \frac{t}{\tau} \right) , \qquad (3.27)$$

for $t > \delta$.

Diffusion time, and numerical evaluation of the solution:

The numerical evaluation of the solution requires the choice of the diffusion timescale, through the choice of the constant diffusivity η_0. Indeed, since the damping factor is $\exp\left(-j_i^2 t/\tau\right)$, the result will depend strongly on the diffusion time τ. Spitzer (1962) gives the expression for the resistivity σ^{-1} of a fully ionized plasma as $\sigma^{-1} = 6.53 \times 10^{12} \ln\Lambda \; T^{-3/2} {\rm cm}^2 {\rm s}^{-1}$, where $T(r/r_{\rm c})$ is the temperature and $\ln\Lambda$ is an electrostatic shielding factor tabulated by Spitzer, which varies from about 2.5 in the solar core to roughly 3.5 at $r = r_{\rm c}$. The relation $\eta = 1/4\pi\sigma$ therefore yields

$$\eta(r/r_{\rm c}) = 5.2 \times 10^{11} \ln\Lambda \; T^{-3/2} {\rm cm}^2 {\rm s}^{-1} . \qquad (3.28)$$

Using the temperature and density profile given by Stix (1989), equation (3.28) yields the following range of values of the diffusivity be-

tween the centre and the outer edge of the radiative zone:

$$20 \text{ cm}^2\text{s}^{-1} \lesssim \eta \lesssim 645 \text{ cm}^2\text{s}^{-1} \ . \tag{3.29}$$

This shows the danger of the constant-diffusivity approximation. A better approximation to the more realistic case of non-constant diffusivity can be obtained using the new coordinate r_η defined by

$$\frac{r_\eta}{r_\mathrm{c}} = \frac{\int_0^{r/r_\mathrm{c}} \eta^{1/2}(x)dx}{\eta_0^{1/2}} \ , \tag{3.30}$$

which captures the influence of the variation of η on the highest spatial derivative of the field. The solution to the diffusion equation with a constant diffusivity η_0 approximates the real solution provided this scaling is used. The value of η_0 is obtained from the requirement that r_η/r_c varies between 0 and 1. Thus,

$$\eta_0 = \left(\int_0^1 \eta^{1/2}(x)dx \right)^2 \simeq 150 \text{ cm}^2 \text{ s}^{-1} \ , \tag{3.31}$$

using equation (3.28) and the temperature and density profiles given by Stix (1989). This corresponds to

$$\tau = 1.65 \times 10^{19} \text{ s} \simeq 5 \times 10^{11} \text{ y} \ . \tag{3.32}$$

The well known Cowling decay time (that is, the timescale with which a primordial large-scale magnetic field would decay) is roughly given by $\tau_\mathrm{C} = r_\odot^2/\eta_0 j_1^2$ (although since the turbulent motions in the convection zone tend to destroy the field in this region, a better estimate would be $\tau'_\mathrm{C} = r_\mathrm{c}^2/\eta_0 j_1^2 \approx \tau_\mathrm{C}/2$). With the chosen estimate for η_0, the Cowling time is $\tau_\mathrm{C} \approx 4 \times 10^{18}$ s $\approx 1.2 \times 10^{11}$ y. The discrepancy with the timescale of 10^{10} years quoted by Cowling (1957) is due to corrections in the conductivity calculations introduced by Spitzer in 1962 (which increased the diffusive timescale by a factor of 5) and the choice of η_0 as an appropriate intermediate value between the diffusivity at the centre of the sun and that at the outer edge of the radiative zone.

The best estimate for the decay timescale of a large scale magnetic field in the radiative zone of the sun is therefore probably given by $\tau_{\rm d} = \tau/j_1^2 = r_{\rm c}^2/\eta_0 j_1^2 = 7 \times 10^{10}$ y.

Fig. 3.1 shows the propagation into the interior of the radial component of the magnetic field, B_r, for the chosen diffusion time τ, while Fig. 3.2 shows the variation of B_r at several fixed radii in the radiative zone.

Random walk process:

The total magnetic field in the radiative interior $\boldsymbol{B}_{\rm in}$ is the sum of the isolated step-function fields $\boldsymbol{B}$. After N periods of the oscillating boundary field, $t = N\delta$ and

$$\boldsymbol{B}_{\rm in}(r,\theta,t) = \sum_{n=0}^{N} X_n \boldsymbol{B}(r,\theta,t-n\delta) \ . \tag{3.33}$$

The expectation value of the field $\boldsymbol{B}_{\rm in}$ is $\boldsymbol{0}$. Since the random variables X_n are presumed to be uncorrelated, the standard deviation for the magnitude of the field is given by

$$B_{\rm rms} = < B_{\rm in}^2(r,\theta,t) >^{1/2} = \sqrt{\sum_{n=0}^{N} B^2(r,\theta,t-n\delta)} \ , \tag{3.34}$$

where $B_{\rm in} = |\boldsymbol{B}_{\rm in}|$ and $B = |\boldsymbol{B}|$. This expression has been evaluated numerically using the results obtained in equation (3.23). The results for each component of the field at the present time ($t = 1.5 \times 10^{17}$ s) are shown in Fig. 3.3, using the diffusion time given by equation (3.32). The results summarized in Fig. 3.3 show how the boundary field is damped within the radiative zone. Firstly, very close to the boundary only a very small fraction of the magnetic flux can penetrate the radiative zone each cycle, due to the large diffusion time. Note indeed the decrease by four orders of magnitude between the boundary value B_0 and the maximum value of the latitudinal field inside the radiative zone. Also, as expected from the boundary conditions, the

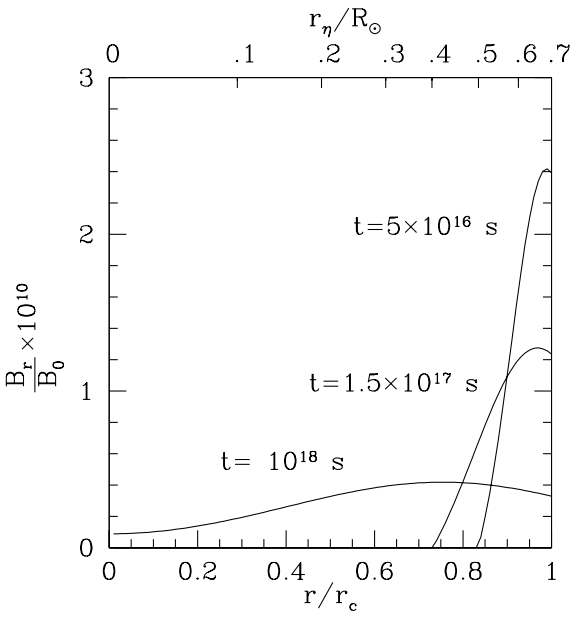

Figure 3.1: Propagation of the radial component of the magnetic field, assuming the sun to have remained in its current state, with a single step-function boundary condition. This plot shows the latitudinal average of B_r over a quadrant as a function of radius, at various times including the present age of the sun ($t = 1.5 \times 10^{17}$ s). The field at $t = 10^{18}$ is presented for heuristic purposes. The lower axis presents the solution as it has been computed for the constant-diffusivity case. In order to get a better approximation to the variable-diffusivity case, the reader should refer to the upper axis *(from Garaud, (1999))*.

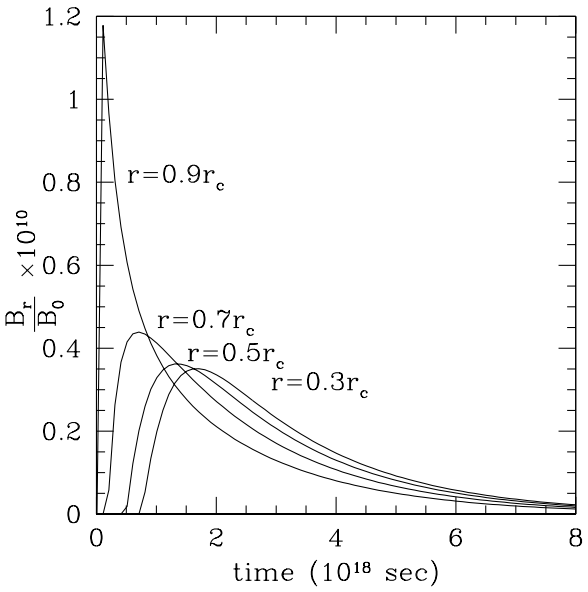

Figure 3.2: Propagation of the radial component of the magnetic field, with a single step-function boundary condition. This plot shows the latitudinal average of B_r over a quadrant as a function of time, as calculated for the constant-diffusivity case, at four different radii *(from Garaud, (1999))*.

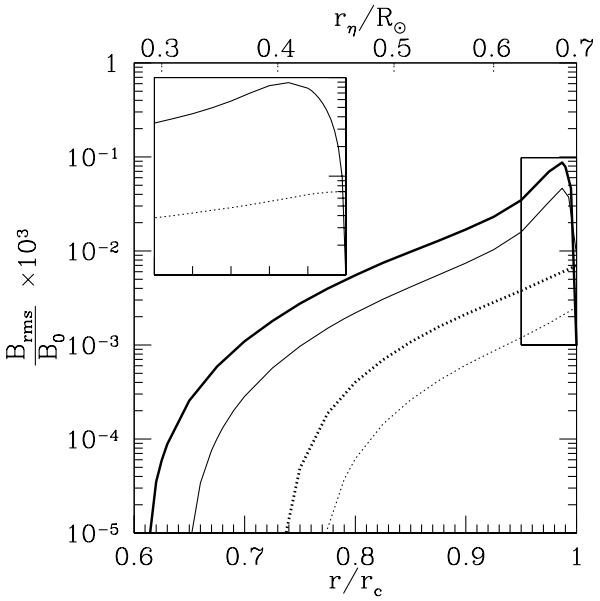

Figure 3.3: Rms value of the intensity of the field as a function of radius. For each component of the field, the latitudinal average over a quadrant is presented. The thick lines correspond to the dipolar case, whereas the thinner ones correspond to the quadrupolar case. The continuous lines correspond to the latitudinal component of the field and the dotted lines correspond to the radial component. The lower axis presents the solution as it has been computed for the constant-diffusivity case. In order to get a better approximation of the variable-diffusivity case, the reader should refer to the upper axis. As it is shown in Section 3, a reasonable value of B_0 is 10^3 G; the scaling used on the vertical axis therefore allows the result to be read *directly* from this plot. The box in the upper left corner is an expanded view of the dipolar field in the rectangular area at the right of the plot. As expected from the chosen boundary condition, the latitudinal component of the field quickly drops to 0 near the outer boundary, whereas the radial component reaches a constant value *(from Garaud, (1999))*.

latitudinal field drops to 0 at the top of the radiative zone. Secondly, this plot also shows the radial scale of variation of the magnetic field, as the latter is reduced again by several orders of magnitude within the outer third of the radiative zone's radius.

Quadrupolar and higher-order multipolar configurations:

In the case where the dynamo field produces a higher-order multipolar configuration, the equations are changed in the following way:

1. The projection of the boundary condition given by equation (3.11) onto the latitudinal eigenstates $G_k(\mu)$ yields the coefficients A_k in equation (3.19), provided the boundary condition for the radial function is chosen to remain the same for each R_k as in equation (3.22). As an example, for an axisymmetric *quadrupolar* configuration where the latitudinal component of the boundary field is proportional to $\sin\theta\cos\theta$, the only non-vanishing term is for $k = 1$, with A_1=1/3 and $G_1(\mu) = 3\mu$.

2. The solution to equation (3.13) is now

$$P(r,\theta,t) = 2B_0 \sum_{k=0}^{\infty} A_k G_k(\mu) \left(\frac{r_c}{r}\right)^{3/2} \times \sum_{i=1}^{\infty} \frac{J_{n+3/2}(j_{i,k}\frac{r}{r_c})\exp\left(-j_{i,k}^2\frac{t}{\tau}\right)\left[\exp\left(j_{i,k}^2\frac{\delta}{\tau}\right)-1\right]}{[j_{i,k}^2+(k+1)(k+2)]J_{k+3/2}(j_{i,k})} \quad (3.35)$$

   where the coefficients $j_{i,k}$ are the solutions of

$$j_{i,k}J_{k+1/2}(j_{i,k}) = (k+1)J_{k+3/2}(j_{i,k})\ . \quad (3.36)$$

With this result, it can be shown numerically (cf Fig. 3.3) that the higher-order components of the dynamo field create a magnetic field that is similar in intensity to the dipolar field close to the outer boundary of the radiative zone, but decreases with depth, as expected, on a correspondingly shorter lengthscale.

This section focuses on using the previous result to obtain a numerical estimate of the field in the interior, which requires the determination of the amplitude of the boundary field, B_0. There exists no direct measurement of the poloidal field at the base of the convection zone. However, considerations about the buoyancy instability of flux tubes in the convection zone and comparisons with the observed sunspot rates led Schüssler et al. (1994) to estimate the mean *toroidal* field at the base of the convection zone to be of order of a few times 10^4G. This estimate can be used together with some simple assumptions to derive an order of magnitude of the amplitude of the poloidal field in the same region.

The model considered here assumes that the poloidal field is generated near the base of the convection zone by the action of cyclonic turbulence. This field is pumped downwards by turbulent motions into the overshoot region (around the outer edge of the tachocline) where it is sheared into a strong toroidal field by the differential rotation, through the advection equation:

$$\frac{\partial \boldsymbol{B}}{\partial t} = \nabla \times (\boldsymbol{u} \times \boldsymbol{B}) + \eta \nabla^2 \boldsymbol{B} \ . \tag{3.37}$$

In this region of very large shear the diffusion term is negligible compared to the advection term, so that

$$\frac{\partial \boldsymbol{B}}{\partial t} = \nabla \times (\boldsymbol{u} \times \boldsymbol{B}) \ . \tag{3.38}$$

It is reasonable to assume that the velocity is due to the rotation only (since the velocity of the meridional circulation is negligible):

$$\boldsymbol{u} = r \ \sin\theta \Omega(r, \theta) \hat{\boldsymbol{e}}_\phi \ . \tag{3.39}$$

where $\hat{\boldsymbol{e}}_\phi$ is the unit vector in the ϕ direction. The ϕ component of equation (3.38) is then

$$\frac{\partial B_\phi}{\partial t} = r \ \sin\theta B_r \frac{\partial \Omega}{\partial r} + \ \sin\theta B_\theta \frac{\partial \Omega}{\partial \theta} \ , \tag{3.40}$$

which yields the order-of-magnitude relation

$$< \sin\theta > r_{\rm c}\frac{\Delta\Omega}{\Delta r}B_r + < \sin\theta > B_\theta\frac{\Delta\Omega}{\Delta\theta} \simeq \frac{2\pi}{t_{\rm dyn}}B_\phi \ , \qquad (3.41)$$

where $t_{\rm dyn}$ is the period of variation of B_ϕ, which would be of order of 2δ (22 years). On the other hand, the presumed axisymetry of the system implies that the poloidal field should be divergence-free, giving the order-of-magnitude relation

$$\Delta\theta r_{\rm c}B_r \simeq \Delta r B_\theta \ . \qquad (3.42)$$

These two equations combine to give

$$B_\theta = \frac{1}{2}\frac{\Delta\theta}{< \sin\theta >}\frac{2\pi}{\Delta\Omega\ t_{\rm dyn}}B_\phi \ . \qquad (3.43)$$

Since the magnetic activity is concentrated around the equatorial regions, with a maximum latitudinal extension of 30°, it is reasonable to chose $< \sin\theta >= 0.25$ (which corresponds to a latitude of 15°, and $\Delta\theta = \pi/6$. Helioseismic measurements (Thompson et al. 1996) show that typically $\Delta\Omega/2\pi \simeq 10^{-8}{\rm s}^{-1}$ around the equator, which finally gives the following relation between B_θ and B_ϕ:

$$B_\theta \approx 0.15 B_\phi \ . \qquad (3.44)$$

Hence the order-of-magnitude estimate for the amplitude of the B_ϕ dynamo field of about 5×10^4G gives the following order-of-magnitude estimate for the periodical component of B_θ:

$$B_{\rm per} \approx 7\times10^3{\rm G} \ . \qquad (3.45)$$

Magnetic activity measurements suggest that the variations of the amplitude of the field from cycle to cycle can be significant, and are on average of order of 10% of the signal, which would in this case lead to $B_0 = 7\times10^2$ G. Since this is only an order-of-magnitude

approximation, it is quite reasonable to choose for simplicity

$$B_0 = 10^3 \mathrm{G} \ . \tag{3.46}$$

With this estimate for B_0, the intensity of the field in the interior can be read directly from Fig. 3.3.

3.2.3 Discussion

Under the assumption of uniform diffusivity, and using a rough estimate of about 10^4 G for the value of the poloidal component of the dynamo field as an outer boundary condition, it was shown that the propagation of random fluctuations of the magnetic field may build up a large-scale poloidal field in the radiative zone with an intensity as shown in Fig. 3.3. The intensity of the field decreases from about 10^{-1}G just below the convection zone (at roughly $0.69 r_\odot$), to 10^{-3}G at about $0.35 r_\odot$. The thickness of the tachocline has been inferred to be of order of 2% of the solar radius (Elliot & Gough (1999)). Assuming that the tachocline circulation has no effect on the propagation of the field, it can be deduced from Fig. 3.3 that a field of about 10^{-1}G can be expected in the tachocline region ($0.68 r_\odot \lesssim r \lesssim 0.7 r_\odot$) as a result of the random diffusion of the dynamo field. Deeper in the core (below $0.35 r_\odot$), this field rapidly becomes negligible compared even to the interstellar field. These estimates have been derived using the standard deviation of the random walk; it is impossible to predict the polarity of the field. Since the increment in the field at each step is extremely small compared to the overall field, the time variation of the field is quite smooth.

The evaluation of the amplitude of a primordial field, as was reviewed previously, is more controversial; however, most authors seem to agree that amplitudes of order of 1 G or more can be expected deep in the radiative zone. This value is much larger than the amplitude of the field expected from the penetration of a dynamo field. The preceding discussion has therefore two important consequences.

1. Mestel & Weiss (1987) showed through timescale arguments that

diffusive and dynamical magnetic instabilities probably allow the shear to persist in the inner core ($r \lesssim 0.2 r_\odot$) provided the poloidal field does not exceed values of about 10^{-3}G. Their argument can easily be extended to the whole of the radiative zone, and yields a similar result. The observed uniform rotation deep in the radiative zone therefore strongly suggests the presence of a primordial field, since the contribution of the random fluctuations of the dynamo field in this region is negligible.

2. Dynamo theory has recently suggested that the solar dynamo should lie in the vicinity of the outer edge of the tachocline (Parker (1993)), and maintains magnetic fields of order of 10^4 G or more. The calculation presented in this paper shows that the inward diffusion of the dynamo may lead to the presence of magnetic fields of about 0.1 G or less near the top the tachocline, quickly decaying with depth. This estimate can be used to discuss the importance of the effects of the dynamo field on the dynamics of the tachocline (see, for example, Gough & McIntyre (1998), and also section 3.3.2).

3.3 Previous MHD models for the tachocline

Having established that any large-scale magnetic field of significant amplitude present in the radiative zone of the sun must be of primordial origin, and that such a primordial magnetic fields is indeed likely to be present in the radiative zone with a reasonably large amplitude, one may now turn to the problem of studying the effect of such a field on the solar angular velocity profile in the radiative zone when a latitudinal shear is imposed by the convection zone. Since the magnetic diffusion timescale is largest for the dipolar component of the magnetic field, it will from now on be assumed that the primordial field present in the radiative zone has a dipolar structure only.

The MHD interaction of fluid flows and magnetic fields is an intrinsically nonlinear process, since both the Lorentz force in the momentum equation, and the advection term in the advection equation are nonlinear. Observations show that deep in the interior the magnetic forces

dominate, by imposing uniform rotation, whereas in the tachocline region the fluid motions dominate, as it can be seen through the presence of a strong shear. These two limits suggest the existence of an intermediate region where the interaction between the magnetic field and the fluid flows is extremely nonlinear. This simple statement stresses the main difficulty of any study of the tachocline, namely, the nonlinearity of the problem. Owing to this mathematical challenge, only two MHD models of the tachocline predate my own work. These are the works of Rüdiger & Kitchatinov (1997) and Gough & McIntyre (1998) respectively. These two approaches are now briefly presented.

3.3.1 Rüdiger & Kitchatinov (1997)

Rüdiger & Kitchatinov (1997) proposed the first MHD model of the differential rotation in the solar interior. The model describes the action of a large-scale poloidal field on the angular velocity of the radiative zone when a latitudinal shear is imposed by the convection zone. In order to simplify the mathematical problem, they neglect the existence of meridional motions, which would advect both the poloidal field and angular momentum. As a result, the poloidal field is fixed, and the system needs only be solved for the angular velocity profile and the azimuthal field. Additionally, the system is assumed to be axisymmetric and in a steady state, and the fluid is incompressible. The viscosity and magnetic diffusivity within the radiative zone are derived from

$$\begin{aligned} \eta &= 10^{13} T^{-3/2} \text{ cm}^2 \text{ s}^{-1} , \qquad (3.47) \\ \nu &= \nu_{\text{rad}} + \nu_{\text{mol}} = 2.5 10^{-25} \frac{T^4}{\kappa\rho} \text{ cm}^2 \text{ s}^{-1} + 1.2 10^{-16} \frac{T^{5/2}}{\rho} \text{ cm}^2 \text{ s}^{-1} . \end{aligned}$$

Under these assumptions, the angular velocity and the toroidal field are calculated according to the azimuthal component of the momentum equation and the azimuthal component of the advection-diffusion

equation, namely:

$$r\left(\frac{\partial\Omega}{\partial\theta}\frac{\partial A}{\partial r}-\frac{\partial A}{\partial\theta}\frac{\partial\Omega}{\partial r}\right) = \eta(r)\frac{\partial}{\partial\theta}\left[\frac{1}{\sin\theta}\frac{\partial}{\partial\theta}\left(B_\phi\,\sin\theta\right)\right] + r\frac{\partial}{\partial r}\left[\eta(r)\frac{\partial}{\partial r}\left(rB_\phi\right)\right]\ , \qquad (3.48)$$

$$\frac{\rho(r)\nu(r)}{\sin^3\theta}\frac{\partial}{\partial\theta}\left(\sin^3\theta\frac{\partial\Omega}{\partial\theta}\right)+\frac{1}{r^2}\frac{\partial}{\partial r}\left(r^4\rho(r)\nu(r)\frac{\partial\Omega}{\partial r}\right) = \frac{1}{4\pi r^2\,\sin^3\theta}\left[r\frac{\partial A}{\partial r}\frac{\partial}{\partial\theta}\left(B_\phi\,\sin\theta\right)-\,\sin\theta\frac{\partial A}{\partial\theta}\frac{\partial}{\partial r}\left(rB_\phi\right)\right] \qquad (3.49)$$

where the flux function A corresponding to the poloidal field is given by

$$\boldsymbol{B}_p=\nabla\times\left(\frac{A}{r\,\sin\theta}\hat{\boldsymbol{e}}_\phi\right)=\left(\frac{1}{r^2\,\sin\theta}\frac{\partial A}{\partial\theta},-\frac{1}{r\,\sin\theta}\frac{\partial A}{\partial r}\right)\ , \qquad (3.50)$$

with

$$A=B_{\rm c}\frac{r^2}{2}\left(1-\frac{r}{r_{\rm c}}\right)^q\,\sin^2\theta\ . \qquad (3.51)$$

The parameter $B_{\rm c}$ is the value of the magnetic field at the centre, and q parameterizes the radial profile: the larger q, the more concentrated the field is around the neutral points. The angular velocity at the top of the radiative zone is imposed by that of the convection zone, and is given by

$$\Omega_{\rm cz}(\theta)=\Omega_{\rm eq}(1-a_2\,\cos^2\theta-a_4\,\cos^4\theta)\ , \qquad (3.52)$$

where reasonable values for a_2 and a_4 are $a_2=0.15$ and $a_4=0.15$. The toroidal field vanishes at the edge of the radiative zone. This results from the assumption that the convection zone behaves as an insulating medium. These two boundary conditions close the system with the regularity conditions at $r=0$.

Rüdiger & Kitchatinov obtain the following results: as expected the

presence of a large-scale poloidal field in the radiative zone imposes an almost uniform rotation throughout the interior, with a magnetic shear layer near the base of the convection zone which matches the inner solution to the boundary conditions. The thickness of the boundary layer varies according to the intensity and geometrical structure of the interior field. Typically, an interior field of about 10^{-3} G is sufficient to reduce the thickness of the boundary layer to a few per cent of the radiative zone, which represents the observed thickness of the tachocline. Also, the maximum toroidal field obtained is of order of 200 G.

The model proposed by Rüdiger & Kitchatinov is fairly successful in reproducing some of the aspects of the tachocline. In particular, the dipolar structure of the field results in a rather thicker tachocline at the poles than near the equator, a feature that may be suggested by some of the observations. However, there are some very important shortfalls to their assumptions. Firstly, the whole dynamical structure of the system (and in particular the circulation) has been neglected. As a result, such a system could not realistically be in a steady state. In particular, Lorentz forces in the latitudinal direction have been neglected; these would normally drive a circulation which would in turn advect angular momentum and change the angular velocity distribution. Also the effects of compressibility and stratification below the convection zone may be important but have not been considered in this work. Secondly, the stability of the magnetic field structure has not been assessed. It is however likely that such a large concentration of toroidal field in the tachocline is unstable to axisymmetric and even non-axisymmetric perturbations (see Gilman & Fox (1997) and subsequent papers).

3.3.2 A dynamical model of the tachocline: Gough & McIntyre (1998)

Gough & McIntyre (1998) approached the problem from a different angle. They recognized the importance of taking the dynamical structure of the tachocline into account, including the effects of a meridional

circulation and compressibility, and focused on laying out the foundations of the best possible model rather than attempt to fully solve it. Through a basic boundary layer analysis, they derive scaling laws between various quantities, such as the amplitude of the interior field and the thickness of the tachocline.

The principal assumptions of the model proposed are as follows. As before, the system is assumed to be axisymmetric, and in a steady state. The azimuthal and meridional fluid motions are assumed to be slow, and the perturbations to the hydrostatic equilibrium structure of the radiative zone are assumed to be very small. As a result, a Boussinesq approximation of the fully compressible equation is used (see Chapter 2), and nonlinear terms in the meridional circulation are neglected. Finally, the effects of the oblateness of the sun and of viscosity on the dynamical structure of the tachocline are also assumed to be negligible .

Within these approximations, the MHD equations take the following form. The mass conservation equation and axisymetry suggests the usefulness in introducing the stream function $\psi(r,\theta)$ such that

$$\begin{aligned} \rho_{\rm h}(r)u_r &= \frac{1}{r^2\ \sin\theta}\frac{\partial\psi}{\partial\theta}\ , \\ \rho_{\rm h}(r)u_\theta &= -\frac{1}{r\ \sin\theta}\frac{\partial\psi}{\partial r}\ . \end{aligned} \tag{3.53}$$

The angular momentum equation yields

$$2\rho_{\rm h}(r)\Omega_{\rm c}(\ \sin\theta u_r + \ \cos\theta u_\theta) = \frac{B_\theta}{r\ \sin\theta}\frac{\partial}{\partial\theta}(\ \sin\theta B_\phi) + \frac{B_r}{r}\frac{\partial}{\partial r}(rB_\phi)\ . \tag{3.54}$$

The energy equation is rewritten as

$$\frac{c_{\rm p}(r)T_{\rm h}(r)N^2(r)}{g(r)}\frac{1}{r^2\ \sin\theta}\frac{\partial\psi}{\partial\theta} = \nabla\cdot(K_{\rm t}(r)\nabla T)\ . \tag{3.55}$$

The thermal wind equation yields

$$-\frac{\cos\theta\,\sin\theta}{r}\frac{\partial}{\partial r}\left(r^2\tilde{\Omega}\right)=\frac{g(r)}{2\Omega_{\rm c}rT_{\rm h}(r)}\frac{\partial T}{\partial\theta}+\nabla\times\left(\frac{1}{\rho_{\rm h}}\boldsymbol{j}\times\boldsymbol{B}\right)_{\phi}\ , \quad (3.56)$$

and finally, the poloidal component of the advection-diffusion equation is

$$u_rB_\theta-u_\theta B_r=\eta\left(\frac{1}{r}\frac{\partial}{\partial r}(rB_\theta)-\frac{1}{r}\frac{\partial B_r}{\partial\theta}\right)\ , \quad (3.57)$$

and the azimuthal component is

$$\begin{aligned}&\frac{1}{r}\frac{\partial}{\partial r}(r^2\,\sin\theta\tilde{\Omega}B_r-ru_rB_\phi)-\frac{1}{r}\frac{\partial}{\partial\theta}(u_\theta B_\phi-r\,\sin\theta\tilde{\Omega}B_\theta)\\ =\quad&-\eta\frac{\partial^2B_\phi}{\partial r^2}\ .\end{aligned} \quad (3.58)$$

Gough & McIntyre (1998) proposed to solve this system through the following three-zone model, represented in Fig. 3.4:

1. the radiative interior is held rigid by the presence of a large-scale poloidal magnetic field; in this region, the meridional circulation is negligible as well as the differential rotation.

2. within the tachocline, a meridional circulation is driven by the baroclinicity originating from the shear.

3. near the base of the tachocline, this circulation interacts with the large-scale poloidal field within a very thin magnetic boundary layer; the poloidal field is kept from diffusing outwards due to the advection by the circulation, and the circulation is kept from burying into the convection zone by diffusion.

Dynamical balance within the tachocline provides a relation between the differential rotation applied by the convection zone, the thickness of the tachocline and the velocity of the meridional circulation. Advection-diffusion balance within the magnetic boundary layer provides a relation between the strength of the magnetic field and the velocity of the circulation. Combining these two results yields a relation between the amplitude of the interior magnetic field, the differential rotation and the thickness of the tachocline, which can then be

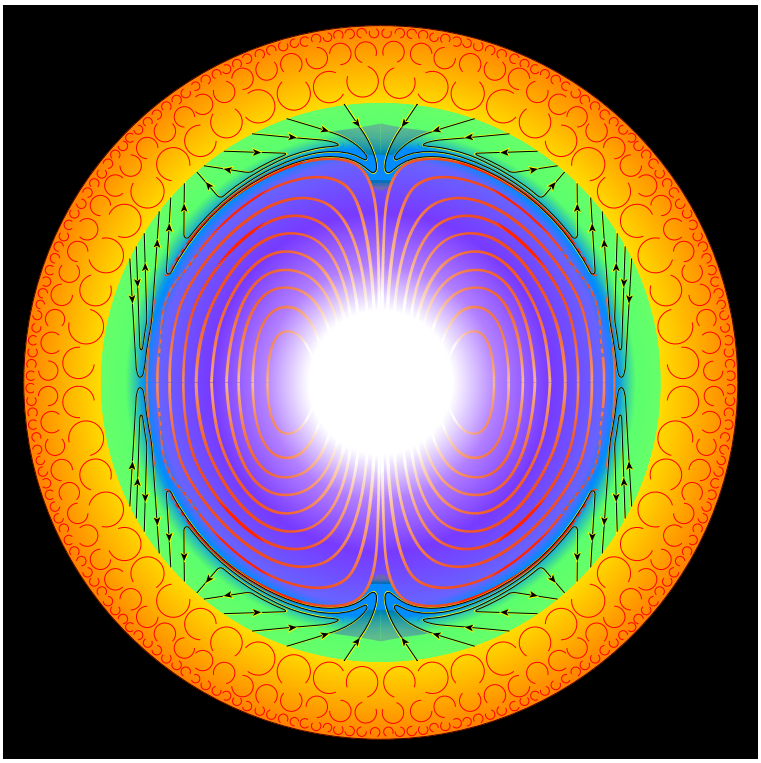

Figure 3.4: Schematic representation of the model proposed by Gough & McIntyre, (1998). The primordial field (thick red lines) imposes a solid-body rotation profile to the radiative zone (white-purple region). The tachocline (in green; its thickness has been largely exaggerated for clarity) is a region of large radial shear, and therefore undergoes large-scale circulatory motions. The arrows represent the tachocline circulation, which follows lines of constant angular momentum. As the relic field slowly diffuses out of the radiative zone, it deflects the circulation within a very thin layer, the magnetic diffusion layer (blue). This interaction results in a net redistribution of angular momentum, within a much thinner region than what could have been expected had only viscous forces been used *(courtesy of D. O. Gough)*.

compared with observations. The following scalings apply: within the tachocline, the circulation is driven by the baroclinicity. Assuming that the magnetic field and the viscosity are negligible, the dominant terms in the thermal wind equations are simply

$$-2r_{\rm c}^2\frac{\partial\tilde{\Omega}}{\partial r}=\frac{g_{\rm h}}{\Omega_{\rm c}T_h}\frac{1}{\cos\theta\,\sin\theta}\frac{\partial T}{\partial\theta}\ . \tag{3.59}$$

In order to derive this scaling, it has been implicitly assumed that the tachocline is thin. The energy equation yields

$$\frac{N^2T_{\rm h}u_r}{g_{\rm h}}\approx\frac{K_{\rm t}}{\rho_{\rm h}c_{\rm p}}\frac{\partial^2T}{\partial r^2}\ . \tag{3.60}$$

Gough & McIntyre show that both equations are still valid within the magnetic boundary layer (in particular, it is shown that the magnetic term in the magnetic boundary layer is negligible compared to the thermal wind term; in the energy equation, the magnetic pressure term is also shown to be negligible). However, the magnetic stresses are essential to the angular momentum balance, which can be rewritten as

$$2\rho_{\rm h}\Omega_{\rm c}\,\cos\theta u_\theta=\frac{B_0}{r\,\sin\theta}\frac{\partial}{\partial\theta}(\,\sin\theta B_\phi) \tag{3.61}$$

if the radial velocity and the radial component of the magnetic field are assumed to be negligible in this region. Finally, the poloidal component of the advection-diffusion equation suggests the scaling

$$u_r\sim\eta/\delta\ , \tag{3.62}$$

where δ is the thickness of the magnetic boundary layer, and the azimuthal component of the advection diffusion equation yields

$$B_0\frac{\partial}{\partial\theta}(\,\sin\theta\tilde{\Omega})=-\eta\frac{\partial^2B_\phi}{\partial r^2}\ . \tag{3.63}$$

In equations (3.61) and (3.63) the magnetic field is assumed to be horizontal and varies little with latitude so that $B_\theta\sim B_0$.

Using the fact that $\nabla\cdot(\rho\boldsymbol{u})=0$, equations (3.59) to (3.63) are re-

duced to

$$\frac{\partial^6 T}{\partial r^6} = \frac{T}{\delta^6} \ , \tag{3.64}$$

where

$$\delta = \left(\frac{2\eta K_{\rm t} \Omega_{\rm c}^2}{r_{\rm c}^2 c_{\rm p} N^2 B_0^2 L^4} \right)^{1/6} r_{\rm c} \ , \tag{3.65}$$

and $1/L$ is the typical angular scale of variation defined by $\frac{\partial}{\partial \theta} \sim L$.

This scaling argument provides the thickness of the magnetic boundary layer, which in turn yields the amplitude of the radial velocity at the base of the tachocline according to equation (3.62). Assuming that within the tachocline $\frac{\partial}{\partial r} \sim \pi/\Delta$ and $\tilde{\Omega} \sim \alpha \Omega_{\rm c}$, this estimate can now be used with equations (3.59) and (3.60) to give a relation between the thickness of the tachocline, and the value of the amplitude of the magnetic field near the base of the tachocline, namely,

$$B_0 \sim \frac{\sqrt{2}\alpha^3 \pi^6}{L^5} \left(\frac{K_{\rm t}}{\rho_{\rm h} c_{\rm p} \eta} \right)^3 \left(\frac{\Omega_{\rm c}}{N} \right)^7 \sqrt{\frac{K_{\rm t} \eta}{\rho_{\rm h} c_{\rm p}}} \left(\frac{\Delta}{r_{\rm c}} \right)^{-9} \ . \tag{3.66}$$

With the values for the parameters in the tachocline described in Table A.1, this reduces to

$$B_0 \sim 5 \times 10^{-15} \left(\frac{\Delta}{r_{\rm c}} \right)^{-9} \ {\rm G} \ , \tag{3.67}$$

so that a tachocline thickness of about 3% of the radius of the convection zone (Elliott & Gough (1999)) requires the presence a magnetic field strength of order of

$$B_0 \sim 1 {\rm G} \tag{3.68}$$

near the base of the tachocline. Also, the characteristic ventilation time for the tachocline is found to be

$$\tau_{\rm v} = \Delta / u_r \sim 3 \times 10^6 \ {\rm y}. \tag{3.69}$$

These results call for the following comments:

1. The amplitude of the magnetic field required to fulfill the dy-

namical equilibrium within the tachocline is of order of 1 G, which is roughly ten times larger than what can be expected from the dynamo diffusion process. The study presented in Section 3.2.2 therefore confirms that the magnetic field must be of primordial origin, and also suggests that the contribution from the dynamo field to the dynamics of the tachocline can be neglected in a first approximation.

2. The ventilation time of the tachocline circulation is sufficiently small that the mixing of material and angular momentum can be assumed to be instantaneous on an evolutionary timescale, which confirms the assumptions proposed by Elliott & Gough (1999) in their model for helium mixing within the tachocline. Also, such a model provides a reasonable explanation for the observed abundances of light elements at the surface: mixing is efficient within the tachocline (above a $0.67r_\odot$), but strongly suppressed by the presence of a large-scale magnetic field below the tachocline (see section 1.4.4). It also confirms the assumption that the tachocline may be assumed to be in a steady state on a solar spin-down timescale.

3. One serious complication arises. Comparing the latitudinal variation of the angular velocity within the convection zone to the results of equations (3.60) and (3.59) suggests that the meridional flow must be upwelling in mid-latitudes, and downwelling both near the equator and the poles. Although the trapping of the magnetic field by the circulation can be assumed to be very efficient in downwelling regions, it is not the case in upwelling regions, and the magnetic field may be entrained into the convection zone where it must necessarily reconnect. Although no magnetic flux is lost through this process, so that the steady state assumption may still be valid *globally*, the system cannot locally be considered steady. In fact, it is likely to undergo a periodic or quasi-periodic behaviour with the gradual distortion of field lines followed regularly by reconnection. This phenomenon is discussed by Gough & McIntyre, who choose to neglect it in a first approximation. However, the scaling argument described

above is not valid in the upwelling region.

4. The scaling law does not apply in the equatorial and polar regions either. Indeed, in those cases the assumptions of neglecting the radial component of the velocity and the magnetic field do not apply. However, provided the flow in these regions does not influence the flow in the main body of the tachocline, the results described above still hold.

5. Finally, some of the most important issues about the dynamics of the tachocline could not be solved by the scaling arguments proposed by Gough & McIntyre. In particular, issues such as the prediction of the value of the angular velocity of the interior of the sun, the exact position and width of the upwelling region, the shape of the tachocline, etc ... could not be dealt with using such a simplified approach, since the geometrical information and latitudinal dependency of the system have been discarded.

3.3.3 Other magnetic models of the tachocline

Very few other papers have described attempts at modeling the tachocline. Amongst these are the work of McGregor & Charbonneau (1999), who (independently) reproduced the work of Rüdiger & Kitchatinov (1997), hereby confirming their results. More extensive is the work proposed by Hujeirat & Yorke (1998), who solve the problem of the nonlinear interaction of a large-scale magnetic field and fluid motions within a spherical shell with inner radius 0.6 $r_\odot$ and outer radius 0.85 $r_\odot$. However, their model is a poor representation of the true physics of the sun as they assume the background stratification and the motions to be adiabatic, and allow no heat diffusion. Yet the effects of stratification and heat diffusion are believed to be essential to the dynamics of the tachocline, according to Gough & McIntyre (1998).

Chapter 4

A numerical study of the solar tachocline

Previous MHD models of the tachocline failed to yield satisfying results, either because for need of a tractable model too stringent assumptions were made, or because for need of a physically realistic model, the mathematical problem could not be solved. An intermediate approach is now proposed whereby a model is created which encompasses gradually more realistic physics, and is solved numerically in order to obtain quantitative results which can be compared directly with observations. This model essentially tries to reproduce the observed interior rotation rate of the radiative zone by studying the full nonlinear interaction between a magnetic field and fluid motions in that region.

Several assumptions must be made; these assumptions need not be well justified, but are made with the sole aim of strongly reducing the mathematical difficulties of the problem studied. The principal assumption common to all the models is the axisymetry of the system. This assumption is essential to the solvability of the problem, but strongly reduces the degrees of freedom of the fluid motions. The second assumption is the steady state assumption, which states that the system must be able to find a dynamical equilibrium where all forces balance. This assumption is reasonably well justified provided all dynamical timescales are much shorter than either the stellar evolution timescale or the magnetic braking timescale, which is likely to be the case except maybe very deep in the interior (in that case, if the circulation operates on a local Eddington-Sweet timescale, it is much slower than the stellar evolution timescale, and has therefore no effect at all on the hydrostatic structure), where dynamical effects are

negligible anyway.

Once these fundamental assumptions have been laid out, some secondary ones must also be presented. These are either simplifying assumptions which are believed to have little effects on the fundamental dynamics of the system, but may have some non-negligible effects in changing the quantitative predictions of the model, or, these could be simplifying assumptions that do have a significant impact on the dynamics of the system but are made as a first approximation and will be removed in later models.

In this chapter and in Chapter 5, the very first attempt at such a numerical model is presented, which includes the two fundamental assumptions, as well as the assumption of incompressibility of the fluid, and combined with a constant hydrostatic background, which translates into constant density, viscosity and magnetic diffusivity. The model is described in the following section, and the mathematical equations are derived. The numerical method for the resolution of these equations is then presented.

4.1 MHD EQUATIONS FOR A TOY MODEL

If the fluid motions are assumed to be axisymmetric and incompressible, the MHD equations in a frame rotating with angular velocity $\boldsymbol{\Omega}_\mathrm{c}$ are the following:

$$\begin{aligned} 2\rho\boldsymbol{\Omega}_\mathrm{c}\times\boldsymbol{u}+\nabla p+\rho\boldsymbol{g}_\mathrm{h}-\boldsymbol{j}\times\boldsymbol{B}-\rho\nu\nabla^2\boldsymbol{u} &= 0\ , \\ \nabla\times(\boldsymbol{u}\times\boldsymbol{B})+\eta\nabla^2\boldsymbol{B} &= 0\ , \\ \nabla\cdot\boldsymbol{u} &= 0\ , \\ \nabla\cdot\boldsymbol{B} &= 0\ . \end{aligned} \qquad (4.1)$$

where the nonlinear terms in the meridional circulation $(\boldsymbol{u}\cdot\nabla)\boldsymbol{u}$ are neglected, and $\boldsymbol{g}_\mathrm{h}=g_\mathrm{h}\hat{\boldsymbol{e}}_r$ is the gravitational attraction of the hydrostatic background. The density $\rho=\rho_0=1\mathrm{g\ cm}^{-3}$ is assumed to be constant everywhere, as well as the viscosity ν and the magnetic diffusivity η. The angular velocity $\Omega_\mathrm{c}=2.84\times10^{-6}\ \mathrm{s}^{-1}$ is the ob-

served interior rotation rate of the sun. $\boldsymbol{B}$ is the magnetic field, $\boldsymbol{j}$ is the electric current, and $\boldsymbol{u}$ is the circulation which has components (u_r, u_θ, u_ϕ).
Using the following new system of units:

$$\begin{aligned} [r] &= r_{\rm c} \ , \\ [t] &= 1/\Omega_{\rm c} \ , \text{ so that } [u] = r_{\rm c}\Omega_{\rm c} \\ [B] &= B_0 \ , \end{aligned} \tag{4.2}$$

where B_0 is the typical strength of the radial field in the interior, the equations become:

$$2\hat{\boldsymbol{e}}_z \times \boldsymbol{u} = -\alpha\nabla p - \boldsymbol{g}_{\rm h} + \Lambda \boldsymbol{j} \times \boldsymbol{B} + E_\nu \nabla^2 \boldsymbol{u} \ , \tag{4.3}$$

$$\nabla\times(\boldsymbol{u} \times \boldsymbol{B}) = -E_\eta \nabla^2 \boldsymbol{B} \ , \tag{4.4}$$

with

$$\Lambda = \frac{\rho_0 B_0^2}{\Omega_{\rm c}^2 r_{\rm c}^2}, \ E_\nu = \frac{\nu}{\Omega_{\rm c} r_{\rm c}^2} \text{ and } E_\eta = \frac{\eta}{\Omega_{\rm c} r_{\rm c}^2} \ , \tag{4.5}$$

where all the quantities are now dimensionless and $\hat{\boldsymbol{e}}_z$ is the unit vector parallel to the rotation axis. The Ekman numbers E_ν and E_η represent the ratio of the diffusive timescale to the rotation timescale, and the Elsasser number Λ is the ratio of the typical amplitude of the Lorentz force to that of the Coriolis force.

These equations are solved in a region located between two spherical boundaries, with impermeable and no-slip walls so that the radial and the latitudinal components of the circulation vanish on the boundaries, and the azimuthal component of the circulation is given by the rotation of the boundaries. As a result, the angular velocity perturbation is $\tilde{\Omega} = \Omega_{\rm in} - \Omega_{\rm c}$ on the inner boundary, $\tilde{\Omega} = \Omega_{\rm cz}(\theta) - \Omega_{\rm c}$ on the outer boundary. The bounding spheres are assumed to be imperfectly conducting and it is assumed that the core interior to $r = r_{\rm in}$ rotates rigidly, which implies that the field outside the fluid region satisfies $\nabla^2 \boldsymbol{B} = 0$, with conditions that $\boldsymbol{B} \to 0$ at infinity, and to a purely poloidal dipolar structure as $r \to 0$. This uniquely determines the boundary conditions for the magnetic field. As a result of these con-

ditions, when the system is not rotating, the solution for the magnetic field is a purely poloidal dipolar structure.

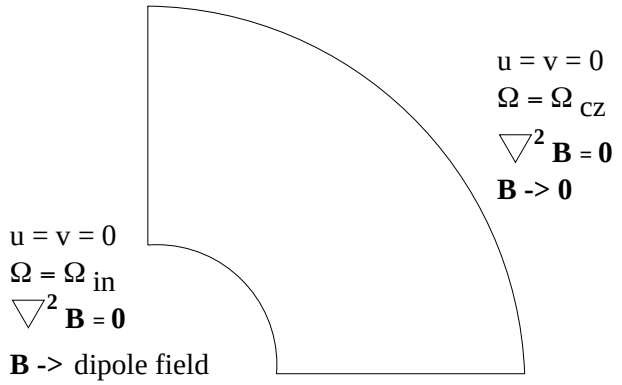

Figure 4.1: Boundary conditions.

The gap between the inner and outer boundaries is chosen to be $\delta = (r_c - r_{in})/r_c = 0.65$ in order to compare the results of the simulations with the work of Dormy, Cardin & Jault (1998), who solved a very similar set of equations with slightly different boundary conditions, in the same flow geometry. One of the main aims of this study is to be able to predict the angular velocity of the interior. In order to do so, the rotation rate of the inner core is treated as an eigenvalue of the problem and an additional boundary condition is imposed on the system accordingly, which is that no net torque should be applied to the inner core (this is a necessary condition to guarantee a steady state). This condition, which determines uniquely the value of Ω_{in}, is equivalent to requiring that the integral of the angular momentum flux through the boundary vanishes:

$$\int_0^{\pi/2} \left(\rho\nu r^2 \sin^2\theta \frac{\partial \Omega}{\partial r} + r \sin\theta B_r B_\phi \right) \sin\theta \mathrm{d}\theta = 0 \, . \qquad (4.6)$$

One can notice through this expression the main justification for the conducting boundary condition: in the insulating case, the radial component of the current must vanish on the boundaries, which in turn implies that the toroidal field must vanish. This, combined with the

impermeable boundary condition implies that the angular momentum flux through the boundaries is purely viscous. Since viscosity is normally negligible in the sun, this model would be a poor representation of the dynamical structure of the radiative zone.

The system as given by the previous equations and boundary conditions is a well posed system of partial differential equations with one eigenvalue. The numerical method chosen for the resolution of this system is first to write the system of equations with respect to a spherical polar coordinate system, to respect the symmetry of the problem, then an expansion of the latitudinal dependency of the equations onto Fourier modes, and finally the resolution of the resulting equations in the radial direction using a Newton-Raphson relaxation method.

4.2 Expansion of the MHD equations into spherical coordinates

All quantities are expressed in a spherical coordinate system (r, θ, ϕ) and have components $\boldsymbol{Q} = (Q_r, Q_\theta, Q_\phi)$ in this system. In order to avoid singularities near the poles, the following functions are introduced:

$$\begin{aligned} v &= \sqrt{1-\mu^2}u_\theta \ , \\ b &= \sqrt{1-\mu^2}B_\theta \ , \\ S &= r\sqrt{1-\mu^2}B_\phi \ , \\ L &= r\sqrt{1-\mu^2}u_\phi \ , \\ W &= r\sqrt{1-\mu^2}\omega_\phi = \frac{\partial}{\partial r}(rv) + (1-\mu^2)\frac{\partial u}{\partial \mu} \ , \\ J &= r\sqrt{1-\mu^2}j_\phi = \frac{\partial}{\partial r}(rb) + (1-\mu^2)\frac{\partial B}{\partial \mu} \ , \end{aligned} \tag{4.7}$$

where $\mu = \cos\theta$. The notation is simplified by taking $u \equiv u_r$ and $B \equiv B_r$.

Projecting the equations onto a spherical coordinate system and sub-

stituting the new variables into the system yields

$$\begin{aligned} & 2\mu v + 2(1-\mu^2)u + \Lambda\left(\frac{b}{r^2}\frac{\partial S}{\partial \mu} - \frac{B}{r}S'\right) \\ = \quad & \frac{E_\nu}{r}\left(L'' + \frac{1-\mu^2}{r^2}\frac{\partial^2 L}{\partial \mu^2}\right) \ , \end{aligned} \tag{4.8}$$

$$\begin{aligned} - \quad & 2\mu L' - 2\frac{1-\mu^2}{r}\frac{\partial L}{\partial \mu} \\ + \quad & \Lambda\left[\frac{2}{r}BJ + \frac{b}{r}\frac{\partial J}{\partial \mu} + \frac{2\mu}{1-\mu^2}\left(\frac{S}{r^2}S' + J\frac{b}{r}\right) - J'B\right] \\ = \quad & E_\nu\left(W'' + \frac{1-\mu^2}{r^2}\frac{\partial^2 W}{\partial \mu^2}\right) \ , \end{aligned} \tag{4.9}$$

$$ub - vB = E_\eta \frac{J}{r} \ , \tag{4.10}$$

$$\begin{aligned} & (L'B - uS') + \frac{2}{r}(uS - LB) \\ + \quad & \frac{1}{r}\left(v\frac{\partial S}{\partial \mu} - b\frac{\partial L}{\partial \mu}\right) + \frac{2\mu}{r(1-\mu^2)}(vS - Lb) \\ = \quad & -E_\eta\left(S'' + \frac{1-\mu^2}{r^2}\frac{\partial^2 S}{\partial \mu^2}\right) \ , \end{aligned} \tag{4.11}$$

$$ru' = \frac{\partial v}{\partial \mu} - 2u \ , \ rB' = \frac{\partial b}{\partial \mu} - 2B \ , \tag{4.12}$$

where the primes denote differentiation with respect to r. To complete the system, the definitions of the vorticity function W and of the electric current function J are needed

$$rv' = W - v - (1-\mu^2)\frac{\partial u}{\partial \mu} \ , \tag{4.13}$$

$$rb' = J - b - (1-\mu^2)\frac{\partial B}{\partial \mu} \ . \tag{4.14}$$

The periodicity of the system in the latitudinal coordinate θ suggests the expansion of the system onto Fourier modes. This is equivalent to an expansion of the equations in the coordinate μ onto Chebyshev polynomials, as $T_n(\cos\theta) = \cos n\theta$ where $T_n(\mu)$ is the Chebyshev polynomial of order n. The following expansion is chosen for each of the relevant quantities:

$$\begin{aligned}
u &= \sum_{n=1..N} Y_n \frac{\partial}{\partial \mu}\left((1-\mu^2)T_{2n-1}(\mu)\right) \ , \\
v &= (1-\mu^2)\sum_{n=1..N} Y_{N+n}(r)T_{2n-1}(\mu) \ , \\
W &= (1-\mu^2)\sum_{n=1..N} Y_{2N+n}(r)T_{2n-1}(\mu) \ , \\
W' &= (1-\mu^2)\sum_{n=1..N} Y_{3N+n}(r)T_{2n-1}(\mu) \ , \\
L &= (1-\mu^2)\sum_{n=1..N} Y_{4N+n}(r)T_{2n-2}(\mu) \ , \\
L' &= (1-\mu^2)\sum_{n=1..N} Y_{5N+n}(r)T_{2n-2}(\mu) \ , \\
B &= \sum_{n=1..N} Y_{6N+n}(r)T_{2n-1}(\mu) \ , \\
b &= (1-\mu^2)\sum_{n=1..N} Y_{7N+n}(r)T_{2n-2}(\mu) \ , \\
S &= (1-\mu^2)\sum_{n=1..N} Y_{8N+n}(r)T_{2n-1}(\mu) \ , \\
S' &= (1-\mu^2)\sum_{n=1..N} Y_{9N+n}(r)T_{2n-1}(\mu) \ , \\
J &= (1-\mu^2)\sum_{n=1..N} Y_{10N+n}(r)T_{2n-2}(\mu) \ . \qquad (4.15)
\end{aligned}$$

The advantage in defining u that way is to guarantee mass conservation, as

$$\int_0^\pi u_r \ \sin\theta \mathrm{d}\theta = \int_0^1 u \mathrm{d}\mu = 0 \ . \qquad (4.16)$$

The reason for the odd notation in equations 4.15 is to follow as closely as possible the notation used in the numerical code, to facilitate the comparison between the equations presented in this dissertation and the program. Expanding onto Chebyshev polynomial and projecting the resulting equations onto each Fourier mode yields the following system. The summation convention is used for index m, and the following notation means

$$(m-1)Y_{4N+m}Y_{6N+k-m+2} \equiv \sum_{m=1}^{N} a_{k-m+2}(m-1)Y_{4N+m}Y_{6N+k-m+2} \ , \tag{4.17}$$

where, for this equation, $a_j = 1$ if $1 \leq j \leq N$ and $a_j = 0$ otherwise.

The momentum equation:

$$\begin{aligned} \frac{E_\nu}{r}Y'_{5N+1} &= Y_{N+1} - Y_1 + \frac{\Lambda}{4r^2}\left[(2m-3)Y_{7N+m}Y_{8N+m}\right. \\ &- \left.(2m+1)Y_{7N+m+1}Y_{8N+m} - Y_{7N+1}Y_{8N+1}\right] \\ &- \frac{\Lambda}{2r}Y_{9N+m}Y_{6N+m} - \frac{E_\nu}{\pi r^3}Y_{4N+m}A_{0,2m-2} \ , \end{aligned} \tag{4.18}$$

and for $k = 1, .., N-1$,

$$\begin{aligned} &\frac{E_\nu}{r}Y'_{5N+k+1} = Y_{N+k} + Y_{N+k+1} + (2k-1)Y_{k+1} - (2k+1)Y_k \\ &+ \frac{\Lambda}{4r^2}\left[(2m-3)Y_{7N+k-m+2}Y_{8N+m} + (2m-3)Y_{7N+k+m}Y_{8N+m}\right. \\ &+ (2m-3)Y_{7N+m-k}Y_{8N+m} - (2m+1)Y_{7N+k-m+1}Y_{8N+m} \\ &- \left.(2m+1)Y_{7N+k+m+1}Y_{8N+m} - (2m+1)Y_{7N+m-k+1}Y_{8N+m}\right] \\ &- \frac{\Lambda}{2r}\left[Y_{9N+k-m+1}Y_{6N+m} + Y_{9N+k+m}Y_{6N+m} + Y_{9N+m-k}Y_{6N+m}\right] \\ &- \frac{2E_\nu}{\pi r^3}Y_{4N+m}A_{2k,2m-2} \ . \end{aligned} \tag{4.19}$$

The vorticity equation:

$$
\begin{aligned}
& E_\nu Y'_{3N+k} \\
& + \frac{\Lambda}{2}\left[Y'_{10N+m}Y_{6N+k-m+1} + Y'_{10N+m}Y_{6N+k+m-1} + Y'_{10N+m}Y_{6N+m-k}\right] \\
& = -\left[Y_{5N+k} + Y_{5N+k+1} + Y_{5N+1}\delta_{1,k}\right] \\
& - \frac{1}{r}\left[2(k-1)Y_{4N+k+1} - 2kY_{4N+k} - 2Y_{4N+1}\delta_{1,k}\right] \\
& + \frac{\Lambda}{r}\left[Y_{10N+m}Y_{6N+k-m+1} + Y_{10N+m}Y_{6N+k+m-1} + Y_{10N+m}Y_{6N+m-k}\right] \\
& + \frac{\Lambda}{2r}\left[(m-1)Y_{7N+k-m+2}Y_{10N+m} + (m-1)Y_{7N+k+m-1}Y_{10N+m}\right. \\
& + (m-1)Y_{7N+m-k}Y_{10N+m} - (m-1)Y_{7N+k-m+1}Y_{10N+m} \\
& \left. - (m-1)Y_{7N+m+k}Y_{10N+m} - (m-1)Y_{7N+m-k+1}Y_{10N+m}\right] \\
& + \frac{\Lambda}{2r^2}\left[Y_{8N+m}Y_{9N+k-m+1} + Y_{8N+m}Y_{9N+k-m} + Y_{8N+m}Y_{9N+k+m-1}\right. \\
& \left. + Y_{8N+m}Y_{9N+m-k} + Y_{8N+m}Y_{9N+k+m} + Y_{8N+m}Y_{9N+m-k+1}\right] \\
& + \frac{\Lambda}{2r^3}\left[(2m-3)Y_{8N+m}Y_{8N+k-m+1} + (2m-3)Y_{8N+m}Y_{8N+k+m-1}\right. \\
& + (2m-3)Y_{8N+m}Y_{8N+m-k} - (2m+1)Y_{8N+m}Y_{8N+k-m} \\
& \left. + (2m+1)Y_{8N+m}Y_{8N+k+m} + (2m+1)Y_{8N+m}Y_{8N+m-k+1}\right] \\
& - \frac{2E_\nu}{\pi r^2}Y_{2N+m}A_{2k-1,2m-1}\ , \qquad (4.20)
\end{aligned}
$$

for $k = 1, .., N$, where $\delta_{1,k}$ is the Kronecker symbol.

The integrated advection equation:

$$
\begin{aligned}
\frac{4E_\eta}{r}Y_{10N+1} &= (2m-3)Y_m Y_{7N+m} - (2m-1)Y_{m-1}Y_{7N+m} \\
&- 2Y_{N+m}Y_{6N+m} - Y_1 Y_{7N+1}\ , \qquad (4.21)
\end{aligned}
$$

and, for $k = 1, .., N-1$,

$$\begin{aligned}
\frac{4E_\eta}{r} Y_{10N+k+1} &= (2m-3) Y_{7N+k-m+2} Y_m + (2m-3) Y_{7N+k+m} Y_m \\
&+ (2m-3) Y_{7N+m-k} Y_m - (2m+1) Y_{7N+k-m+1} Y_m \\
&- (2m+1) Y_{7N+k+m+1} Y_m - (2m+1) Y_{7N+m-k+1} Y_m \\
&- 2 Y_{N+k-m+1} Y_{6N+m} - 2 Y_{N+k+m} Y_{6N+m} \\
&- 2 Y_{N+m-k} Y_{2N+m} \ . \qquad (4.22)
\end{aligned}$$

The advection equation:

$$\begin{aligned}
& - E_\eta Y'_{9N+k} \\
=& \frac{1}{2} \left[Y_{5N+m} Y_{6N+k-m+1} + Y_{5N+m} Y_{6N+k+m-1} + Y_{5N+m} Y_{6N+m-k} \right] \\
-& \frac{1}{r} \left[Y_{4N+m} Y_{6N+k-m+1} + Y_{4N+m} Y_{6N+k+m-1} + Y_{4N+m} Y_{6N+m-k} \right] \\
-& \frac{1}{4} \left[(2m-3) Y_m Y_{9N+k-m+1} + (2m-3) Y_m Y_{9N+m-k} \right. \\
&+ (2m-3) Y_m Y_{9N+k+m-1} - (2m+1) Y_m Y_{9N+k-m} \\
&\left. - (2m+1) Y_m Y_{9N+k+m} - (2m+1) Y_m Y_{9N+m-k+1} \right] \\
&+ \frac{1}{2r} \left[(2m-3) Y_m Y_{8N+k-m+1} + (2m-3) Y_m Y_{8N+m-k} \right. \\
&+ (2m-3) Y_m Y_{8N+k+m-1} - (2m+1) Y_m Y_{8N+k-m} \\
&\left. - (2m+1) Y_m Y_{8N+k+m} - (2m+1) Y_m Y_{8N+m-k+1} \right] \\
&+ \frac{1}{4r} \left[(2m-1) Y_{N+k-m+1} Y_{8N+m} + (2m-1) Y_{N+k+m-1} Y_{8N+m} \right. \\
&+ (2m-1) Y_{N+m-k} Y_{8N+m} - (2m-1) Y_{N+k-m} Y_{8N+m} \\
&\left. - (2m-1) Y_{N+m+k} Y_{8N+m} - (2m-1) Y_{N+m-k+1} Y_{8N+m} \right] \\
&- \frac{1}{2r} \left[(m-1) Y_{7N+k-m+2} Y_{4N+m} + (m-1) Y_{7N+k+m-1} Y_{4N+m} \right. \\
&+ (m-1) Y_{7N+m-k} Y_{4N+m} - (m-1) Y_{7N+k-m+1} Y_{4N+m} \\
&\left. - (m-1) Y_{7N+m+k} Y_{4N+m} - (m-1) Y_{7N+m-k+1} Y_{4N+m} \right] \\
&+ \frac{2E_\eta}{\pi r^2} Y_{8N+m} A_{2k-1,2m-1} \ , \qquad (4.23)
\end{aligned}$$

for $k = 1, .., N$.

Additional equations:

- The $\nabla \cdot \boldsymbol{u} = 0$ equation:

$$rY'_k = Y_{N+k} - 2Y_k \ , \tag{4.24}$$

  for $k = 1, .., N$.

- The $\nabla \cdot \boldsymbol{B} = 0$ equation:

$$rY'_{6N+k} = (k-1)Y_{7N+k+1} - kY_{7N+k} - Y_{7N+1}\delta_{1,k} - 2Y_{6N+k} \ , \tag{4.25}$$

  for $k = 1, .., N$.

- The relation between vorticity and velocity:

$$rY'_{N+k} = Y_{2N+k} - Y_{N+k} - \frac{2}{\pi} Y_m A_{2k-1,2m-1} \ , \tag{4.26}$$

  for $k = 1, .., N$.

- The relation between current and magnetic field:

$$rY'_{7N+1} = Y_{10N+1} - Y_{7N+1} - \frac{1}{\pi} Y_{6N+m} B_{0,2m-1} \ , \tag{4.27}$$

  and

$$rY'_{7N+k+1} = Y_{10N+k+1} - Y_{7N+k+1} - \frac{2}{\pi} Y_{6N+m} B_{2k,2m-1} \ , \tag{4.28}$$

  for $k = 1, .., N-1$, where $B_{k,n}$ is defined in the Appendix B.

- The relation between functions and their derivatives:

$$\begin{aligned} Y'_{2N+k} &= Y_{3N+k} \ , \\ Y'_{4N+k} &= Y_{5N+k} \ , \\ Y'_{8N+k} &= Y_{9N+k} \ , \end{aligned} \tag{4.29}$$

for $k = 1, .., N$.

4.3 Boundary conditions

The system has 11N equations with one eigenvalue, so 11N+1 boundary conditions are needed. The problem is limited to the solution of the flow between two concentric spheres, the larger one corresponding to the bottom of the convection zone.

4.3.1 Impermeable, no-slip walls

The condition on the meridional circulation can be rewritten simply as $u = 0$, $v = 0$, so that

- at the inner boundary:

$$Y_k(r_{\rm in}) = 0 \text{ and } Y_{N+k}(r_{\rm in}) = 0 \ , \tag{4.30}$$

  for $k = 1, .., N$,

- at the outer boundary

$$Y_k(r_{\rm out}) = 0 \text{ and } Y_{N+k}(r_{\rm out}) = 0 \ , \tag{4.31}$$

  for $k = 1, .., N$.

The no-slip condition implies that the angular velocity of the fluid on the boundary is equal to that of the boundary. The inner boundary rotates with uniform angular velocity $\Omega_{\rm in}$ which implies that

$$L(r_{\rm in}, \mu) = r_{\rm in}^2(1 - \mu^2)(\Omega_{\rm in} - \Omega_{\rm c}) \ , \tag{4.32}$$

so that

$$\begin{aligned} Y_{4N+1}(r_{\rm in}) &= r_{\rm in}^2(\Omega_{\rm in} - \Omega_{\rm c}) \ , \\ Y_{4N+k}(r_{\rm in}) &= 0 \text{ for } k = 2..N. \end{aligned} \tag{4.33}$$

The outer boundary rotates with the shear imposed by the convection zone so that

$$L(r_{\rm out},\mu) = r_{\rm out}^2(1-\mu^2)(\Omega_{\rm cz}(\mu)-\Omega_{\rm c}) \ , \tag{4.34}$$

where

$$\Omega_{\rm cz}(\mu) = \Omega_{\rm eq}(1-a_2\mu^2-a_4\mu^4) \ , \tag{4.35}$$

where $\Omega_{\rm eq} = 1.07\Omega_{\rm c}$, so that

$$\begin{aligned} Y_{4N+1}(r_{\rm out}) &= r_{\rm out}^2\left[(\Omega_{\rm eq}-\Omega_{\rm c}) - \Omega_{\rm eq}\left(\frac{a_2}{2}+\frac{3a_4}{8}\right)\right] \ , \\ Y_{4N+2}(r_{\rm out}) &= -\Omega_{\rm eq} r_{\rm out}^2\left(\frac{a_2+a_4}{2}\right) \ , \\ Y_{4N+3}(r_{\rm out}) &= -\Omega_{\rm eq} r_{\rm out}^2\frac{a_4}{8} \ , \\ Y_{4N+k} &= 0 \text{ for } k = 4..N. \end{aligned} \tag{4.36}$$

4.3.2 No torque condition for the bottom boundary

This condition, which determines uniquely the value of $\Omega_{\rm in}$, is equivalent to requiring that the integral of the angular momentum flux through the boundary vanishes:

$$\int_0^{\pi/2}\left(\rho\nu r^2\,\sin^2\theta\frac{\partial\Omega}{\partial r} + r\,\sin\theta B_r B_\phi\right)\,\sin\theta{\rm d}\theta = 0 \ . \tag{4.37}$$

This can be rewritten as

$$\int_{-1}^{1} E_\nu\left(\frac{\partial L}{\partial r}-\frac{2L}{r}\right)+\Lambda S B{\rm d}\mu = 0 \ . \tag{4.38}$$

Integrating this expression yields

$$E_\nu \left(\sum_{m=1}^{N} Y_{5N+m}(r_{\rm in})\gamma_{2m-2} - \frac{2}{r_{\rm in}} \sum_{m=1}^{N} Y_{4N+m}(r_{\rm in})\gamma_{2m-2} \right) \tag{4.39}$$

$$+\frac{\Lambda}{2} \sum_{m,n=1}^{N} Y_{8N+n}(r_{\rm in}) Y_{6N+m}(r_{\rm in})(\gamma_{2n+2m-2} + \gamma_{2n-2m}) = 0 \ ,$$

where γ_m is defined in Appendix B.

4.3.3 Magnetic field boundary conditions at the bottom boundary

The inner core is conducting, which implies that the magnetic field satisfies

$$\nabla^2 \boldsymbol{B} = \boldsymbol{0} \ , \tag{4.40}$$

(assuming the conductivity is uniform) everywhere within the core. This solution is matched it to a point source as $r \to 0$. In order to simplify the matching condition with the fluid region, it is assumed that the conductivity of the inner core is the same as that of the fluid region.

Equation (4.40) is first expanded in the spherical coordinate system as

$$\begin{aligned} \nabla^2 \left(\frac{\chi}{r \ \sin\theta} \hat{\boldsymbol{e}}_\phi \right) &= 0 \ , \\ \nabla^2 \left(B_\phi \hat{\boldsymbol{e}}_\phi \right) &= 0 \ , \end{aligned} \tag{4.41}$$

when the poloidal flux function χ is defined as

$$\boldsymbol{B}_{\rm p} = \nabla \times \left(\frac{\chi}{r \ \sin\theta} \hat{\boldsymbol{e}}_\phi \right) \ . \tag{4.42}$$

The set of solutions to equations (4.41) that tend to a purely dipolar structure as $r \to 0$ are

$$\begin{aligned} S &= -(1-\mu^2)\sum_{n=1}^{\infty}\alpha_n r^{2n+1}\frac{\mathrm{d}P_{2n}}{\mathrm{d}\mu} \ , \\ \chi &= -\frac{\chi_0}{r}(1-\mu^2) - (1-\mu^2)\sum_{n=1}^{\infty}\beta_n r^{2n}\frac{\mathrm{d}P_{2n-1}}{\mathrm{d}\mu} \ , \end{aligned} \tag{4.43}$$

where $P_n(\mu)$ is the Legendre Polynomial of order n. Using the fact that

$$B = \frac{1}{r^2}\frac{\partial\chi}{\partial\mu} \ , \ b = \frac{1}{r}\frac{\partial\chi}{\partial r} \ , \tag{4.44}$$

and matching the solutions (4.43) with the numerical solutions in the fluid region at the bottom boundary yields

$$\begin{aligned} &\sum_{n=1}^{\infty} Y_{6N+n}(r_{\mathrm{in}})T_{2n-1}(\mu) \\ =&\frac{2\chi_0}{r_{\mathrm{in}}^3}P_1(\mu) + \sum_{n=1}^{\infty}\beta_n r_{\mathrm{in}}^{2n-2}(2n-1)(2n)P_{2n-1}(\mu) \ , \end{aligned} \tag{4.45}$$

$$\begin{aligned} &(1-\mu^2)\sum_{n=1}^{\infty} Y_{7N+n}(r_{\mathrm{in}})T_{2n-2} \\ =&-\frac{\chi_0}{r_{\mathrm{in}}^3}(1-\mu^2)\frac{\mathrm{d}P_1}{\mathrm{d}\mu} - 2n(1-\mu^2)\sum_{n=1}^{\infty}\beta_n r_{\mathrm{in}}^{2n-2}\frac{\mathrm{d}P_{2n-1}}{\mathrm{d}\mu} \ . \end{aligned} \tag{4.46}$$

Using the identity

$$\left((1-\mu^2)P_n'\right)' + n(n+1)P_n = 0 \ , \tag{4.47}$$

and integrating equations (4.45) and (4.46) onto the basis formed by the Legendre polynomials results in

$$\begin{aligned}&\frac{2\chi_0}{r_{\rm in}^3}h_1\delta_{1,k}+\beta_k r_{\rm in}^{2k-2}(2k-1)(2k)h_{2k-1}\\ =&Y_{6N+n}(r_{\rm in})I_{2k-1,2n-1}\ ,\end{aligned}\tag{4.48}$$

$$\begin{aligned}&2B_0\delta_{1,k}+(2k)^2(2k-1)\beta_k r_{\rm in}^{2k-2}h_{2k-1}\\ =&Y_{7N+n}(r_{\rm in})D_{2k-1,2n-2}\ ,\end{aligned}\tag{4.49}$$

for $k=1,..,N$, where $h_k=2/(2k+1)$ (see Abramowitz & Stegun, 1972), and $I_{k,n}$ and $D_{k,n}$ are defined in Appendix B; also,

$$B_0=\frac{2\chi_0}{r_{\rm in}^3}\ .\tag{4.50}$$

The summation convention is used for the index n, with n ranging from 1 to N. Eliminating the coefficients β_k yields,

$$\begin{aligned}Y_{7N+n}(r_{\rm in})D_{1,2n-2}&=2Y_{6N+n}(r_{\rm in})I_{1,2n-1}-2B_0\ ,\\ Y_{7N+n}(r_{\rm in})D_{2k-1,2n-2}&=2kY_{6N+n}(r_{\rm in})I_{2k-1,2n-1}\ ,\end{aligned}\tag{4.51}$$

for $k=2,..,N$.

For the toroidal field, the same method yields successively

$$\begin{aligned}Y_{8N+n}(r_{\rm in})T_{2n-1}&=-\alpha_n r_{\rm in}^{2n+1}\frac{{\rm d}P_{2n}}{{\rm d}\mu}\ ,\\ Y_{9N+n}(r_{\rm in})T_{2n-1}&=-(2n+1)\alpha_n r_{\rm in}^{2n}\frac{{\rm d}P_{2n}}{{\rm d}\mu}\ ,\end{aligned}\tag{4.52}$$

so that

$$\begin{aligned}Y_{8N+n}(r_{\rm in})D_{2k,2n-1}&=2k(2k+1)\alpha_k r_{\rm in}^{2k+1}h_{2k}\ ,\\ Y_{9N+n}(r_{\rm in})D_{2k,2n-1}&=2k(2k+1)^2\alpha_k r_{\rm in}^{2k}h_{2k}\ ,\end{aligned}\tag{4.53}$$

for $k = 1, .., N$ and, eliminating the α_k coefficients

$$(2k+1)Y_{8N+n}(r_{\rm in})D_{2k,2n-1} = r_{\rm in}Y_{9N+n}(r_{\rm in})D_{2k,2n-1} \ , \quad (4.54)$$

for $k = 1, .., N$.

4.3.4 Magnetic field at the top: the vacuum condition

The same method is used to obtain the matching conditions at the top boundary. For the toroidal field,

$$2kY_{8N+n}(r_{\rm out})D_{2k,2n-1} + r_{\rm out}Y_{9N+n}(r_{\rm out})D_{2k,2n-1} = 0 \ , \quad (4.55)$$

for all $k = 1..N$, where $I_{k,n}$ and $D_{k,n}$ are defined in Appendix B. Again, the summation convention is used for index n with n ranging from 1 to N. The boundary condition for the poloidal field is

$$(2k-1)Y_{6N+n}(r_{\rm out})I_{2k-1,2n-1} + Y_{7N+n}(r_{\rm out})D_{2k-1,2n-2} = 0 \ , \quad (4.56)$$

for $k = 1, .., N$.

4.3.5 Algebraic condition

Finally, for consistency, the algebraic equations 4.21 and 4.22 must also be reproduced at one of the boundaries. The inner boundary is chosen in order to increase the performance of the numerical method used for the resolution of the radial ODEs.

4.4 Numerical resolution of radial ODEs

The resulting system, after spectral expansion of the MHD equations and boundary conditions, is a system of 10N ODEs and N algebraic equations in the independent variable r, varying

between $r_{\rm in}$ and $r_{\rm out}$. This system is solved with the Newton-Raphson-Kantorovich (NRK) algorithm developed and implemented by D. O. Gough. The NRK program has been slightly modified in order to be capable of solving algebraic equations simultaneously with the differential equations. The notations introduced in the two following sections are specific to those sections and are not used otherwise in this dissertation.

4.4.1 Brief overview of NRK

The NRK algorithm solves the system of equations

$$\frac{\mathrm{d}y_i}{\mathrm{d}x} = f_i(\boldsymbol{y}, \boldsymbol{\Lambda}, x) \ , \tag{4.57}$$

where x is the independent variable, $\boldsymbol{y} = (y_1, y_2, ...y_I)$ is the set of dependent variables, and $\boldsymbol{\Lambda} = (\lambda_1, \lambda_2, ...\lambda_K)$ is the set of eigenvalues of the problem.

This system is discretized upon a mesh $(x_1, x_2, ...x_N)$, with

$$y_i^{n+1} - y_i^n = \frac{\Delta x^n}{2} \left[f_i(\boldsymbol{y}^n, \boldsymbol{\Lambda}, x^n) + f_i(\boldsymbol{y}^{n+1}, \boldsymbol{\Lambda}, x^{n+1}) \right] \ , \tag{4.58}$$

for $n = 1, .., N$ and

$$\Delta x^n = x^{n+1} - x^n \ . \tag{4.59}$$

The mesh is chosen to follow adequately the variations of the solutions. This point is discussed in more detail in Section 4.4.3

Given a trial value for the solution $\overline{\boldsymbol{y}}$ and $\overline{\boldsymbol{\Lambda}}$, the true solution is $\boldsymbol{y} = \overline{\boldsymbol{y}} + \delta\boldsymbol{y}$ and $\boldsymbol{\Lambda} = \overline{\boldsymbol{\Lambda}} + \delta\boldsymbol{\Lambda}$ for each component of index i and at each point of index n. To first order in δ, the errors $\delta\boldsymbol{y}$ and $\delta\boldsymbol{\Lambda}$ satisfy

$$\delta y_i^{n+1} - \delta y_i^n - \frac{\Delta x^n}{2} \left[F_{ij}^n \delta y_j^n + F_{ij}^{n+1} \delta y_j^{n+1} + \left(L_{ik}^n + L_{ik}^{n+1} \right) \delta\lambda_k \right]$$

$$+\overline{y}_i^{n+1} - \overline{y}_i^n - \frac{\Delta x^n}{2}\left(\overline{f}_i^{n+1} + \overline{f}_i^n\right) = 0 \ , \tag{4.61}$$

where

$$F_{ij}^n = \frac{\partial f_i^n}{\partial y_j} \ , \tag{4.62}$$

$$L_{ik}^n = \frac{\partial f_i^n}{\partial \lambda_k} \ , \tag{4.63}$$

and the summation convention is used for subscripts, but not for superscripts. To put it in a more concise form,

$$A_{ij}^n \delta y_j^n + B_{ij}^n \delta y_j^{n+1} + C_{ik}^n \delta\lambda_k + D_i^n = 0 \ , \tag{4.64}$$

where

$$\begin{aligned} A_{ij}^n =& \delta_{ij} + \frac{\Delta x^n}{2} F_{ij}^n \ , \\ B_{ij}^n =& -\delta_{ij} + \frac{\Delta x^n}{2} F_{ij}^{n+1} \ , \\ C_{ik}^n =& \frac{\Delta x^n}{2}\left(L_{ik}^n + L_{ik}^{n+1}\right) \ , \\ D_i^n =& \frac{\Delta x^n}{2}\left(\overline{f}_i^n + \overline{f}_i^{n+1}\right) - \left(\overline{y}_i^{n+1} - \overline{y}_i^n\right) \ , \end{aligned} \tag{4.65}$$

for $n = 1, .., N$.

This system is solved for the matrix composed of all δ_i^n. The solution to the system is then given by $\overline{\boldsymbol{y}} + \delta\boldsymbol{y}$, and this solution is used as a guess for the next iteration of the NRK algorithm until the error $\delta\boldsymbol{y}$ is satisfyingly small.

The NRK algorithm described in the previous section is modified in order to be capable of solving systems of the type

$$\sum_{j=1}^{I} M_{ij}(\boldsymbol{y}, \boldsymbol{\Lambda}, x)\frac{\mathrm{d}y_i}{\mathrm{d}x} = f_i(\boldsymbol{y}, \boldsymbol{\Lambda}, x) \ . \tag{4.66}$$

In the case of algebraic equations, the matrix M_{ij} is null. It can be shown that this type of system can always be reduced to the type described in the previous section, but it may occur that such a reduction leads to very complicated expressions for the right-hand-side of the equations, which is the case with the MHD equations studied in this work. It is then much easier to use the modified version of NRK presented here.

The discretization of equation 4.66 yields

$$\sum_{j=1}^{I} \left(M_{ij}^{n+1} + M_{ij}^{n}\right)\left(y_{ij}^{n+1} - y_{ij}^{n}\right) = \Delta x^n \left(f_i^{n+1} + f_i^{n}\right) \ , \tag{4.67}$$

where the same notation is used as in the previous section. Then, using the same method, the system is successively reduced to

$$\begin{aligned}
&\sum_{j=1}^{I}\left[M_{ij}^{n+1} + \sum_{l=1}^{I}\delta y_l^{n+1}T_{ijl}^{n+1} + \sum_{k=1}^{K}\delta\lambda_k^{n+1}U_{ijk}^{n+1} + M_{ij}^{n}\right.\\
&\left. + \sum_{l=1}^{I}\delta y_l^{n}T_{ijl}^{n} + \sum_{k=1}^{K}\delta\lambda_k^{n}U_{ijk}^{n}\right]\cdot\left[\overline{y}_j^{n+1} + \delta y_j^{n+1} - \overline{y}_j^{n} - \delta y_j^{n}\right]\\
&=\Delta x^n\left[f_i^{n+1} + \sum_{l=1}^{I}\delta y_l^{n+1}F_{il}^{n+1} + \sum_{k=1}^{K}\delta\lambda_k^{n+1}L_{ik}^{n+1}\right.\\
&\left. + f_i^{n} + \sum_{l=1}^{I}\delta y_l^{n}F_{il}^{n} + \sum_{k=1}^{K}\delta\lambda_k^{n}L_{ik}^{n}\right] \ ,
\end{aligned} \tag{4.68}$$

where

$$T^n_{ijl} = \frac{\partial M^n_{ij}}{\partial y_l} \ , \tag{4.69}$$

$$U^n_{ijk} = \frac{\partial M^n_{ij}}{\partial \lambda_k} \ . \tag{4.70}$$

To first order in δ, and introducing the variable

$$\delta \overline{y}^n_i = \overline{y}^{n+1}_i - \overline{y}^n_i \ , \tag{4.71}$$

it is easy to show that the error matrix δy^n_i satisfies

$$A^n_{ij} \delta y^n_j + B^n_{ij} \delta y^{n+1}_j + C^n_{ik} \delta \lambda_k + D^n_i = 0 \ , \tag{4.72}$$

where

$$\begin{aligned}
A^n_{ij} &= M^{n+1}_{ij} + M^n_{ij} + \Delta x^n F^n_{ij} - \sum_{l=1}^{I} \delta \overline{y}^n_l T^n_{ilj} \ , \\
B^n_{ij} &= -\left(M^{n+1}_{ij} + M^n_{ij} \right) + \Delta x^n F^{n+1}_{ij} - \sum_{l=1}^{I} \delta \overline{y}^n_l T^{n+1}_{ilj} \ , \\
C^n_{ik} &= \Delta x^n \left(L^n_{ik} + L^{n+1}_{ik} \right) - \sum_{j=1}^{I} \delta \overline{y}^n_j \left(U^{n+1}_{ijk} + U^{n+1}_{ijk} \right) \ , \\
D^n_i &= \Delta x^n \left(\overline{f}^n_i + \overline{f}^{n+1}_i \right) - \sum_{j=1}^{I} \delta \overline{y}^n_j \left(M^{n+1}_{ij} + M^n_{ij} \right) \ ,
\end{aligned} \tag{4.73}$$

for $n = 1, .., N$. Apart from the additional terms in these four matrices, the NRK algorithm remains otherwise unchanged.

4.4.3 Choice of the mesh spacing

As in all numerical algorithms for solving ODE's, it is important to discretize the independent variable in such as way as to follow closely the variations of the solution, by choosing to have more mesh points in regions where the function varies more rapidly.

In most problems where the solution is not known a priori the most judicious way of performing this task is through automated mesh-point allocation, as it is proposed for example by Gough, Spiegel & Toomre (1974).

This algorithm was initially used in the resolution of the equations presented in Section 4.2, but it was found that it had a rather low performance for very thin boundary layers (of order of $10^{-6}(r_{\rm out} - r_{\rm in})$ or less). This low performance is probably due to the fact that as many modes are used, the allocation algorithm cannot choose adequately according to which functions the mesh should be stretched.

The alternative solution is to stretch the mesh manually. In order to do this, the position and width of the boundary layers must first be determined. The principal boundary layers, as it will be shown in the following chapter, are located at both spherical boundaries. It will also be shown that the typical width of the thinnest boundary layer on the spheres is

- in the non-magnetic case:

$$\delta = E_\nu^{1/2} \mu^{-1/2} \ , \tag{4.74}$$

- in the magnetic case:

$$\delta = \left(\frac{\Lambda_{\rm loc} + \sqrt{\Lambda_{\rm loc}^2 + 4\mu^2 E_\eta^2}}{2 E_\nu E_\eta} \right)^{-1/2} \ , \tag{4.75}$$

where $\Lambda_{\rm loc}$ is the local Elsasser number defined as

$$\begin{aligned} \Lambda_{\rm loc} &= \Lambda \text{ on the inner boundary,} \\ \Lambda_{\rm loc} &= r_{\rm in}^6 \Lambda \text{ on the outer boundary.} \end{aligned} \tag{4.76}$$

The width of the boundary layer varies significantly with latitude. It is important to resolve the smallest possible scale, so

that the "assumed" boundary layer thickness for the numerical calculations will be that corresponding to $\mu = 1$.

In order to follow correctly the development of the boundary layers, a minimum of ten points is taken within the width δ near the boundary, and the same mesh-point density is kept for ten times this width, leading to a total of a hundred points in each of the boundary layers. Typically, another 400 points are allocated to the interval outside the boundary layers. The principal advantage of NRK over other numerical methods is that the mesh spacing need not be smoothly varying, but can have corners. This allows the choice of a very simple mesh-point allocation, as follows: if $N_{\rm bulk}$ is the number of mesh points allocated to the interval outside of the boundary layers,

$$\begin{aligned} x_n &= r_{\rm in} + \frac{n-1}{10}\delta \text{ for } n = 1, 100 \qquad (4.77) \\ x_n &= r_{\rm in} + 10\delta + \frac{r_{\rm out} - r_{\rm in} - 20\delta}{N_{\rm bulk}}(n - 101) \\ &\text{for} \quad n = 101, 100 + N_{\rm bulk} \\ x_n &= r_{\rm out} - 10\delta + \frac{n - 101 - N_{\rm bulk}}{9.9}\delta \\ &\text{for} \quad n = 101 + N_{\rm bulk}, 200 + N_{\rm bulk} \end{aligned}$$

A typical mesh distribution is shown in Fig. 4.2 for a non-magnetic simulation with Ekman number $E_\nu = 10^{-6}$, and a magnetic simulation with Ekman numbers $E_\nu = E_\eta = 10^{-4}$.

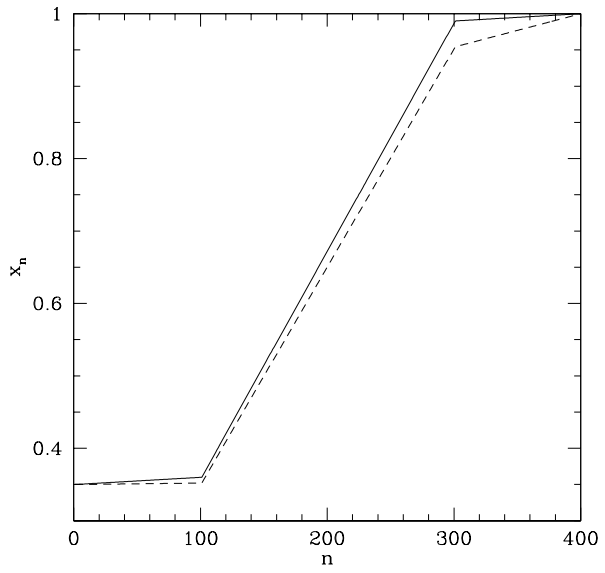

Figure 4.2: Mesh spacing for non-magnetic simulation, for Ekman number $E_\nu = 10^{-6}$ (solid line) and for a magnetic simulation with Ekman numbers $E_\nu = E_\eta = 10^{-4}$ and $\Lambda = 1/200$.

Chapter 5

Discussion of the results

The model proposed in the previous chapter is investigated numerically, and various issues are considered. In order to verify the good behaviour of the numerical analysis, and test the performance of the program, the non-magnetic case is studied first in Section 5.1. This corresponds to the study of a viscous fluid flow between concentric rotating spheres, which is a problem that can be studied analytically in the limit of very small viscosity. The numerical results are compared with the analytical predictions, as well as with another similar numerical study performed by Dormy, Cardin & Jault (1998). The results in the magnetic case are presented in Section 5.2. The problem depends essentially on three parameters: the Ekman numbers E_ν and E_η, which represent the ratio of the diffusive timescale to the rotation timescale, and the Elsasser number, which is the ratio of the typical amplitude of the Lorentz force to that of the centrifugal force. An analytical boundary layer analysis of the regions near the poles and near the equator is presented in Section 5.3 and compared with the simulations. The results from the simulations are compared with other models of the tachocline and with the observations.

5.1 Non-magnetic case

5.1.1 Numerical results

When no magnetic field is present, fluid motion is dominated by Coriolis forces everywhere except in two boundary layers near

the spherical boundaries, and in a shear layer at the tangent cylinder. In the bulk of the fluid, angular velocity is more-or-less constant on cylinders: indeed, when viscosity is negligible, the fluid dynamics equations for the incompressible fluid reduce to

$$(\Omega_c \times \boldsymbol{u})_\phi = 0 \ , \tag{5.1}$$

which implies that $\boldsymbol{u}$ must be parallel to the rotation axis, and

$$(\nabla \times (\Omega_c \times \boldsymbol{u}))_\phi \ , \tag{5.2}$$

which implies that the angular velocity must be independent of z where z is the cylindrical coordinate that runs parallel to the rotation axis. Viscous effects are necessary in the boundary layers to ensure the smooth transition between the rotation profile in the bulk of the fluid and that imposed at the boundaries. This structure was first studied by Proudman (1956) and Stewartson (1966), in the case where E_ν is asymptotically small. It is possible to show that in this limit the interior angular velocity is uniquely determined by the size of the gap between the two spheres, and its value can be predicted analytically. The derivation of the relation between the interior angular velocity and the gap width in the asymptotic case is carried out in the following section.

5.1.2 Asymptotic analysis of a fluid flow between concentric rotating spheres

5.1.2.1 The model

The model is represented in Fig. 5.2. The top boundary at $r = r_{\rm out} = r_c$ undergoes the latitudinal shear observed at the base of the convection zone $\Omega_{\rm cz}(\theta)$, given by equation (2.14), with the parameters $a_2 = 0.15$ and $a_4 = 0.15$; the bottom boundary at $r = r_{\rm in}$ is rotating rigidly with angular velocity Ω_c. The flow is assumed to be incompressible, which suggests the use of the

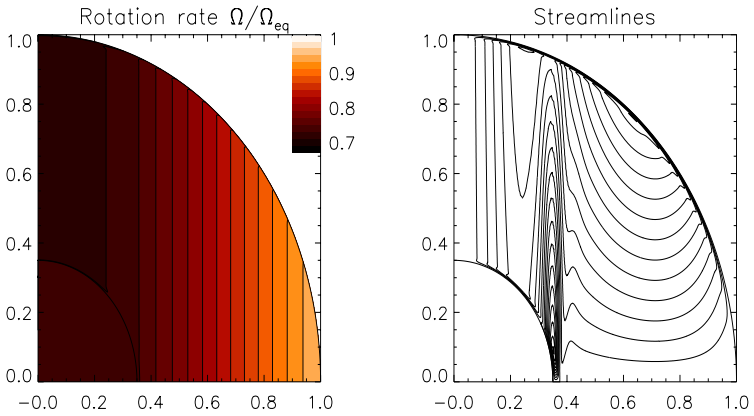

Figure 5.1: Rotation profile and streamlines in the non-magnetic case for $E_\nu = 8 \times 10^{-6}$. The interior rotation rate in this simulation is $\Omega_{\rm in} = 0.75\Omega_{\rm eq}$.

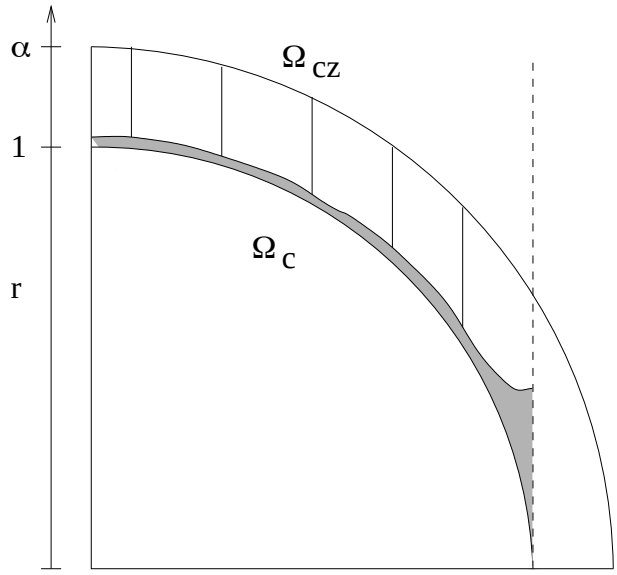

Figure 5.2: Schematic representation of the model implemented in Section 5.1.2. The edge of the convection zone, at the dimensionless radius $r = 1$, is rotating with angular velocity $\Omega_{\rm cz}(\theta)$; the edge of the radiative zone (at the dimensionless radius $r = 1 - \Delta$) is rotating with constant velocity $\Omega_{\rm c}$. The boundary with the radiative zone is impermeable. Outside the boundary layer, the flow as well as the contours of constant angular velocity are parallel to the rotation axis. The dotted line represents the edge of the cylinder with unit radius, outside which the flow cannot reach the radiative zone: there can be no dynamical connection of the convection zone to the radiative zone outside this cylinder.

stream function ψ, defined by

$$u_r = \frac{1}{r^2 \sin\theta}\frac{\partial \psi}{\partial \theta} \text{ and } u_\theta = -\frac{1}{r \sin\theta}\frac{\partial \psi}{\partial r} \ . \tag{5.3}$$

The specific angular momentum is introduced as

$$u_\phi = \frac{\chi}{r \sin\theta} \ , \tag{5.4}$$

Two coordinate systems will be used: the spherical coordinate system (r, θ, ϕ), with the unit vectors $(\hat{\boldsymbol{e}}_r, \hat{\boldsymbol{e}}_\theta, \hat{\boldsymbol{e}}_\phi)$ and the cylindrical coordinate system (s, φ, z), with the vertical axis aligned with the rotation axis; the unit vector in the vertical direction is $\hat{\boldsymbol{e}}_z$. In order to find an approximate analytical solution, it is necessary to linearize the equations; in order to do so, the meridional flow is assumed to be slow, so that the nonlinear advection term $(\boldsymbol{u}\cdot\nabla)\boldsymbol{u}$ in the momentum equation can be neglected. This approximation can be shown to be valid provided the angular velocity imposed by the top boundary is not very different from the angular velocity of the bottom boundary, which is roughly true in the case of the solar tachocline (the average difference in angular velocities between the convection zone and the interior is of order of 10 %).

Within these approximations, the system is described by the following equations (which are the angular momentum equation and the thermal wind equation respectively):

$$\begin{aligned} 2\left(\frac{\partial \chi}{\partial r}\cos\theta - \frac{1}{r}\frac{\partial \chi}{\partial \theta}\sin\theta\right) &= E_\nu D^4 \psi \ , \\ -2\left(\frac{\partial \psi}{\partial r}\cos\theta - \frac{1}{r}\frac{\partial \psi}{\partial \theta}\sin\theta\right) &= E_\nu D^2 \chi \ , \end{aligned} \tag{5.5}$$

where

$$D^2 = \frac{\partial^2}{\partial r^2} + \frac{\sin\theta}{r^2}\frac{\partial}{\partial \theta}\left(\frac{1}{\sin\theta}\frac{\partial}{\partial \theta}\right) \ . \tag{5.6}$$

This problem, namely the determination of the flow between two concentric spheres rotating with slightly different angular velocities, has already been studied by Proudman (1956) and Stewartson (1966) in the case where both boundaries were rotating rigidly (i.e., without latitudinal shear). The following section develops their results in the case where the top boundary is rotating differentially.

5.1.2.2 The calculation

Following the work of Proudman, the problem is first solved in the main body of the fluid, then successively near the bottom and top boundaries. In the main body of the tachocline, the viscous stresses are negligible, and the system simply reduces to

$$(\hat{\boldsymbol{e}}_z \cdot \nabla)\boldsymbol{u} = 0 \ , \tag{5.7}$$

which suggests that $\boldsymbol{u}$ is independent of z, so that the solutions are

$$\psi = \psi_0(s) \text{ and } \chi = \chi_0(s) \ . \tag{5.8}$$

In order to solve the problem near the lower boundary, Proudman introduces the stretched variable ζ such that

$$\zeta = (r - r_{\rm in}) E_\nu^{-1/2} \cos^{1/2}\theta \ . \tag{5.9}$$

This is equivalent to introducing a boundary layer with thickness $\delta = E_\nu^{1/2} \cos^{-1/2}\theta$. The equations (5.5) and (5.5) become, to zeroth order in $E_\nu^{1/2}$

$$\begin{aligned} \frac{\partial^5 \psi}{\partial \zeta^5} &= -4 \frac{\partial \psi}{\partial \zeta} \\ \frac{\partial^5 \chi}{\partial \zeta^5} &= -4 \frac{\partial \chi}{\partial \zeta} \ . \end{aligned} \tag{5.10}$$

Note that these approximations are not valid near the poles, where latitudinal derivatives may become important, and near the equator, where the thickness of the boundary layer δ di-

verges. These regions will be discussed later. Rigid rotation at the bottom boundary requires that $\chi \to 0$ as $r \to 1$, or $\zeta \to 0$. Moreover, the impermeable boundary condition requires that $\psi = 0$ on the boundary, as well as $\partial\psi/\partial\zeta = 0$. The solution to equations (5.10) and (5.10) which fulfills all these boundary conditions, and which is bounded as $\zeta \to \infty$ is

$$\begin{aligned} \psi(\zeta,\theta) &= \psi_1(\theta)\left(1 - e^{-\zeta}(\cos\zeta + \sin\zeta)\right) \\ \chi(\zeta,\theta) &= \chi_1(\theta)\left(1 - e^{-\zeta}\cos\zeta\right) , \end{aligned} \tag{5.11}$$

where $\psi_1(\theta)$ remains to be determined, and

$$\chi_1(\theta) = 2E_\nu^{-1/2}\cos^{1/2}\theta\psi_1(\theta) . \tag{5.12}$$

As $\zeta \to \infty$, these functions must match onto the solution obtained previously for the main body of the tachocline: it is then easy to see that one must have

$$\chi_1(\theta) = \chi_0(r_{\rm in}\sin\theta) \text{ and } \psi_1(\theta) = \psi_0(r_{\rm in}\sin\theta) . \tag{5.13}$$

This result can be combined with equation (5.12) and yields the matching condition

$$\chi_0(r_{\rm in}\sin\theta) = 2E_\nu^{-1/2}\cos^{1/2}\theta\psi_0(r_{\rm in}\sin\theta) . \tag{5.14}$$

In order to study the boundary layer near the top boundary, another stretched variable is introduced:

$$\xi = (r_{\rm out} - r)E_\nu^{-1/2}\cos^{1/2}\theta . \tag{5.15}$$

The scaled equations are the same as before (cf equations (5.10)); the boundary conditions for the stream function are also the same as for the lower boundary when $\chi \to 0$, but the differential rotation must now match onto that of the convection zone, so that

$$\chi(r = r_{\rm out},\theta) = r_{\rm out}^2\sin^2\theta\tilde{\Omega}_{\rm cz}(\theta) , \tag{5.16}$$

where

$$\tilde{\Omega}_{\rm cz}(\theta) = \Omega_{\rm eq}(1 - a_2\ \cos^2\theta - a_4\ \cos^4\theta) - \Omega_{\rm c}\ . \qquad (5.17)$$

The solutions to equations (5.10) which fulfill these conditions are

$$\begin{aligned} \psi(\xi,\theta) &= \psi_2(\theta)\left(1 - e^{-\xi}(\ \cos\xi + \ \sin\xi)\right)\ , \\ \chi(\xi,\theta) &= \chi_2(\theta) + 2E_\nu^{-1/2}\ \cos^{1/2}\theta\psi_2(\theta)e^{-\xi}\ \cos\xi\ , \end{aligned} \qquad (5.18)$$

with

$$\chi_2(\theta) = r_{\rm out}^2\ \sin^2\theta\tilde{\Omega}_{\rm cz}(\theta) - 2E_\nu^{-1/2}\ \cos^{1/2}\theta\psi_2(\theta)\ . \qquad (5.19)$$

As before, matching with the solution in the main body of the tachocline implies that

$$\psi_2(\theta) = \psi_0(r_{\rm out}\ \sin\theta) \text{ and } \chi_2(\theta) = \chi_0(r_{\rm out}\ \sin\theta)\ , \qquad (5.20)$$

so that

$$\chi_0(r_{\rm out}\ \sin\theta) = r_{\rm out}^2\ \sin^2\theta\tilde{\Omega}_{\rm cz}(\theta) - 2E_\nu^{-1/2}\ \cos^{1/2}\theta\psi_0(r_{\rm out}\ \sin\theta)\ . \qquad (5.21)$$

Since ψ_0 and χ_0 are functions of s only, the two matching conditions given by equations (5.14) and (5.21) can also be rewritten as

$$\begin{aligned} \chi_0(s) &= 2E_\nu^{-1/2}\left(1 - (s/r_{\rm in})^2\right)^{1/4}\psi_0(s)\ , \\ \chi_0(s) &= s^2\Omega'_{\rm cz}(s) - 2E_\nu^{-1/2}\left(1 - (s/r_{\rm out})^2\right)^{1/4}\psi_0(s)\ , \end{aligned} \qquad (5.22)$$

where

$$\Omega'_{\rm cz}(s) = \Omega_{\rm eq}\left[1 - a_2\left(1 - (s/r_{\rm out})^2\right) - a_4\left(1 - (s/r_{\rm out})^2\right)^2\right] - \Omega_{\rm c}\ , \qquad (5.23)$$

which can now be solved uniquely as

$$\psi_0(s) = \frac{E_\nu^{1/2}}{2} \frac{s^2 \Omega'_{\rm cz}(s)}{(1-(s/r_{\rm in})^2)^{1/4} + (1-(s/r_{\rm out})^2)^{1/4}} \ ,$$

$$\chi_0(s) = \frac{s^2 \left(1-(s/r_{\rm in})^2\right)^{1/4} \Omega'_{\rm cz}(s)}{(1-(s/r_{\rm in})^2)^{1/4} + (1-(s/r_{\rm out})^2)^{1/4}} \ . \qquad (5.24)$$

The flow within two spheres is now known analytically everywhere.

5.1.2.3 Failure of the boundary layer theory at the tangent cylinder

As it can be seen from equation (5.9), the thickness of the Ekman layer diverges near the equator, and the arguments presented in the previous section fail. The divergence is related to the existence of a "critical cylinder" of unit radius, beyond which the meridional flow from the convection zone does not reach the radiative zone (see Fig. 5.2). The problems arising near this region are extremely complex, and several boundary layers appear on the cylinder; Stewartson (1966) studied these effects in detail. The main results of his analysis are as follows: there exist several concentric cylindrical nested boundary layers with unit radius, and respective widths $E_\nu^{1/3}$, $E_\nu^{2/7}$ and $E_\nu^{1/4}$. The essential role of these boundary layers is to carry the return flow, that is, to ensure that the total mass into the tachocline from the convection zone is zero (see Fig. 5.3). This flow exerts a negligible torque on the radiative zone. Additional boundary layers occur near the corner where the unit cylinder meets the equator, and where the flow from the pole reaches the radiative zone; these can be neglected, since they are of no consequence for the transport of mass or angular momentum.

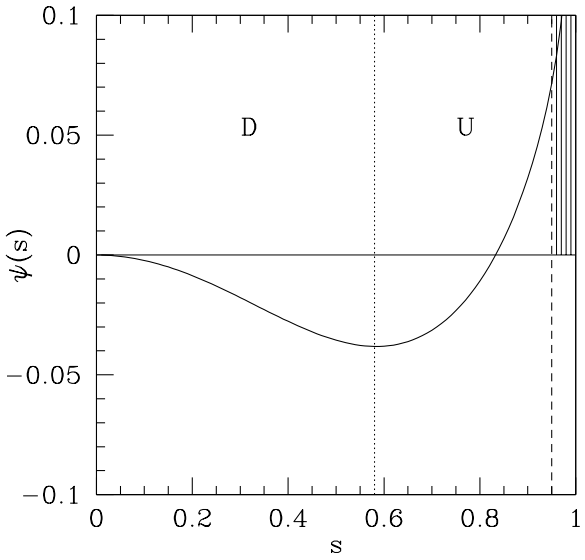

Figure 5.3: Stream function for the flow within the tachocline, as a function of cylindrical radius s. Note the downward flowing region (D), and the upward flowing region (U), separated by the dotted line at the cylindrical radius $s = 0.58$. The divergence near $s = 1$ occurs because of the divergence of the thickness of the boundary layer at the equator. A more thorough study would reveal downflows within a thin boundary layer close to $s = 1$ as well (represented here by the shaded area, to ensure that $\psi(s = 1) = 0$, as required. The width of the boundary layer has been exaggerated for the purpose of plotting.

5.1.3 Comparison with the numerical results

5.1.3.1 Ekman spiral

Within the tangent cylinder (i.e. for $r\ \sin\theta \leq r_{\rm in}$) the flow is well approximated by the Proudman asymptotic solution described in Section 5.1.2. The best way to compare the solution to the numerical solution is through the Ekman spiral. Calculating u_ϕ/r and u_θ/r yields

$$\begin{aligned} \frac{u_\phi}{r} &= \frac{\chi}{r^2\ \sin\theta}\ , \\ \frac{u_\theta}{r} &= -\frac{1}{r^2\ \sin\theta}\frac{\partial\psi}{\partial r}\ . \end{aligned} \tag{5.25}$$

This can be rewritten as,

- in the inner boundary layer,

$$\begin{aligned} \left.\frac{u_\phi}{r}\right|_{\rm in} &= \frac{2E_\nu^{-1/2}\ \cos^{1/2}\theta\psi_1(\theta)}{r_{\rm in}^2\ \sin\theta}(1-e^{-\zeta}\ \cos\zeta)\ , \\ \left.\frac{u_\theta}{r}\right|_{\rm in} &= -\ \frac{2E_\nu^{-1/2}\ \cos^{1/2}\theta\psi_1(\theta)}{r_{\rm in}^2\ \sin\theta}e^{-\zeta}\ \sin\zeta\ , \end{aligned} \tag{5.26}$$

- in the outer boundary layer,

$$\begin{aligned} \left.\frac{u_\phi}{r}\right|_{\rm out} &= \sin\theta\tilde{\Omega}_{\rm cz}(\theta) + \frac{2E_\nu^{-1/2}\ \cos^{1/2}\theta\psi_2(\theta)}{r_{\rm out}^2\ \sin\theta}(e^{-\xi}\ \cos\xi - 1)\ , \\ \left.\frac{u_\theta}{r}\right|_{\rm out} &= -\ \frac{2E_\nu^{-1/2}\ \cos^{1/2}\theta\psi_2(\theta)}{r_{\rm out}^2\ \sin\theta}e^{-\xi}\ \sin\xi\ . \end{aligned} \tag{5.27}$$

The Ekman spiral is created by plotting u_ϕ/r against u_θ/r at a fixed latitude. The following plot presents the asymptotic solutions as well as the true numerical solution for $\theta = \pi/12$, and two different values of the Ekman number. For this simulation, the angular velocity profile imposed on the outer boundary is chosen to be constant with value $\Omega = \Omega_{\rm c} + 10^{-5}$, and the angular velocity of the inner core is simply $\Omega_{\rm c}$. The no-torque condition is dropped. Note how the fit of the asymptotic analytical

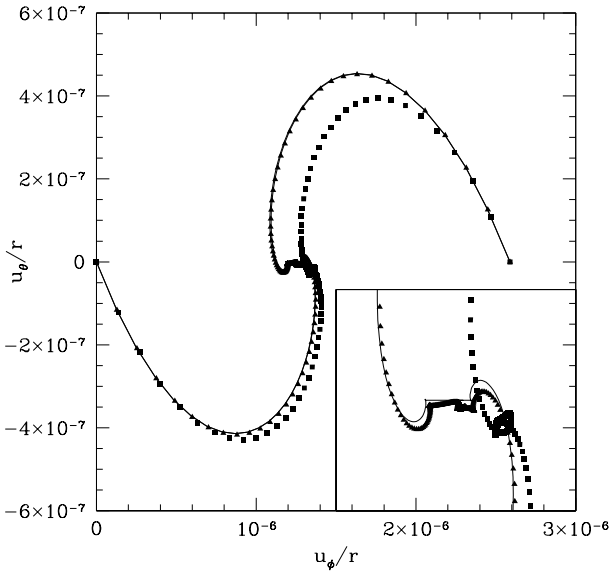

Figure 5.4: Predicted and calculated Ekman spirals for the simulation described in Section 5.1.3.1. The analytical prediction in shown as a continuous line, whereas the simulations are shown as square points for $E_\nu = 10^{-4}$ or triangular points for $E_\nu = 6.5 \times 10^{-6}$. The inset shows an enlargement of the central area.

prediction to the numerical solution is valid only provided the Ekman number is small enough. For larger Ekman numbers, viscosity plays a non-negligible role in the dynamics of the fluid outside the boundary layers, invalidating the Proudman asymptotic analysis.

5.1.3.2 Predictions of the interior rotation rate

Assuming that the sun is in equilibrium, the total torque applied by the tachocline on the radiative interior should be equal to that exerted by the solar wind on the convection zone. Since that torque is extremely small, it is assumed to be null as a first approximation, which is equivalent to requiring that the sun be in a steady state. This condition determines the interior rotation rate Ω_c uniquely.

In the model presented above, the torques applied by the tachocline onto the radiative zone are purely viscous, since the velocity terms vanish at the boundary with the radiative zone. As a result, the steady-state condition can be rewritten as

$$T_\nu(r=1) = 2\pi\nu \int_0^{\pi/2} \left[r^3 \sin^2\theta \frac{\partial \Omega}{\partial r} \right]_{r=1} \sin\theta \mathrm{d}\theta = 0 \ , \quad (5.28)$$

where T_ν is the total viscous torque from the tachocline onto the radiative zone, and $\Omega = \Omega_c + (\chi/r^2 \sin^2\theta)$ is the total angular velocity at the base of the tachocline. Using the results derived previously, this condition can be rewritten as:

$$\frac{\Omega_c}{\Omega_{eq}} = \frac{\int_0^{\pi/2} F(\theta) D(\sin\theta) \mathrm{d}\theta}{\int_0^{\pi/2} F(\theta) \mathrm{d}\theta} \ , \quad (5.29)$$

where

$$F(\theta) = \frac{\sin^3\theta \cos\theta}{\cos^{1/2}\theta + \left(1 - \sin^2\theta \frac{r_{in}^2}{r_{out}^2}\right)^{1/4}} \ . \quad (5.30)$$

and

$$D(s) = 1 - a_2 \left(1 - (s^2/r_{\rm out}^2)\right) - a_4 \left(1 - (s^2/r_{\rm out}^2)\right)^2 \qquad (5.31)$$

The variation of the calculated value of the interior rotation rate as a function of the width of the gap $\delta = r_{\rm out} - r_{\rm in}$ is presented in Fig 5.5. It can be seen that the simulations fit well the analytical predictions provided the Ekman number is small enough (i.e. below 10^{-6}). It is also interesting to note, as an aside, that for gap width of about 3% of the radiative zone's radius (which corresponds to the width of the tachocline), the interior angular velocity is 93% of the equatorial velocity, which is very close to the observed value for the interior rotation rate. This result, although quite striking, may be just a coincidence.

5.1.4 Numerical convergence

It is important to remember that the numerical system solved is not necessarily an accurate representation of the fluid dynamics equations, since the Fourier expansion of these equations is truncated at large order. The previous sections show that the numerical solutions seem to reproduce the analytical analysis reasonably well, hence it is likely that the numerical solutions presented actually represent a "converged" solution (i.e. a simulation for which the number of Fourier modes calculated is sufficiently large that the truncation has little influence on the solution). However, it is important to verify the convergence in a manner that can also be applied later to the magnetic simulations, for which there exists no analytical prediction with which to compare the solutions. The numerical convergence of the Fourier series can be checked be computing the typical amplitude of the Fourier modes Y_{jN+n} for $n = 1, .., N$. The amplitude is simply determined as the integral of the function $Y_{jN+n}(r)$ in the interval $[r_{\rm in}, r_{\rm out}]$. Fig. 5.6 shows these amplitudes as a function of the Fourier order n for the angular momentum functions Y_{4N+n}, and for the latitudinal velocity functions Y_{N+n} for two

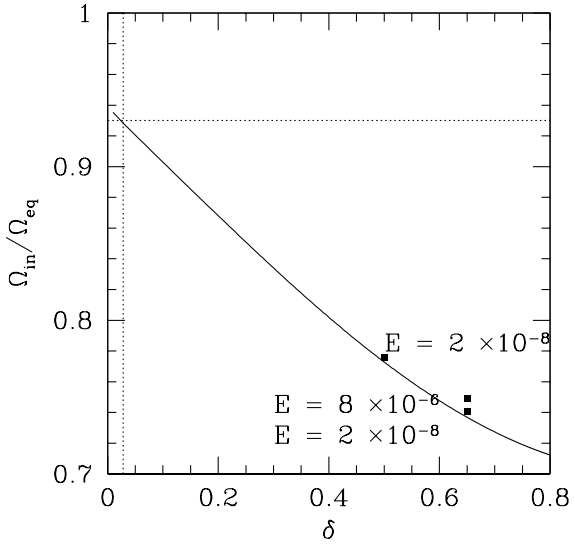

Figure 5.5: Analytical prediction for the interior rotation rate as a function of gap width δ, and results of simulations for $\delta = 0.5$ and $\delta = 0.65$ for values of the Ekman number as shown.

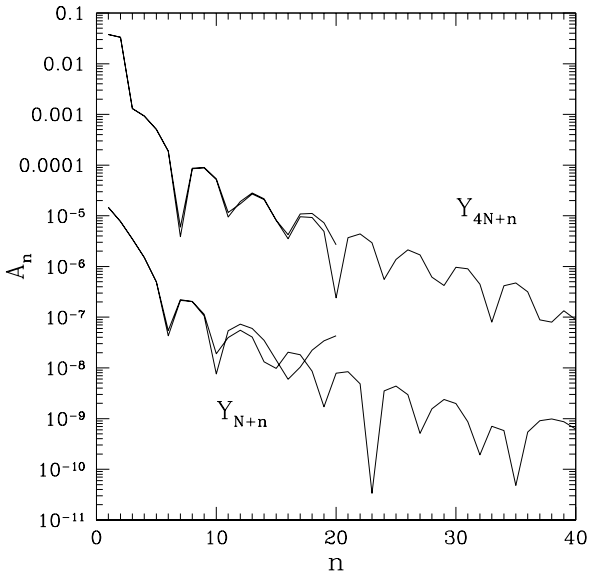

Figure 5.6: Amplitude of the Fourier modes of the angular momentum function Y_{4N+n} and the latitudinal velocity function Y_{N+n} as a function of n, for a simulation with $N = 20$ and $N = 40$.

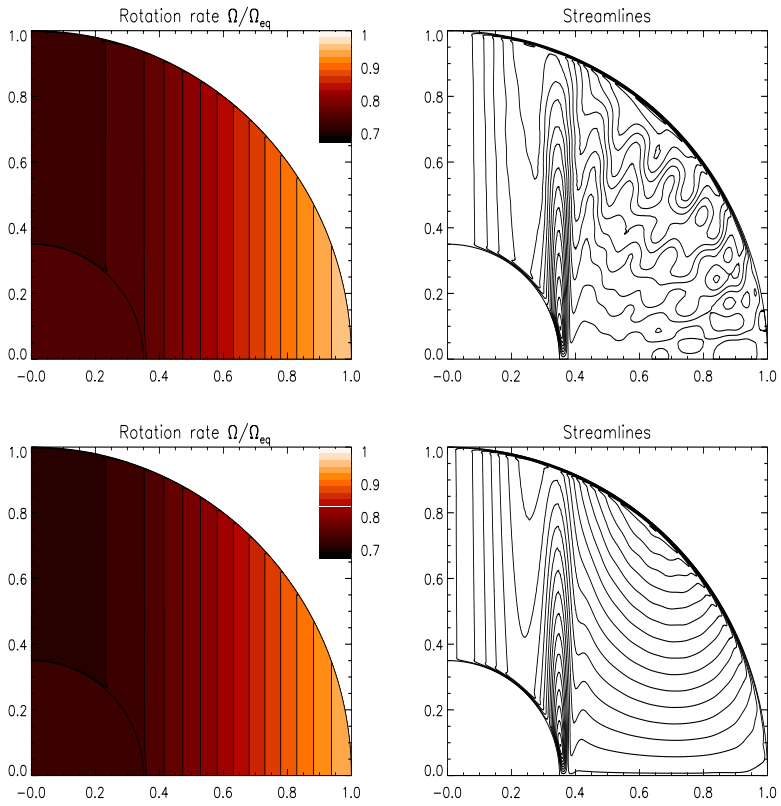

Figure 5.7: Comparison between two simulations with $N = 20$ (above) and $N = 40$ (below) for $E_\nu = 10^{-5}$

different total numbers of modes ($N = 20$ and $N = 40$), for $E_\nu = 10^{-5}$.

This example illustrates well the problems one may encounter by choosing to truncate the Fourier expansion at too low order. The Fourier series for the angular momentum function Y_{4N+n} appears to converge relatively well, with a gradual decrease of the amplitude of the modes with n for either $N = 20$ or $N = 40$. The two curves are hardly distinguishable. However, the same is not true of the latitudinal velocity functions Y_{N+n} for which the mode amplitudes flatten around $n = 20$ when the series is truncated at low order, but keeps on decreasing when the series is truncated at higher order, showing relatively good convergence. This intrinsic difference between the behaviours of the velocity function and the angular momentum function can also be seen in the final results. Fig. 5.7 shows the results of the simulations for both truncation orders $N = 20$ and $N = 40$. Note how the angular velocity contour plots for $N = 20$ and $N = 40$ are indistinguishable, whereas the streamlines contour plot obviously shows the lack of convergence of the Fourier expansion in the $N = 20$ case.

The angular velocity series seems to converge faster than the streamlines series; this suggests two comments. Firstly, that in order to check on the absolute numerical convergence of the system it is essential to use the slowest converging functions rather than the angular momentum functions. Secondly, this also explains why the numerical solutions in Section 5.1.3.2 for $E_\nu \simeq 10^{-8}$ predict the asymptotic values of the interior rotation rate very well despite the fact that for such low Ekman numbers, the number of modes kept in the simulations ($N = 40$) is far too low to represent a fully converged solution for the velocity functions. It is however large enough to represent a fully converged solution for the angular momentum function, and shows that the discrepancies in the velocity field have little influence on the angular velocity profile.

5.2 Results in the magnetic case

In the magnetic case, the influence of the magnetic field on the fluid depends essentially on two parameters: the field strength and the magnetic diffusivity. In the following section, three regimes are presented for varying Elsasser number. The Elsasser will then be fixed and Section 5.2.2 studies the dependence of the solution on the magnetic Ekman number.

5.2.1 Varying the field strength

In these first simulations, only the Elsasser number Λ is varied. Note that the definition of Λ defined in equation (4.5) uses the value of the amplitude of the radial component of the magnetic field on the inner boundary. Accordingly, it should normally be defined using the true value of the density on the lower boundary, which is of order of $\rho_{\rm in} = 20$ g cm^{-3} rather than the chosen uniform value of 1 cm^{-3}. As a result, in the sun, the true magnetic field strength on inner boundary corresponding to the Elsasser number Λ is

$$B_{\rm in} = \sqrt{\rho_{\rm in}\Lambda} r_{\rm c}\Omega_{\rm c} = \sqrt{\frac{\rho_{\rm in}}{\rho_0}} B_0 \ , \tag{5.32}$$

In any case, the quantitative predictions of the simulations should be interpreted with care, as a rough indications rather than precise predictions. The viscous and magnetic Ekman numbers chosen for these simulations are identical, with a value of 2.5×10^{-4}. This value was chosen for simplicity, as a value for which it is easy to obtain solutions for any value of the magnetic field strength.

5.2.1.1 Low-field case, $\Lambda = 1/25$

This first simulation is shown in Fig. 5.8, which presents the result in the case of a low Elsasser number. This corresponds to $B_0 = 0.25T$ and a true field strength $B_{\rm in} = 12T$ at $r = 0.35 r_{\rm c}$.

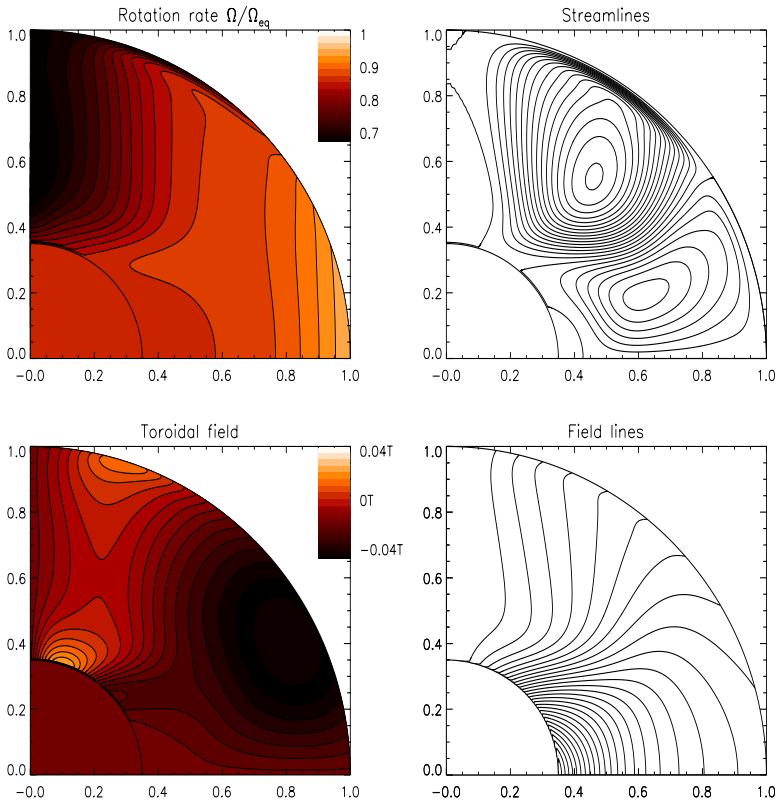

Figure 5.8: Simulation results for $\Lambda = 1/25$, $E_\nu = 2.5 \times 10^{-4}$, and $E_\eta = 2.5 \times 10^{-4}$.

The local Elsasser number near the surface is of order of 7×10^{-5}.

The structure of the interior angular velocity is dominated by centrifugal forces and the angular velocity profile is close to Proudman (cylindrical) rotation, except maybe very close to the inner core where the influence of a magnetic field can be seen through the slight deviation in the angular velocity contour lines. Because of the additional Lorentz forces in the momentum equation, the circulation is no more limited to cylindrical surfaces and takes a rather different pattern, with two cells that burrow deeply into the radiative zone. The shear layer at the tangent cylinder vanishes. Advection of the poloidal field by the circulation is strong despite the high magnetic diffusivity because of the strength of the circulation. In the polar regions, for example, the field is stretched to a structure that is nearly parallel to the rotation axis. Similarly, near the surface, the Ekman circulation strongly distorts the field by advecting it in a direction parallel to the surface. The shear persists throughout the fluid region, and as a result, leads to the winding up of the poloidal field into a relatively strong toroidal field. Typical values of the toroidal field are of order of one tenth of the value of the poloidal field near the core. This structure shows little resemblance with the observations, failing in particular to impose uniform rotation within the core.

5.2.1.2 High-field case, $\Lambda = 25$

The second simulation is shown in 5.9, which presents the result in the case of a high Elsasser number. This corresponds to $B_0 = 6.5T$. The local Elsasser number near the surface is typically of order of 4.5×10^{-2}.

In the strong-field case, (see Fig. 5.9), the system is strongly dominated by the Lorentz forces, and, as a result, is in a state close to Ferraro iso-rotation despite the relatively high magnetic diffusivity. The magnetic field is hardly affected by the cir-

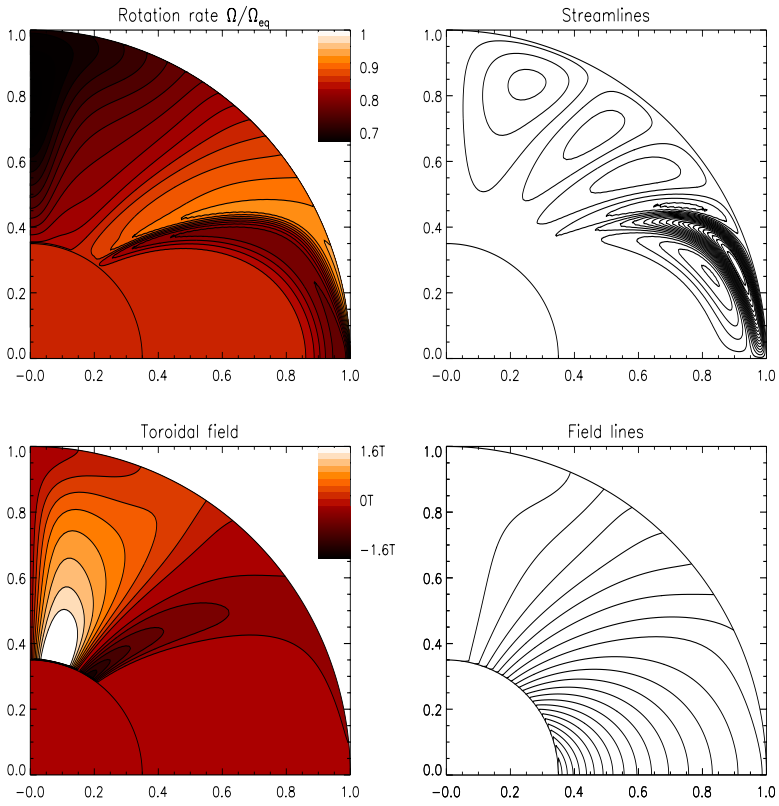

Figure 5.9: Simulation results for $\Lambda = 25$, $E_\nu = 1.25 \times 10^{-4}$, and $E_\eta = 1.25 \times 10^{-4}$.

culation, and keeps essentially its dipolar structure everywhere within the fluid region. The constant angular-velocity contours follow closely the magnetic field lines. Magnetic connection with the inner core is strong, and a large region near the equator is forced to rotate nearly uniformly with angular velocity $\Omega_{\rm in}$. On the other hand near the poles the shear persists at all radii and there exists a boundary layer near the inner boundary, of width

$$\delta = \left(\frac{\Lambda_{\rm loc} + \sqrt{\Lambda_{\rm loc}^2 + 4\mu^2 E_\eta^2}}{2 E_\nu E_\eta} \right)^{-1/2} , \qquad (5.33)$$

This boundary layer is discussed in detail in Section 5.3.1. The transition with the outer boundary is similar in the polar regions, but as the local Elsasser number is much smaller, the width of the boundary layer is much larger. However, in the equatorial regions the structure of the boundary layer is intrinsically different as the radial component of the poloidal field vanishes, as well as the magnetic stresses connecting that area with the boundary. That type of boundary layer is much wider than the Ekman-Hartman layer, with a typical width of order of

$$\delta = \left(\frac{E_\nu E_\eta}{\Lambda_{\rm loc}} \right)^{1/4} , \qquad (5.34)$$

A more detailed study of the equatorial regions is presented in Section 5.3.2.

The circulation is essentially limited to equatorial regions, with one strong principal cell and weak secondary ones. This cell advects rapidly rotating fluid from the equatorial regions, bringing angular momentum into the radiative zone, and brings more slowly rotating fluid from the interior out to large radii, where conservation of angular momentum slows it down even further. This process leads to the creation of an alternating shear structure, as it can be seen in Fig. 5.9. This type of solution contrasts strongly with the results presented by Rüdiger & Kitchatinov (1997) who found that the stronger the field the more uniform

the angular velocity of the interior. Their results fail to predict this structure because their simulations do not take into account the advection of angular momentum by the meridional flows. This alternating shear structure is well illustrated in the simulations presented by Dormy, Cardin & Jault (1998). The toroidal field is mostly limited to regions of shear (near the poles) with a very small amplitude in the co-rotating regions. It is worth mentioning that in this case, because the inner regions rotate almost uniformly, relaxing the rigidity condition within $r = r_c$ is likely to have little effect on the solution.

5.2.1.3 Intermediate-field case, $\Lambda = 1$

This third simulation is shown in Fig. 5.10, which presents the result in the case of an intermediate value of the Elsasser number. This corresponds to $B_0 = 1.3T$. The local Elsasser number near the surface is typically of order of 2×10^{-3}. The intermediate-field case reveals the emergence of two distinct regions: in the interior the system is dominated by the magnetic field, and is in a state close to isorotation, with a large region rotating with angular velocity $\Omega_{\rm in}$. However, closer to the outer boundary and especially near the equator, the system follows Proudman-column rotation.

The following phenomenon is happening. In the equatorial regions near the surface, the circulation is sufficiently strong to advect the magnetic field down, leaving a whole area below the convection zone virtually magnetic free, and therefore dominated by Coriolis forces. Flux conservation implies that the magnetic field strength is correspondingly increased in regions just below. This magnetic field evacuation by the circulation can be seen better in Fig. 5.12 which shows the square of the amplitude of the magnetic field on the equator(proportional to the local Elsasser number) as a function of radius. The plot shows particularly well the two regions:

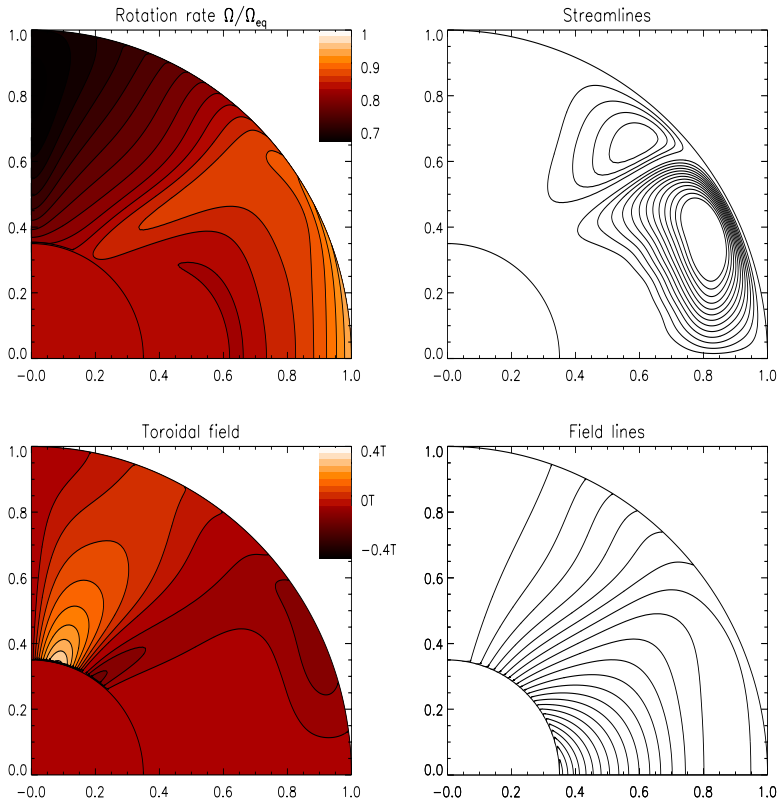

Figure 5.10: Simulation results for $\Lambda = 1$, $E_\nu = 2.5 \times 10^{-4}$, and $E_\eta = 2.5 \times 10^{-4}$.

1. in the core, the field is hardly perturbed by the differential rotation imposed on the top, and varies with r^{-3} just like the initially imposed dipolar field would (as represented by the dotted line).
2. the advection of the field by the circulation can easily be seen near the surface: just below the convection zone, the amplitude of the field is much smaller than the initial dipolar field, and slightly lower down the amplitude is much higher.

Conversely, the magnetic field keeps the circulation from burrowing deep into the radiative zone and confines it to a shallow region. This confinement can be seen in Fig. 5.10 but is represented best in Fig. 5.13, which shows the latitudinal component of the velocity as a function of radius. Note how the circulation is heavily suppressed below $r = 0.6 r_{\rm c}$.

5.2.2 Varying the magnetic diffusivity

When the magnetic diffusivity is decreased, as it is shown in Fig. 5.11, advection of the magnetic field by the circulation becomes more important compared to diffusion. This has several consequences:

1. the fluid is closer to being a perfect fluid, driving the the system closer to iso-rotation. A larger volume of fluid in the interior is rotating nearly uniformly with the interior angular velocity;
2. as can be seen in Fig. 5.11 and Fig. 5.12 the magnetic evacuation in the surface equatorial regions is greater, and occurs more abruptly as expected. The amplitude of the magnetic field below the evacuated volumes increases more rapidly;
3. as a result, the circulation is confined within a smaller volume by the magnetic field (see Fig. 5.13).

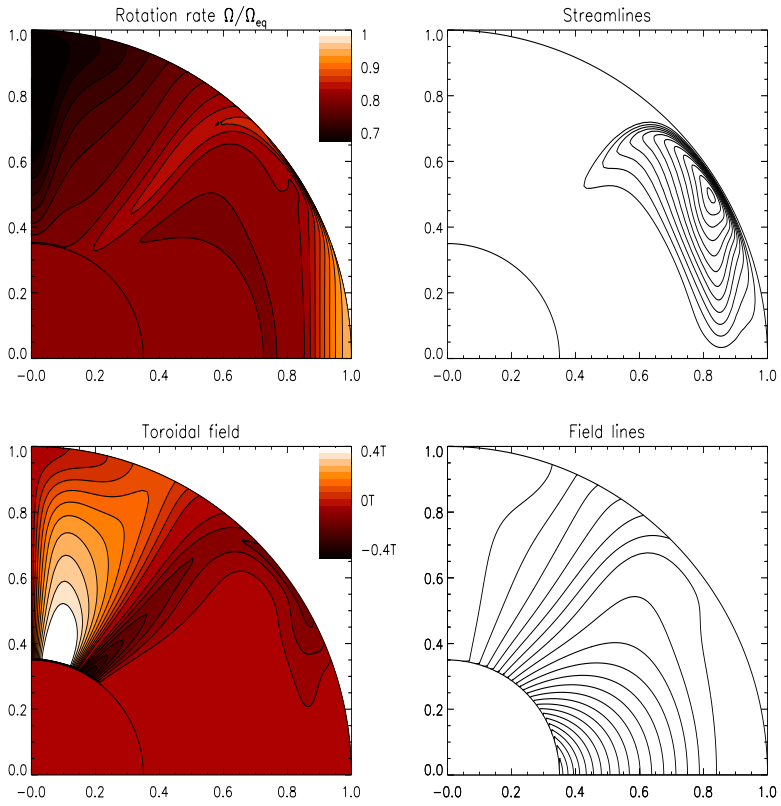

Figure 5.11: Simulation results for $\Lambda = 1$, $E_\nu = 6.25 \times 10^{-5}$, and $E_\eta = 6.25 \times 10^{-5}$.

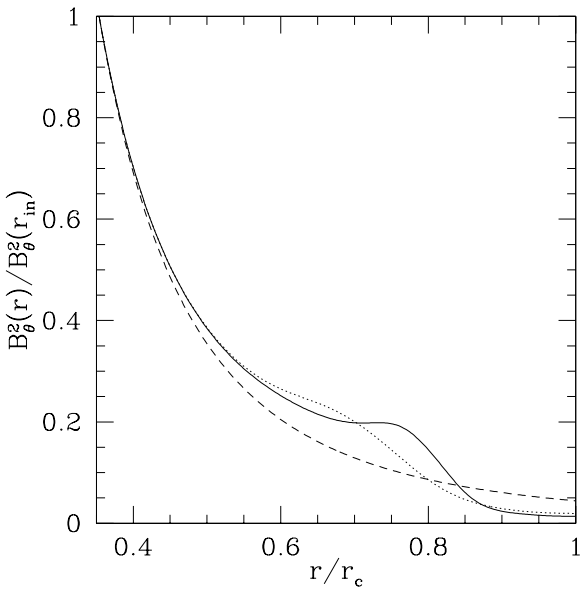

Figure 5.12: Normalized square of the amplitude of the magnetic field on the equator as a function of normalized radius for the simulation presented in Section 5.2.1.3 (i.e. with the parameter values $E_\nu = 2.5 \times 10^{-4}$, $E_\eta = 2.5 \times 10^{-4}$ and $\Lambda = 1$) (dotted line), and Section 5.2.2 (i.e. with the parameter values $E_\nu = 6.25 \times 10^{-5}$, $E_\eta = 6.25 \times 10^{-5}$ and $\Lambda = 1$) (solid line). The dashed line represents the same quantity for a non-rotating system, where the magnetic field solution is a dipolar field decaying as r^{-3}.

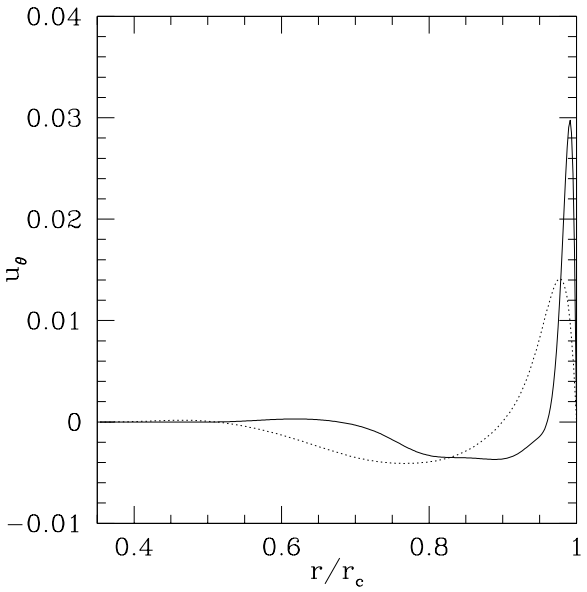

Figure 5.13: Latitudinal component of the velocity as a function of the normalized radius at colatitude $\theta = \pi/3$, in units of the azimuthal velocity $r_c\Omega_c$, for the simulation presented in Section 5.2.1.3 (i.e. with the parameter values $E_\nu = 2.5 \times 10^{-4}$, $E_\eta = 2.5 \times 10^{-4}$ and $\Lambda = 1$) (dotted line), and in Section 5.2.2 (i.e. with the parameter values $E_\nu = 6.25 \times 10^{-5}$, $E_\eta = 6.25 \times 10^{-5}$ and $\Lambda = 1$) (solid line).

5.2.3 Numerical accuracy

The mesh-point distribution described in Section 4.4.3 follows closely the variations of all the functions throughout the fluid region: the radial boundary layers are fully resolved. This can be shown best by looking for example at the variation of the latitudinal velocity Y_{N+n} with radius for $n = 1$ in Fig. 5.14. The numerical accuracy of the solution must also be checked with respect to the convergence of the Fourier expansion. In order to do this, the method which was presented in Section 5.1.4 for the non-magnetic case is adopted again. Fig. 5.15 shows the variation with Fourier order n of the amplitude of the modes for the angular momentum function Y_{4N+n}, for the two intermediate-field simulations presented above. Note again how the mode amplitudes flatten around $n = 20$ when the series is truncated at low order (see the comparison between the $N = 20$ and $N = 60$ simulations for the low-Ekman-number case). Comparing the left and right panels of Fig. 5.15 reveals that the amplitude of the modes decreases faster with n in the high-diffusivity case than in the low-diffusivity case. Indeed, for $n = 20$, the amplitude of the modes shown in the high-diffusivity case is an order of magnitude lower than in the low-diffusivity case.

The numerical convergence of the solution is therefore much harder to obtain for lower Ekman numbers. Contrary to common expectations, this is not due to the lack of resolution in the radial boundary layers (which are very well resolved for any Ekman number) but to the gradual flattening of the angular velocity profile, which is ill represented by Fourier expansion: a flat profile is very difficult to reproduce by a sum of oscillating functions, and a residual oscillation always exists with latitudinal order N, the order of the truncation of the Fourier series. This oscillation is of low amplitude and cannot necessarily be seen on the angular velocity contour plots, but affect strongly the meridional circulation which has an intrinsically low amplitude. Fig. 5.16 shows a typical example of a simulation in which the truncation order N is too low; an oscillation appears in the

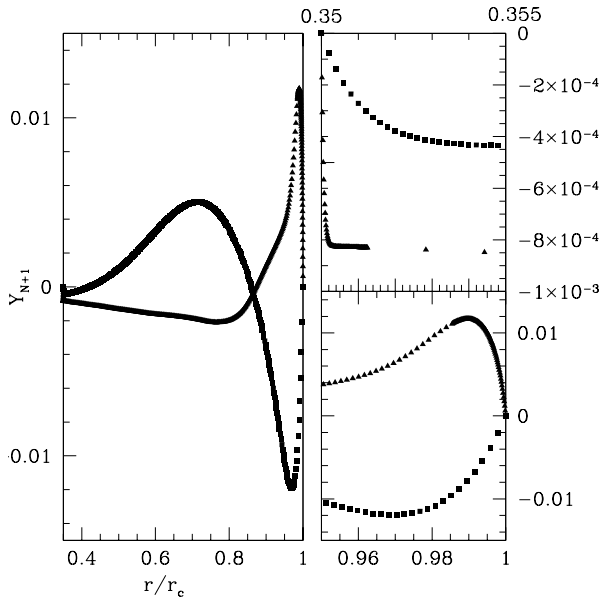

Figure 5.14: Variation of Y_{N+1} with radius for the simulations presented in Section 5.2.1.3 (squares) (which corresponds to "high" diffusivities) and Section 5.2.2 (triangles) (which corresponds to low diffusivities). The panel on the left shows the global variation between $r = r_{\rm in}$ and $r = r_{\rm out}$ and the panels on the right show a close up of the region near the boundaries (inner boundary for the top panel and outer boundary for the bottom panel).

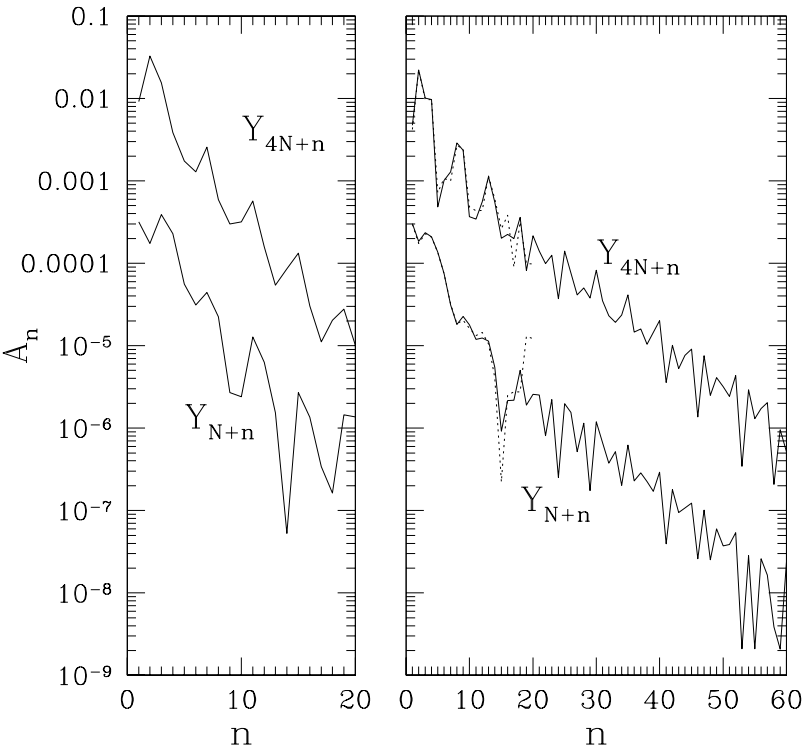

Figure 5.15: Amplitude of the Fourier modes of the angular momentum function Y_{4N+n} and the latitudinal velocity function Y_{N+n} as a function of n, for a simulation with $E_\nu = E_\eta = 2.5 \times 10^{-4}$ and $N = 20$ in the left panel, and $E_\nu = E_\eta = 6.25 \times 10^{-5}$ in the right panel, with $N = 20$ (dotted line) and $N = 60$ (solid line). The vertical axis is the same for both panels.

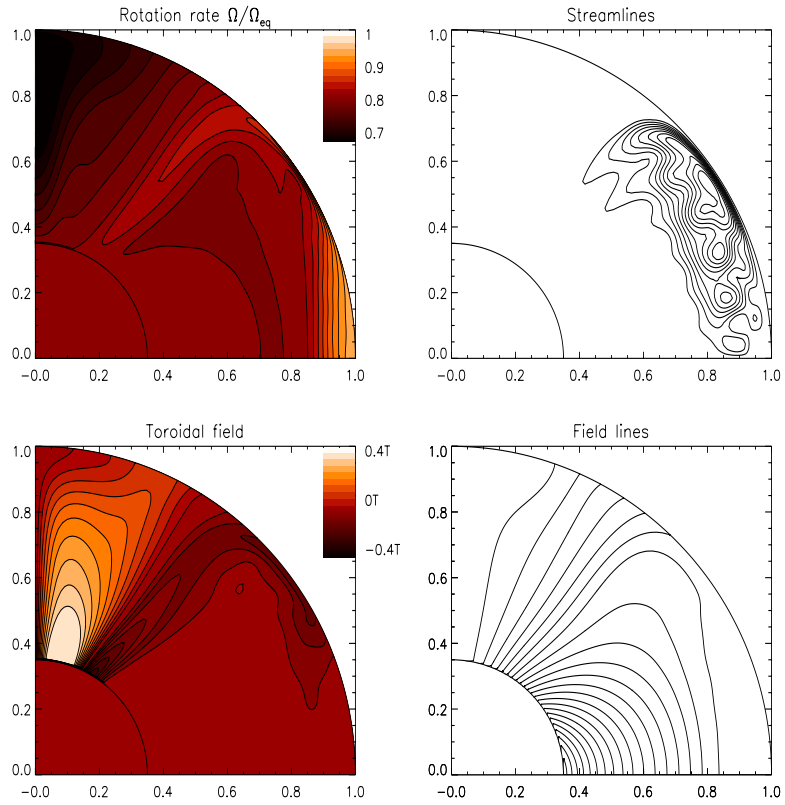

Figure 5.16: Typical example of a simulation with N too low. This simulation is for Ekman number of 6.25×10^{-5} as in Section 5.2.2 but with $N = 20$ instead of $N = 60$

solution with latitudinal order N.

5.3 Comparison with asymptotic analytical analysis

The simulations presented above represent a very good approximation of the true solution to the problem of the nonlinear interaction of a large-scale magnetic field with fluid motions in the radiative zone. Each of these solutions, however, represents up to several days of computer time, and the computation time increases strongly with decreasing Ekman numbers. For this reason, and also to compare the numerical results with theory, it is important to try and find approximate analytical solutions to the problem, even if it is only locally (near boundaries, or near the poles, for instance). This section focuses on the derivation of two asymptotic solutions near the boundaries, in the case where the magnetic field is mostly perpendicular to the boundary (which occurs near the poles) and in the case where the magnetic field is mostly parallel to the boundary (which occurs on the outer boundary near the equator).

5.3.1 Analysis of the boundary layer in the polar regions

5.3.1.1 Analytical derivation of the boundary layer solution

When the magnetic field is mostly perpendicular to the boundary, an Ekman-Hartman boundary layer develops (see the review by Acheson & Hide (1973)). The derivation of the boundary layer analysis in the case of a spherical boundary is outlined in the following section. Assuming that the magnetic field is essentially perpendicular to the boundary with constant amplitude B_0, one can write

$$\boldsymbol{B} = B_0 \hat{\boldsymbol{e}}_r \ . \tag{5.35}$$

The principal motivation for this model is the observation that in the polar regions, and near the interior boundary, the field is essentially radial. Call $x = r - r_{\rm in}$. Then, using the new subscripts "in" to identify the solution in the boundary layer on the inner sphere, the system of MHD equations yields

$$\begin{aligned} 2\mu\frac{\partial\psi_{\rm in}}{\partial x} &= \Lambda\frac{\partial S_{\rm in}}{\partial x} + E_\nu\frac{\partial^2 L_{\rm in}}{\partial x^2} \\ -\frac{1}{r_{\rm in}}\frac{\partial\psi_{\rm in}}{\partial x} &= E_\eta\frac{\partial b_{\rm in}}{\partial x} \\ -2\mu\frac{\partial L_{\rm in}}{\partial x} &= r_{\rm in}\Lambda\frac{\partial^2 b_{\rm in}}{\partial x^2} + E_\nu\frac{\partial^4\psi_{\rm in}}{\partial x^4} \\ \frac{\partial L_{\rm in}}{\partial x} &= -E_\eta\frac{\partial^2 S_{\rm in}}{\partial x^2}\ , \end{aligned} \tag{5.36}$$

where ψ is the stream function of the fluid flow, such that

$$v = \frac{1}{r}\frac{\partial\psi}{\partial r}\ ,\ u = \frac{1}{r^2}\frac{\partial\psi}{\partial\mu}\ . \tag{5.37}$$

Grouping these equations yields

$$-4\mu^2 E_\eta^2 F = \left(\Lambda - E_\nu E_\eta\frac{\partial^2}{\partial x^2}\right)^2 F\ , \tag{5.38}$$

where F represents $\frac{\partial^2 S}{\partial r^2}$, $\frac{\partial^2 b}{\partial r^2}$, $\frac{\partial^2\psi}{\partial r^2}$ and finally $\frac{\partial L}{\partial r}$. Looking for a solution of the kind $F \propto e^{\gamma x}$ yields

$$-4\mu^2 E_\eta^2 = \left(\Lambda - E_\nu E_\eta\gamma^2\right)^2\ , \tag{5.39}$$

and in turn, that $\gamma = \pm(\beta \pm i\alpha)$ where

$$\beta = \left(\frac{\Lambda + \sqrt{\Lambda^2 + 4\mu^2 E_\eta^2}}{2E_\nu E_\eta} \right)^{1/2} ,$$
$$\alpha = \left(\frac{-\Lambda + \sqrt{\Lambda^2 + 4\mu^2 E_\eta^2}}{2E_\nu E_\eta} \right)^{1/2} . \quad (5.40)$$

The solutions, which must be bounded, can then be written out as

$$Q_{\text{in}} = Q_{\text{in}}^c e^{-\beta x} \cos\alpha x + Q_{\text{in}}^s e^{-\beta x} \sin\alpha x + Q_{\text{in}}^1 x + Q_{\text{in}}^0 , \quad (5.41)$$

where Q is either of the three quantities S, b, or ψ, and

$$L_{\text{in}} = L_{\text{in}}^c e^{-\beta x} \cos\alpha x + L_{\text{in}}^s e^{-\beta x} \sin\alpha x + L_{\text{in}}^0 . \quad (5.42)$$

The term in Q^1, although not exactly bounded when going out of the boundary layer, must be kept in order to match the solution to that of the bulk of the fluid.

5.3.1.2 Comparison with the numerical solutions

In order to compare rigorously the simulations to the analytical solutions derived above, the matching of the solutions obtained in the boundary layer to those in the bulk of the fluid should be performed. However, the solution in the bulk of the fluid, in particular in the polar regions, is dominated by geometric effects (as the latitudinal derivatives near the poles are not necessarily negligible) and diffusive effects (as the Ekman numbers used in the simulations are not small enough to justify neglecting the diffusive terms); as a result, it is beyond to scope of this analysis to derive an analytical solution for the solutions in the bulk of the fluid, and therefore attempt such a matching. However, it is still possible to check the qualitative behaviour of the solutions

in the boundary layer. Fig. 5.17 shows the angular momentum function L as a function of the scaled variable $\xi = \beta x = \beta(r - r_{\rm in})$, for three different values of the Ekman numbers. Although the boundary conditions and asymptotic conditions are different for each case, this plots illustrates that the angular momentum function L indeed behaves as $e^{\beta x}$ within the boundary layer (i.e. for values of ξ below unity).

5.3.2 Analysis of the equatorial regions

5.3.2.1 An asymptotic analysis

Near the equator, the asymptotic analysis described in Section 5.3.1 breaks down, as the magnetic field is advected by the circulation into a a direction parallel to the surface. Another type of boundary layer appears, which is analysed in this Section.

The magnetic field is mostly parallel to the surface, in a region close to the equator so that $\mu \approx 0$. Assuming little variation in the latitudinal direction, the magnetic field is approximated by $\boldsymbol{B} \approx B_0 \hat{\boldsymbol{e}}_\theta$. In that case, and in the boundary layer only, the MHD equations can be simplified to

$$\begin{aligned} \Lambda \frac{B_0}{r_{\rm out}} \frac{\partial S}{\partial \mu} &= E_\nu L'' \\ \frac{B_0}{r_{\rm out}} \frac{\partial L}{\partial \mu} &= E_\eta S'' \ , \end{aligned} \tag{5.43}$$

where the primes denote differentiation with respect to r. These two equations entirely determine the variation of L and S near the boundary, and can be combined into

$$\frac{\partial^2 Q}{\partial \mu^2} = r_{\rm out}^2 \frac{E_\nu E_\eta}{\Lambda B_0^2} \frac{\partial^4 Q}{\partial \zeta^4} \ , \tag{5.44}$$

where Q is either L or S, and where the boundary layer coordinate $\zeta = r_{\rm out} - r$ was introduced. On the boundary, the

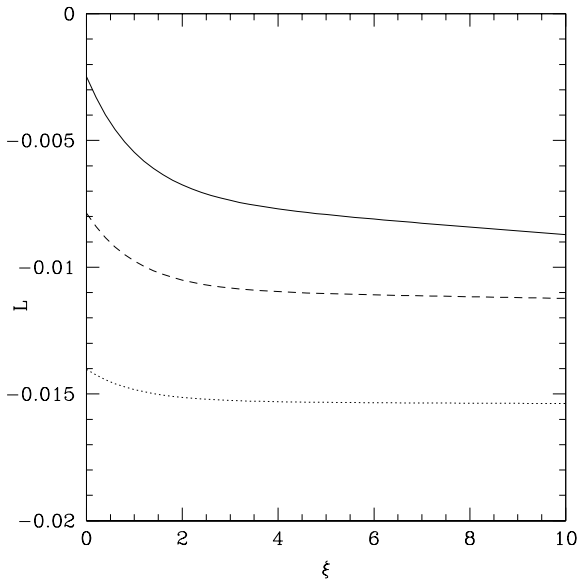

Figure 5.17: Variation with the scaled variable ξ of the angular momentum function L at fixed co-latitude $\theta = \pi/12$ and fixed Elsasser number $\Lambda = 1$, for three different values of the Ekman numbers: $E_\nu = E_\eta = 10^{-3}$ (solid line), $E_\nu = E_\eta = 2.5 \times 10^{-4}$ (dashed line) and $E_\nu = E_\eta = 6.25 \times 10^{-5}$ (dotted line).

latitudinal variation of L is given by the boundary conditions, so that

$$\frac{\partial^2 L}{\partial \mu^2} \approx 2(1-(a+1)\Omega_{\rm eq}) \approx -2L \ . \tag{5.45}$$

So finally, the governing boundary layer equation is

$$-2L = r_{\rm out}^2 \frac{E_\nu E_\eta}{\Lambda B_0^2} \frac{\partial^4 L}{\partial \zeta^4} \ , \tag{5.46}$$

and similarly for S. The solutions which are bounded as $\zeta \to \infty$ are

$$L = L^c(\mu) e^{\gamma_{\rm eq}\zeta} \cos(\gamma_{\rm eq}\zeta) + L^s(\mu) e^{\gamma_{\rm eq}\zeta} \sin(\gamma_{\rm eq}\zeta) \ , \tag{5.47}$$

and similarly for S, with

$$\gamma_{\rm eq} = \left(\frac{\Lambda B_0^2}{2 r_{\rm out}^2 E_\eta E_\nu} \right)^{1/4} \ . \tag{5.48}$$

Note that this analysis should predict the variation of the tachocline thickness with the interior field strenght in the model proposed by Rüdiger & Kitchatinov (1997), since in their model the magnetic field near the boundary is essentially parallel to the surface.

5.3.2.2 Comparison with the numerical solutions near the equator

The exact functional form of L and S remains unknown, as a full matching with the solution near the poles is needed to determine the unknown coefficients L^c, L^s, S^c and S^s. However, as a first comparison, it is easy to check whether the exponential dependency of the solution is indeed present in the numerical simulations. Fig. 5.18 presents the variation of $(L-L_{\rm c})/(L_{\rm eq}-L_{\rm c})$ on the equator as a function of normalized radius,

1. for the numerical solution as represented by the solid line

2. for the "analytical prediction" given by

$$\frac{L - L_c}{L_{eq} - L_c} \approx e^{\gamma_{eq}(r - r_{out})} , \tag{5.49}$$

as represented by the dotted line.

This simulation corresponds to the parameters $E_\eta = E_\nu = 6.25 \times 10^{-5}$ and $\Lambda = 1$. If higher Ekman numbers are chosen, the asymptotic analysis does not satisfyingly reproduce the solution. One can see that the general shape of the solution is well represented by the exponentially decaying solution with boundary layer width

$$\delta_{eq} = \left(\frac{\Lambda B_0^2}{2 r_{out}^2 E_\eta E_\nu} \right)^{-1/4} . \tag{5.50}$$

5.4 Discussion of the results

The results of these simulations are now discussed, by comparing them with other attempts at modeling the interaction between a differentially rotating fluid and a large-scale magnetic field, which were carried out by Dormy, Cardin & Jault (1998), and Gough & McIntyre (1998) respectively.

5.4.1 Comparison with the work of Dormy, Cardin & Jault (1998)

Dormy, Cardin & Jault (1998) studied the interaction between a large-scale magnetic field and fluid motions confined between two rotating rigid spherical shells, when the inner shell is rotating with a slightly faster angular velocity than the outer shell. The problem they study is very similar to the one proposed in this dissertation; in particular, in both cases the nonlinear advection by the meridional circulation is neglected whereas the full nonlinearity of the Lorentz forces and magnetic advection

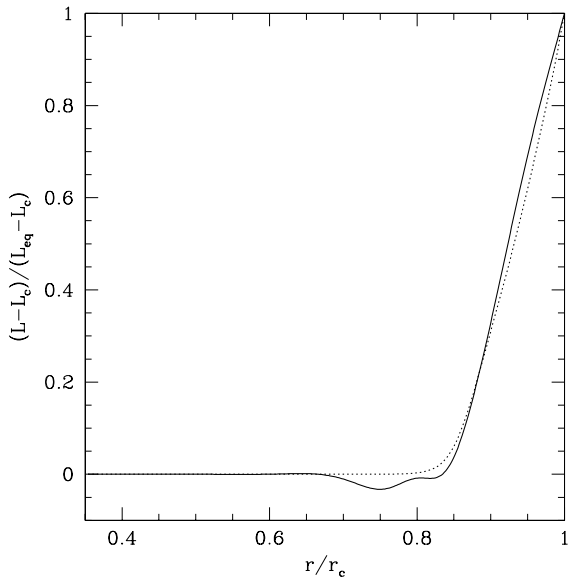

Figure 5.18: Variation with normalized radius of $(L - L_c)/(L_{eq} - L_c)$. The solid line is deduced from the numerical solution presented in Section 5.2.2 and the dotted line is the exponential solution described in equation (5.49)

terms is kept. However, their numerical method of resolution is slightly different as they evolve an initial configuration with time (starting from a uniformly rotating fluid with no meridional circulation and a given dipolar magnetic field) to an asymptotically steady state. The boundary conditions chosen by Dormy, Cardin & Jault for the magnetic structure are also slightly different as they choose to study the case of a conducting inner core and an insulating outer sphere (whereas in the simulations presented in this dissertation both spheres are conducting). This difference is essential to the results since in the insulating case, only viscous torques connect the fluid to the outer boundary, whereas in the conducting case the connection between the fluid and the boundary occurs principally via magnetic stresses.

Dormy, Cardin & Jault present the results of several simulations for increasing Elsasser number (note that their definition of the Elsasser number is different from the one used in this dissertation), and viscous Ekman number of $E_\nu = 10^{-5}$; unfortunately, they do not report on the value of the magnetic diffusivity used. Their simulations qualitatively match my own extremely well (see Fig. 14 of their paper for instance), assuming that they used a rather large magnetic Ekman number. More specifically, the following features reported in their work are worth noting:

1. As the Elsasser number is increased progressively from the non-magnetic case to the strong-field case, the shear layer at the tangent cylinder is progressively smoothed out and eventually disappears completely. The flow tends to a bulk rotation together with the inner sphere.
2. An Ekman-Hartman boundary layer develops near the outer boundary, whereas the shear disappears completely at the boundary with the inner sphere. No mention is made of a boundary layer at the inner sphere.
3. They observe that in the high Elsasser number case the angular velocity follows closely the field lines, and that an alternating shear layer develops from the equator inwards,

just as presented in Fig. 5.9. They argue that "this internal shear layer is associated with the recirculation of electric currents induced in the Hartman layer as the internal Stewartson layer is associated with the recirculation of the meridional flows generated in the Ekman layers".

4. They also observe that the width of the sheared zone near the equator "follows the $M^{-1/2}$ asymptotic law for boundary layer attached to a wall parallel to the imposed magnetic field (Moreau, 1990)", where $M = \Lambda_{\rm loc}/E$.

5. Finally, they observe an unexpected inversion of the angular velocity profile near the inner boundary, where the local angular velocity exceeds that of the inner shell.

Their results call for the following comments. Firstly, the shear near the inner boundary is indeed suppressed by the presence of the magnetic field in the equatorial regions, but not in the polar regions. It is therefore inexact to claim that no boundary layer is present near the inner boundary. An Ekman-Hartman boundary layer of the type described in the asymptotic analysis in Section 5.3.1 must necessarily be present in the polar region, as shown in Fig. 5.19. The jump across the boundary layer is *reduced* when the magnetic diffusivity is reduced, or when the magnetic field strength is increased. Secondly, Dormy, Cardin & Jault interpret the shear layer as the recirculation of electric currents within the radiative zone. I believe that another phenomenon is in play: Ekman-Hartman pumping drives a circulation from the boundary layer into the bulk of the flow. This circulation advects angular momentum from the outer regions into the radiative zone, accelerating the fluid there. However, because of the Ferraro iso-rotation law, this accelerated region is confined within a thin diffusive shear layer (which indeed has a thickness of $M^{-1/2}$, see Section 5.3.2). Finally, this phenomenon could also explain the angular velocity inversion they observe, where a portion of the fluid is rotating faster than either boundaries. In the case where the two boundaries are rotating with only slightly different angular velocities, it is not unlikely that the accelera-

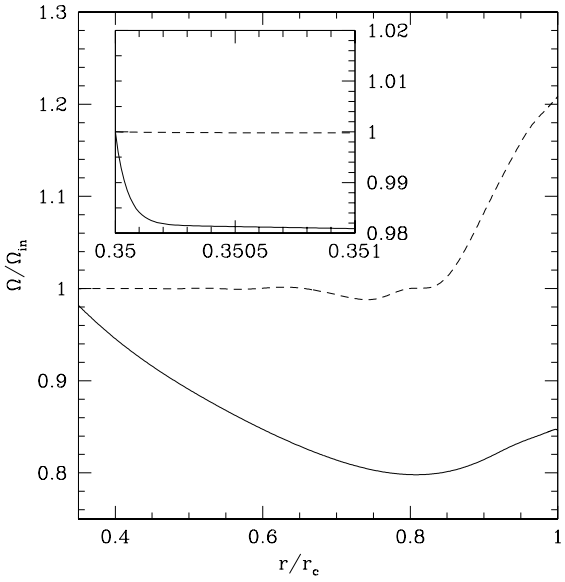

Figure 5.19: Variation with latitude of the angular velocity profile near the poles (solid line) and near the equator (dashed line) for the simulation described in Section 5.2.2. The inset shows an enlargement of the region near the inner boundary, and shows the existence of a boundary layer near the poles, but its suppression at the equator.

tion of the fluid as it is advected to smaller and smaller radii would result in velocities higher than that of either boundaries. However, despite the different interpretation of the results, the qualitative and quantitative agreement of the work presented in this dissertation with that of Dormy, Cardin & Jault is excellent.

Having shown how closely the simulations presented in Section 5.2.2 follow asymptotic analytical predictions, and also how well they compare to the simulations carried out by Dormy, Cardin & Jault (1998) it will from now on be assumed that the numerical solutions obtained through the method presented in Chapter 4 represent a sufficiently accurate approximation of the true solution of the model studied. The results are now analysed with respect to the observations.

5.4.2 Analysis of the results

Section 5.2.2 showed that there exists an intermediate magnetic field regime which holds the following properties: a large region of the fluid region is forced to rotate nearly uniformly with the angular velocity of the inner core. In the equatorial regions the transition to differential rotation occurs within a small shear layer, whereas in the polar regions the transition is more gradual, with a near-constant radial shear. The transition latitude between the "polar" regions and the "equatorial" regions seems to correspond to the latitude below which the radial component of the magnetic field is heavily suppressed on the outer boundary. In the equatorial regions, the shear layer is virtually magnetic-free, the poloidal field being pushed downwards by a large-scale meridional circulation. On the other hand, the circulation is confined to the shallower layers of the fluid region by the deep magnetic field. All these phenomena (the synchronization of the rotation with the inner core, the shallowness of the shear layer, the magnetic expulsion near the equator and the confinement of the circulation) are enhanced when the magnetic diffusivity is decreased.

This qualitative behaviour was predicted by Gough & McIntyre (1998), who first suggested that the tachocline should be virtually magnetic-free, and undergoing large-scale mixing by a confined circulation. The scaling argument they derive to predict the variation of the width of the tachocline with internal field strength does not apply here, however, since their model is based on thermal wind driving and includes advective heat transport. As a result, the quantitative predictions they propose cannot be reproduced by the simulations presented here. As an example, the typical timescale of the circulation in the model proposed by Gough & McIntyre is a local Eddington-Sweet timescale, whereas in the simulations presented here the circulation velocity is related to the typical Ekman velocities.

The final step of this analysis consists in comparing the numerical simulations with the observations. It is essential to keep in mind that the typical Ekman numbers of the simulations are several orders of magnitude larger than in the sun. In the region of the tachocline, assuming that the flow is not turbulent, the magnetic and viscous diffusion coefficients are of order of $\nu = 10\mathrm{cm}^2\mathrm{s}^{-1}$ and $\eta = 2 \times 10^3\mathrm{cm}^2\mathrm{s}^{-1}$, which implies that

$$E_\nu \simeq 10^{-15} \text{ and } E_\eta \simeq 2 \times 10^{-13} \ . \tag{5.51}$$

The main consequence of this discrepancy is that although the principal features of the interaction between fluid motions and large-scale fields in the sun can be studied through this method, it cannot provide reliable quantitative estimates unless the Ekman numbers are sufficiently low that an asymptotic state is reached, in which all the relevant dynamical interactions happen outside the thin boundary layers (such as it is observed in the non-magnetic case for example).

The simulations qualitatively reproduce the observations extremely well:

1. For sufficiently low magnetic diffusivity, a large region of the fluid is forced to rotate uniformly with the angular velocity of the core; such a uniform angular velocity profile in the radiative interior is clearly shown by the observations. The simulations suggest that polar regions seem to sustain some radial shear down to a latitude of about 50° for $E_\nu = E_\eta = 2.5 \times 10^{-4}$, and down to latitudes of about 60° for $E_\nu = E_\eta = 6.25 \times 10^{-5}$: the polar shear is gradually confined to higher and higher latitudes as the Ekman numbers are reduced. Helioseismic inversions still have too low a resolution to provide any reliable observations of the polar regions; this numerical model however predicts slower rotating fluid in the polar regions deep within the radiative zone, which is also a feature of the works of Rüdiger & Kitchatinov (1997) and Gough & McIntyre (1998). However, this prediction is principally dependent on the assumption of incompressibility of the fluid, and may be invalidated by future studies of the compressible case.

2. A thin boundary layer appears in which most of the shear is contained, in particular in the equatorial regions. The thickness of this shear layer is much larger than the observed thickness of the tachocline, a discrepancy which is again simply related to the high diffusivities used. Additional simulations will be needed to confirm the variation of the thickness and centre-position of the tachocline suggested by the simulations presented in Section 5.2.2. Observations seem to suggest a slight prolateness of the tachocline, which could indeed be related to these variations.

3. A meridional circulation is driven below the convection zone by Ekman-Hartmann pumping; this circulation is confined by the large scale poloidal field to shallow layers of the radiative zone. This result validates the analysis of the sound speed profile performed by Elliott & Gough (1999) (see Section 1.4.1) and also relates to the upper limits in the depth of the tachocline mixing suggested by observa-

tions of the abundances of light elements in the convection zone (see Section 1.4.4). Again the simulated depth of penetration of the circulation is much larger than suggested by the observations, a discrepancy which is due to the large diffusivities used for the numerical analysis, and possibly to the assumption of incompressibility also. Comparison between high- and low-diffusivity cases indeed show a significant reduction of the mixed layer depth for lower Ekman numbers.

Quantitative estimates, however, are still to be improved. In addition to the deficiencies pointed out above, the predictions of the value of the angular velocity of the interior do not match the observations. Figure 5.20 shows the predicted ratio of interior to equatorial angular velocities as a function of the Ekman number in the intermediate-field case and high-field case. The predictions fall quite short of the observed value of $\Omega_{\rm in}/\Omega_{\rm eq} = 0.93$, and this discrepancy seems to get worse as the diffusivities are decreased. The main reason for the slow rotation of the inner core is the following: the polar regions are the last to be affected by the shear expulsion, and rotate with a low angular velocity more or less at all radii. A slowly rotating region, connected to the core via magnetic stresses, necessarily imposes its slow rotation to the inner core. Once more, this discrepancy between the observations and the simulations are likely to be principally due to the large diffusivities used in the simulations: a lower magnetic diffusivity increases the ability of the magnetic field to impose isorotation, particularly in the polar regions. This effect could yield a more rapidly rotating core, and in fact, the results for the high field case in Fig. 5.20 seem to suggest that as the diffusivity is decreased even further, the angular velocity of the inner core may rise again towards the observed values.

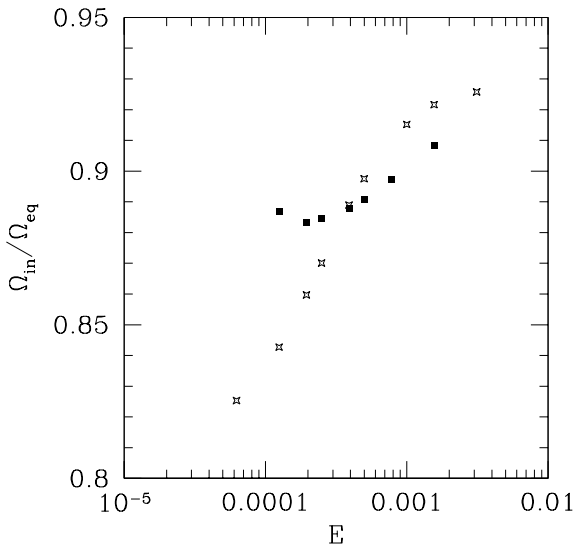

Figure 5.20: Interior angular velocity as a function of the magnetic Ekman number for the intermediate field case (stars) and the high field case (squares) .

Chapter 6

Effects of stratification and energy transport

Although the incompressible analysis presented in Chapter 5 is fairly successful in reproducing qualitatively the structure of the tachocline, it cannot take into account the effects of the hydrostatic stratification of the background, which is known to hinder motions in the radial direction, or of heat transport and thermal-wind driving. These effects are at the heart of the model proposed by Gough & McIntyre (1998) and are believed to play an important role in the dynamics of the tachocline. In particular, the effects of heat diffusion and stratification strongly reduce the typical velocities of the meridional circulation, which in turn will reduce the advective power of the circulation on the magnetic field. The MHD equations described in Chapter 4 are now modified to take into account these effects through a Boussinesq approximation of the fully compressible equations.

6.1 MHD equations in a Boussinesq approximation

The Boussinesq approximation was discussed in Chapter 2. The assumption that the typical flow velocities are much smaller than the local sound speed results in the filtering out of sound waves through the following mass continuity equation:

$$\nabla\cdot(\rho_{\rm h}\boldsymbol{u}) = 0 \ , \tag{6.1}$$

and the conclusion that the pressure perturbations are much smaller than the density or temperature fluctuations. In the case where the pressure is principally due to the gas pressure p, this approximation can be combined to the equation of state to yield

$$\frac{p}{p_{\rm h}} = \frac{\rho}{\rho_{\rm h}} + \frac{T}{T_{\rm h}} \approx 0 \ . \tag{6.2}$$

However, when magnetic pressure is present, this equation is no longer valid; instead, one should write

$$\frac{\Pi}{p_{\rm h}} = \frac{\rho}{\rho_{\rm h}} + \frac{T}{T_{\rm h}} \approx 0 \ , \tag{6.3}$$

where $\Pi = p + \boldsymbol{B} \cdot \boldsymbol{B}/8\pi$. This effect, which may result in the presence of strong local density fluctuations with no compensating temperature perturbations, leads to magnetic buoyancy. It has been neglected in this calculation as a first approximation, and equation (6.2) is assumed to be valid.

6.1.1 The equations

Under the Boussinesq approximation, the MHD equations in a compressible, axisymmetric fluid rotating with angular velocity $\Omega_{\rm c}$ take the following form:

$$\nabla\cdot(\rho_{\rm h}\boldsymbol{u}) = 0 \ , \tag{6.4}$$

which is rewritten as

$$r\frac{\partial u}{\partial r} = \frac{\partial v}{\partial \mu} - \left(2 + \frac{{\rm d}\ln\rho_{\rm h}}{{\rm d}\ln r}\right) u \ . \tag{6.5}$$

The azimuthal component of the momentum equation is essentially unaffected by the introduction of compressible effects in the Boussinesq approximation, except by the introduction of a

varying density profile, namely

$$\begin{aligned} & 2\mu v + 2(1-\mu^2)u + \frac{\Lambda}{\rho_{\rm h}}\left(\frac{b}{r^2}\frac{\partial S}{\partial \mu} - \frac{B}{r}S'\right) \\ = \; & \frac{E_\nu}{r}\left(L'' + \frac{1-\mu^2}{r^2}\frac{\partial^2 L}{\partial \mu^2}\right) \; . \end{aligned} \tag{6.6}$$

Note that the radial and latitudinal components of the momentum equation are unchanged in the linearized approximation of small perturbations.

The azimuthal component of the vorticity equation becomes

$$\begin{aligned} \nabla\times((2\boldsymbol{\Omega}_{\rm c}+\boldsymbol{\omega})\times\boldsymbol{u})_\phi = & -\frac{1}{\rho_{\rm h}^2}\left(\nabla p\times\nabla\rho\right)_\phi + \frac{1}{\rho_{\rm h}}\nabla\times(\boldsymbol{j}\times\boldsymbol{B})_\phi \\ & + \nu\left(\nabla^2\boldsymbol{\omega}\right)_\phi \; . \end{aligned} \tag{6.7}$$

The effect of the thermal-wind driving has been discussed in more detail in Chapter 2 and by Gough & McIntyre (1998). Equation (6.7) can now be rewritten as

$$\begin{aligned} & -2\mu L' - 2\frac{1-\mu^2}{r}\frac{\partial L}{\partial \mu} \\ + \; & \frac{\Lambda}{\rho_{\rm h}}\left[\frac{2}{r}BJ + \frac{b}{r}\frac{\partial J}{\partial \mu} + \frac{2\mu}{1-\mu^2}\left(\frac{S}{r^2}S' + J\frac{b}{r}\right) - J'B\right] \\ = \; & \frac{g_{\rm h}}{T_{\rm h}}(1-\mu^2)\frac{\partial T}{\partial \mu} + E_\nu\left(W'' + \frac{1-\mu^2}{r^2}\frac{\partial^2 W}{\partial \mu^2}\right) \; . \end{aligned} \tag{6.8}$$

In order to derive this equation from the curl of the momentum equation, two terms were neglected:

1. in the baroclinic term, the contribution from the latitudinal pressure gradient,

$$\frac{\partial p}{\partial \theta}\frac{\partial \rho_{\rm h}}{\partial r} \; , \tag{6.9}$$

(it is found that the inclusion of that term has little effect on the results of the simulations)

2. in the magnetic term, the contribution from the density fluctuations:

$$-\frac{1}{\rho_{\rm h}^2}\left(\nabla\rho\times(\boldsymbol{j}\times\boldsymbol{B})\right)_\phi \ . \tag{6.10}$$

Finally, the energy transport equation is linearized to obtain

$$\rho_{\rm h}T_{\rm h}\boldsymbol{u}\cdot\nabla s = \nabla\cdot(K_{\rm t}\nabla T) \ , \tag{6.11}$$

which can be rewritten as

$$-\frac{T_{\rm h}c_{\rm p}N^2}{g_{\rm h}^2}\boldsymbol{u}\cdot\nabla p = \nabla\cdot(K_{\rm t}\nabla T) \ . \tag{6.12}$$

Expanding this into the spherical coordinate system, and using the identities

$$\frac{\partial p}{\partial r} \simeq -\rho_{\rm h}g_{\rm h} \ , \ \frac{1}{r}\frac{\partial p}{\partial\theta} \simeq \rho_{\rm h}r\Omega_{\rm c}^2\ \sin\theta\ \cos\theta \ , \tag{6.13}$$

(which are derived from the radial and latitudinal components of the momentum equation respectively), the energy equation becomes:

$$\frac{T_{\rm h}c_{\rm p}N^2}{g_{\rm h}^2}\left(u\rho_{\rm h}g_{\rm h} - v\mu\rho_{\rm h}r\Omega_{\rm c}^2\right) = \nabla\cdot(K_{\rm t}\nabla T) \ , \tag{6.14}$$

The buoyancy frequency N^2 is approximated to be that of the hydrostatic background stratification. This approximation may not be valid if the mixing in the tachocline region due to the meridional circulation is strong enough to create a local adiabatic stratification (i.e. if the mixing occurs on a timescale much shorter than the thermal diffusion timescale).

6.1.2 Fourier expansion

As previously, all the relevant quantities are expanded into series of Chebyshev polynomials. The symmetry of the system requires

that

$$T = \sum_{n=1}^{N} Y_{11N+n}(r) T_{2n-2}(\mu) \ , \tag{6.15}$$

$$r^2 T' = \sum_{n=1}^{N} Y_{12N+n}(r) T_{2n-2}(\mu) \ . \tag{6.16}$$

The conservation of mass becomes

$$r Y_k' = Y_{N+k} - F_1(r) Y_k \ , \tag{6.17}$$

for $k = 1..N$, where

$$F_1(r) = 2 + \frac{\mathrm{d} \ln \rho_\mathrm{h}}{\mathrm{d} \ln r} \ . \tag{6.18}$$

In the momentum equation, Λ is everywhere replaced by $F_2(r)\Lambda$ where

$$F_2(r) = \frac{M_\odot}{r_\mathrm{c}^3} \frac{1}{\rho_\mathrm{h}} \ , \tag{6.19}$$

where ρ_h is given in cgs units. The vorticity equation (4.20) has the following additional term in the r.h.s.:

$$-\frac{2}{\pi} F_3(r) Y_{11N+m} B_{2k-1,2m-2} \ , \tag{6.20}$$

for $k = 1, .., N$, where the summation convention is used for m and

$$F_3(r) = \frac{1}{r_\mathrm{c} \Omega_\mathrm{c}^2} \frac{g_\mathrm{h}}{T_\mathrm{h}} \ , \tag{6.21}$$

where ρ_h and T_h are given in cgs units. Also, Λ is again everywhere replaced by $F_2(r)\Lambda$. Finally, the energy equation is expanded into

$$\begin{aligned} Y_{12N+1}' &= -\frac{F_4(r)}{2} Y_1 + \frac{F_5(r)}{8} \left(Y_{N+1} - Y_{N+2} \right) \\ &- \frac{1}{\pi} (m-1) Y_{11N+m} (B_{0,2m-3} - B_{0,2m-1}) \ , \end{aligned} \tag{6.22}$$

and

$$\begin{aligned} Y'_{12N+k+1} =& \frac{F_4(r)}{2}\left((2k-1)Y_{k+1} - (2k+1)Y_k\right) \\ &+ F_5(r)\left(Y_{N+k+1} + Y_{N+k} - Y_{N+k+2}\right. \\ &\left. - Y_{N+k-1} - Y_{N+1}\delta(k-1)\right) \\ &- \frac{2}{\pi}(m-1)Y_{11N+m}(B_{2k,2m-3} - B_{2k,2m-1}) \ , \end{aligned} \tag{6.23}$$

for $k = 1..N-1$, where

$$F_4(r) = r_{\rm c}^3\Omega_{\rm c}\frac{\rho_{\rm h}c_{\rm p}N_{\rm h}^2T_{\rm h}}{K_{\rm t}g_{\rm h}}r^2 \ , \ F_5(r) = -r_{\rm c}^4\Omega_{\rm c}^3\frac{N_{\rm h}^2T_{\rm h}\rho_{\rm h}c_{\rm p}}{g_{\rm h}^2K_{\rm t}}r^3 \ , \tag{6.24}$$

where all the quantities in the fractions are given in cgs units.

The variation with r of the functions F_1, F_2, F_3, F_4 and F_5 is given in Fig. 6.1. These are determined using the solar model computed by Christensen-Dalsgaard et al. (1996). Note that the absolute value of the function $F_5(r)$ is everywhere much smaller than $F_4(r)$, which implies that the latitudinal advection of heat is negligible everywhere except very close to the boundaries, where u vanishes faster than v.

6.1.3 Boundary conditions

The boundary conditions for the temperature fluctuations are derived from the assumption that the material outside the fluid region conducts heat, and has no fluid motion. In the steady-state case, the temperature fluctuations are subject to

$$\nabla^2 T = 0 \ , \tag{6.25}$$

in the inner core ($r \leq r_{\rm in}$) and for $r \geq r_{\rm out}$. The solution to this equation within the inner core is a linear combination of $P_n(\mu)r^n$, and the resulting matching conditions with the fluid

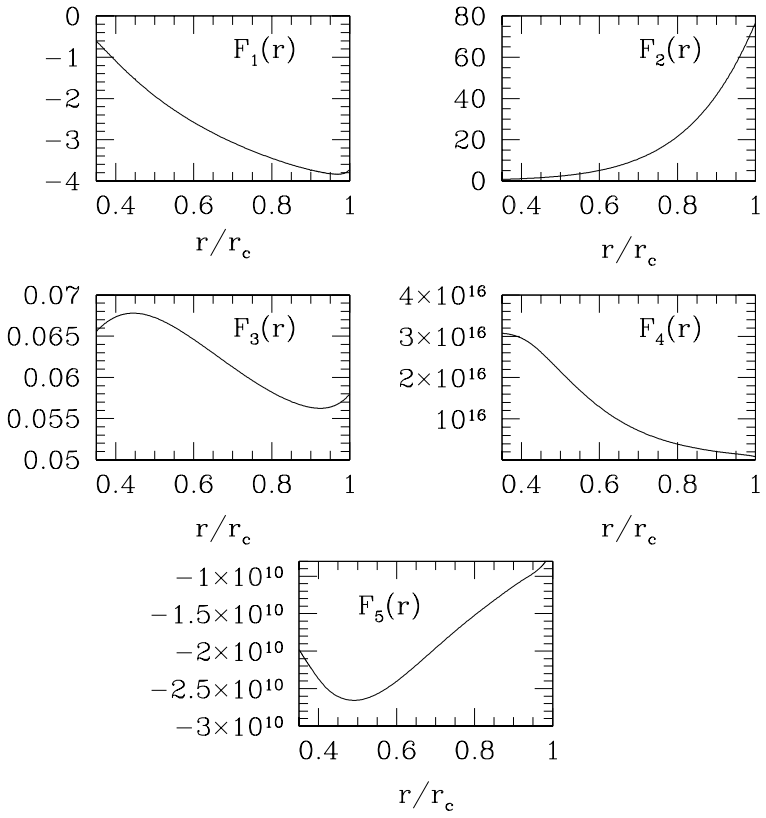

Figure 6.1: Variation with r of functions F_1, F_2, F_3, F_4 and F_5

region through the inner boundary is

$$\begin{aligned} & \sum_{1}^{N} Y_{12N+m}(r_{\rm in}) I_{2k,2m-2} \\ = \quad & 2k \sum_{1}^{N} r_{\rm in} Y_{11N+m}(r_{\rm in}) I_{2k,2m-2} \ , \end{aligned} \tag{6.26}$$

for $k = 1, .., N$. The solution to equation (6.25) that decays when $r \to \infty$ is a linear combination of $P_n(\mu) r^{-n-1}$ so that the resulting matching condition with the fluid region on the outer boundary is

$$\begin{aligned} & \sum_{1}^{N} Y_{12N+m}(r_{\rm out}) I_{2k,2m-2} \\ = \quad & -(2k+1) \sum_{1}^{N} r_{\rm out} Y_{11N+m}(r_{\rm out}) I_{2k,2m-2} \ , \end{aligned} \tag{6.27}$$

for $k = 1, .., N$.

6.2 Results in the non-magnetic case

Although it is treated here as a preliminary analysis to the magnetic case, the non-magnetic steady-state analysis of a stratified, rotating self-gravitating fluid is itself an interesting problem, in particular in the case of the sun. As mentioned in Section 2.1.2, rotation leads to baroclinicity, which in turn drives a meridional circulation due to the thermal wind: the Eddington-Sweet circulation (Sweet, 1950). It is not the aim of the following section to study in detail the Eddington-Sweet theory, although the numerical procedure used could, in principle, be used for such a purpose.

The principal problem in the study of the effects of compressibility and heat transport on the rotation profile of the sun is linked

to the very delicate advection-diffusion balance of heat. This problem soon becomes apparent when a steady-state solution for the model presented in Section 6.1 is seeked. The numerical method used for the resolution of the equations starts from an initial guess and iterates the NRK algorithm (see Section 4.4) until a solution is found with the desired accuracy. This method is also used to progressively explore the parameter space (for viscosity, magnetic diffusivity, etc...). When heat transport is studied, another parameter comes into play, the heat conductivity K_t, or if a dimensionless parameter is preferred, the Prandtl number $\sigma = \rho_\mathrm{h} c_\mathrm{p} \nu / K_\mathrm{t}$ which describes the ratio of the viscous diffusion timescale to the heat diffusion timescale. When trying to find solutions for progressively lower viscosity, there are two ways of proceeding: either the heat conductivity is fixed to its true solar value, and the viscosity alone is progressively reduced, or the Prandtl number is fixed to its value in the tachocline σ_0, for instance (in fact, the Prandtl number varies little with radius in the sun), which implies that the heat diffusivity must be varied with the Ekman number as

$$K_\mathrm{t} = \frac{\rho_\mathrm{h} c_\mathrm{p} E_\nu r_\mathrm{c}^2 \Omega_\mathrm{c}}{\sigma_0} \tag{6.28}$$

In the first case, the simulations tend to have an abnormally large viscous diffusion compared to heat diffusion. This implies that meridional motions are strongly suppressed, since all but the slowest motions would create large temperature fluctuations. In the second case, heat diffusion dominates over viscous diffusion (as it is the case in the sun), but the diffusive timescale is abnormally small compared to the typical turnover timescale (which implies that temperature fluctuations tend to be smoothed out).

Both approaches have been studied, in order to choose which method would be most suitably used in the magnetic case.

6.2.1 Fixing the heat capacity

This approach should be the most natural, as only one parameter (the viscosity) deviates from its normal solar value. It was chosen, for instance, by Elliott (1996). The results are shown in Fig. 6.2 for an Ekman number $E_\nu = 10^{-5}$ and solar values for the heat conductivity K_t, and compare well with the results obtained by Elliott. It is found that the system is essentially dominated by viscous stresses and thermal-wind driving, and the following equations apply:

$$(\nabla^2 \boldsymbol{u})_\phi = 0 \,, \tag{6.29}$$

$$2\nabla\times(\boldsymbol{\Omega}_\mathrm{c}\times\boldsymbol{u})_\phi = \nabla\times\left(\frac{\nabla p}{\rho}\right)_\phi \,. \tag{6.30}$$

As mentioned previously, the meridional circulation is heavily suppressed by the stratification of the background, since heat diffusion is weak compared to viscous diffusion. As a result, the angular velocity of the system is entirely determined through equation (6.29), and imposes the temperature perturbation through equation (6.30). The rotation rate of the inner core is $\Omega_\mathrm{in} = 0.957\Omega_\mathrm{eq}$. This is exactly the value obtained when calculating the interior rotation rate assuming that no other forces but viscous forces are in play: in this case, assuming that the viscous torques vary little with radius, the interior rotation rate is given by the requirement that the total viscous torque at the *top* boundary vanishes:

$$\int_0^1 (1-\mu^2)(\Omega_\mathrm{cz}-\Omega_\mathrm{in})\mathrm{d}\mu = 0 \tag{6.31}$$

which determines uniquely $\Omega_\mathrm{in} = 0.957\Omega_\mathrm{eq}$.

Obviously, such a solution is undesirable, for the following reasons:

- it is not possible to evaluate numerically the meridional circulation in this approach, because typical amplitudes of the

latitudinal and radial velocities are of order of $10^{-16} r_c \Omega_c$, which is close to machine-accuracy.

- the solar angular rotation profile is not dominated by viscous stresses. It is therefore inappropriate to try determine a reasonable solar rotation model starting from such an obviously inadequate guess.

6.2.2 Fixing the Prandtl number

When the Prandtl number is fixed, heat diffusion is important throughout the fluid motions, which allows the meridional circulation to bury into the radiative zone despite the stratification of the fluid. This simple fact should drastically change the dynamics of the system.

In order to verify this claim, the heat conductivity K_t is replaced in the simulations by the constant $\rho_h c_p E_\nu r_c^2 \Omega_c / \sigma_0$ where $\sigma_0 = 10^{-6}$. This implies that for the following simulations,

$$K_t = \frac{\rho_h c_p E_\nu r_c^2 \Omega_c}{\sigma_0} \simeq 5 \times 10^{29} E_\nu \ . \tag{6.32}$$

The Prandtl number in the sun varies little with radius, so that taking it as a constant throughout the fluid region is a reasonably good approximation. The results of the non-magnetic simulations in this case are shown in Fig. 6.3, for an Ekman number $E_\nu = 5 \times 10^{-6}$, and reveal a dynamical system intrinsically different from the one presented in the previous section. Ekman pumping on the boundaries drives a meridional circulation, as it was already observed in the incompressible case (see Section 5.1). However, the temperature stratification of the background resists the radial motions and slows down the circulation compared to the incompressible case (see Fig. 6.4). As a result, Coriolis forces do not necessarily dominate the motion in the momentum equation – viscous forces can be of equal importance. This implies in particular that the streamlines are no

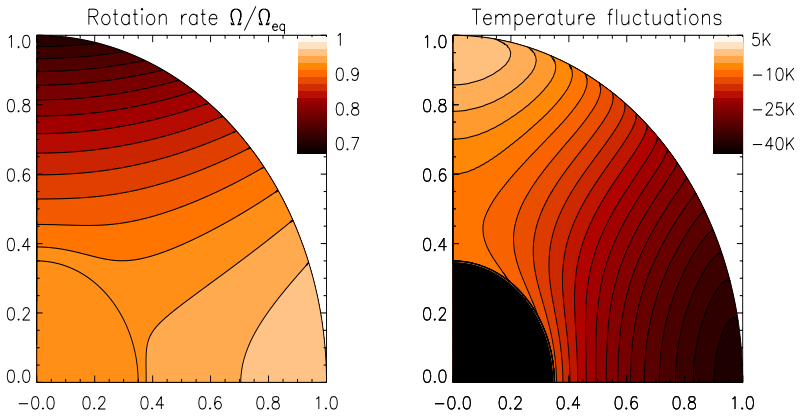

Figure 6.2: Solution to the non-magnetic case described in Section 6.2.1 for $E_\nu = 10^{-5}$

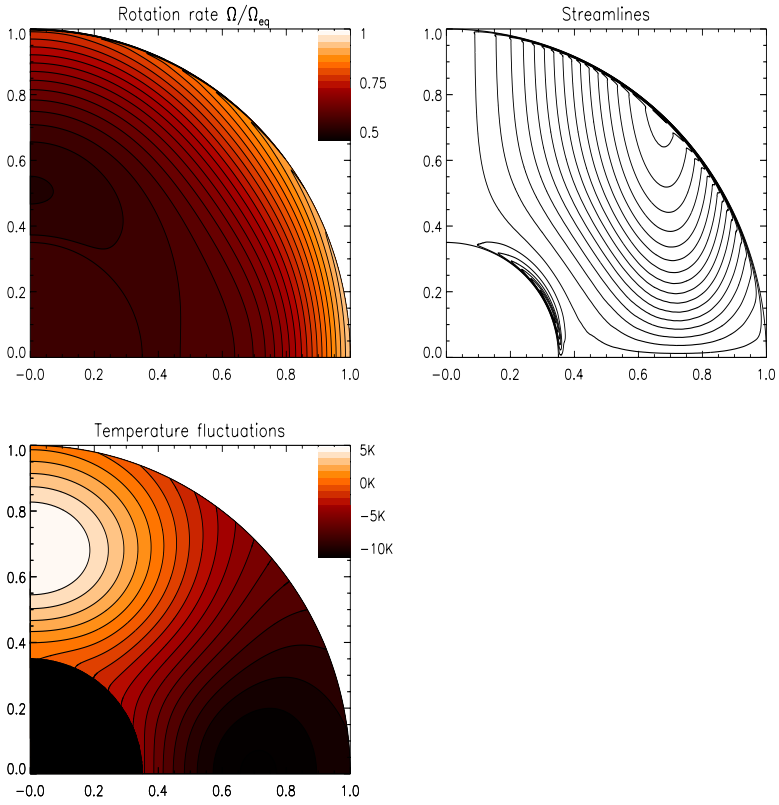

Figure 6.3: Solution to the non-magnetic case described in Section 6.2.2 when $E_\nu = 5 \times 10^{-6}$.

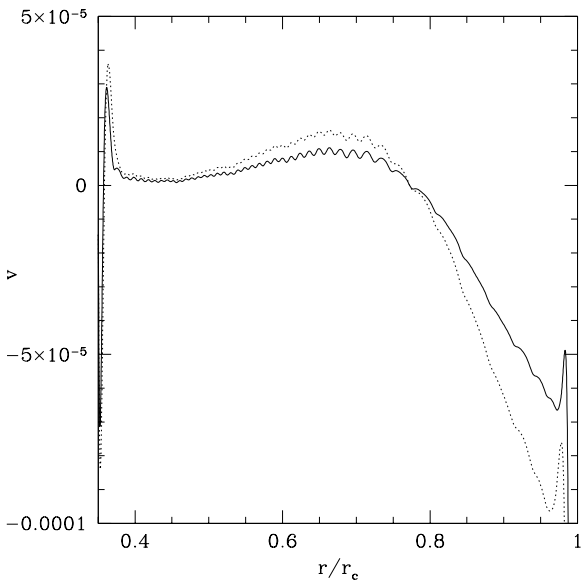

Figure 6.4: Comparison of the variation with radius of the latitudinal velocities obtained in the compressible (solid line) and incompressible (dotted line) simulations at the angular position ($\mu = 0.3$) and for the same Ekman number. The oscillations observed in both cases are well resolved radially; these could be due to lack of latitudinal resolution, which affects the meridional motions in particular (see Section 5.1.4).

more limited to be parallel to the rotation axis. In the vorticity equation, viscous forces are negligible except in the Ekman layers near each boundary; the thermal-wind driving term balances the Coriolis stresses. The meridional circulation runs anticlockwise, burying into the radiative zone near the poles and emerging near the equator. In the downwelling regions, the flow diverges from the pole conserving angular momentum, hence slowing down considerably in the azimuthal direction. Near the bottom of the radiative zone it imposes its slow rotation to the inner core (which is found to be rotating with a value of about a half of the surface equatorial value). As the flow emerges from the deep interior towards the surface near the equator, it is extremely slow both in the radial and azimuthal direction. Viscous stresses have ample time to accelerate the flow to finally match its angular velocity to that of the surface rotation profile. The temperature profile is as expected: the meridional circulation, burrowing into the radiative zone, brings lighter (and therefore hotter) fluid into it, and as it emerges near the equator, brings heavier (and therefore cooler) fluid to higher radii.

Despite the high heat diffusivity of the simulations, this model is more likely to represent the dynamics of a self-gravitating, stratified, rotating fluid than the one presented in the previous section. Moreover, it is found to be easier to converge the solutions to progressively lower Ekman numbers (and heat conductivities) than when the heat conductivity is fixed to its actual solar value. As a result of this analysis, the second method (fixed Prandtl number) is preferred from now on to the first one (fixed heat conductivity) for the study of the effects of heat transport and stratification on the rotation of the sun.

6.3 Results in the magnetic case

As in the incompressible case, the interaction between fluid motions and a large-scale magnetic field depends essentially on the Elsasser number Λ. For consistency with the previous chapters,

the same definition is kept for the Elsasser number:

$$\Lambda = \frac{B_0^2}{r_c^2 \Omega_c^2} \ . \tag{6.33}$$

However, as it is clear from the MHD equation presented in Section 6.1, the relevant quantity which describes the ratio of the magnetic to Coriolis forces is now $\Lambda_c = \Lambda/\rho_c$, where, for consistency, ρ_c is chosen to be the value of the hydrostatic equilibrium density on the boundary with the inner core. As the density of the background decreases with increasing radius between r_{in} and r_{out} roughly as $\rho_h \propto r^{-5}$, the local Elsasser number of the flow $\Lambda_{loc} = B^2/\rho_h r_c^2 \Omega_c^2$ typically varies as $1/r$, instead of $1/r^6$ in the incompressible case. It is therefore difficult to compare directly the results of the incompressible case to those obtained in the compressible case quantitatively. Two cases will however be analysed: $\Lambda_c = 1/500$, $\Lambda_c = 1/20$.

6.3.1 The high-field case, $\Lambda_c = 1/20$

This first simulation is shown in Fig. 6.5, which presents the result in the case of a high Elsasser number. This corresponds to $B_0 = 1.3$ T. The local Elsasser number near the surface is of order of 2×10^{-2} (which is a factor of 10 larger than the surface Elsasser number for the same interior field strength in the incompressible case).

In the high field case, as expected, the system is dominated by magnetic stresses and follows more or less Ferraro iso-rotation. The magnetic field lines are slightly distorted by meridional advection, but globally retain their dipolar structure throughout the fluid region. As in the incompressible high-field case, a strong equatorial circulation is driven by Ekman-Hartman pumping, and is confined into a thin cell by the magnetic field. This circulation advects angular momentum into the radiative zone, leading to the alterning shear structure described in Sec-

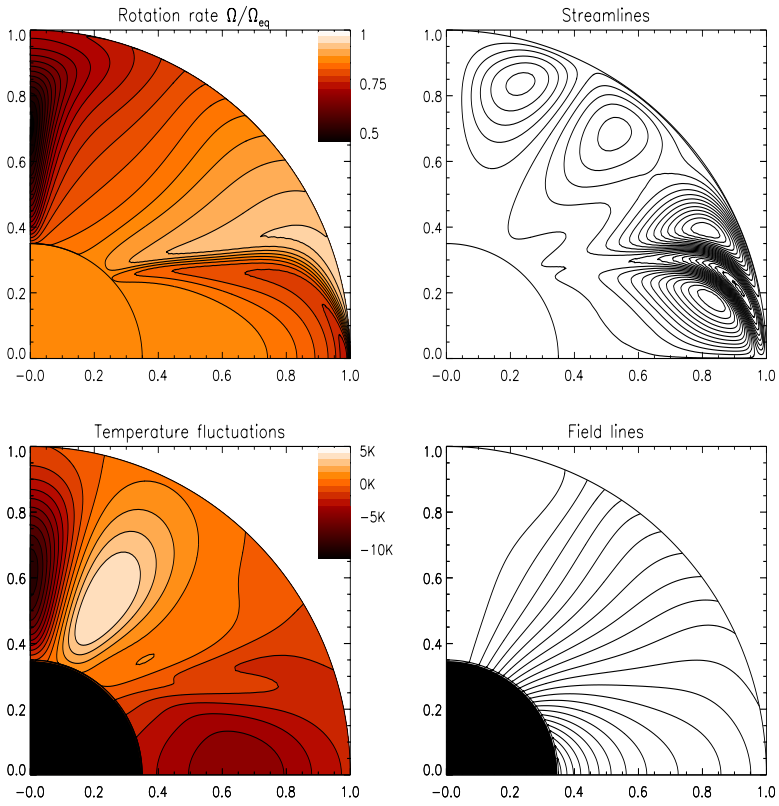

Figure 6.5: Simulation results for $\Lambda_c = 1/20$, $E_\nu = 2.5 \times 10^{-4}$, and $E_\eta = 2.5 \times 10^{-4}$.

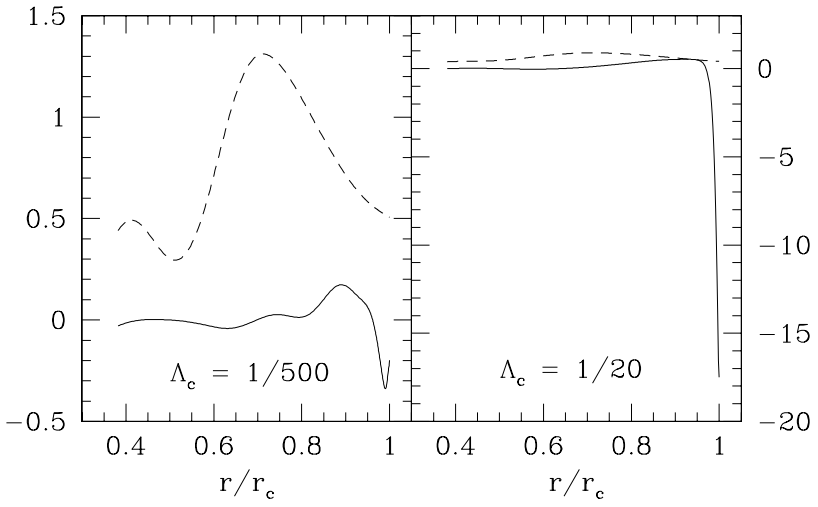

Figure 6.6: Comparison of the variation with radius of the (non-dimensional) thermal-wind term (dashed line) and the magnetic stresses (solid line) at a fixed angular position ($\mu = 0.5$) and fixed Ekman numbers $E_\nu = E_\eta = 2.5 \times 10^{-4}$, for the low-field case (left panel) and the high-field case (right panel).

tion 5.2.1.2 and studied in Section 5.3.2. The dynamics of the system are essentially the same as in the incompressible, high-field case; the principal reason for this similar behaviour is that throughout most of the fluid region, magnetic stresses dominate over thermal-wind driving, and in particular near the surface (see Fig. 6.6). The meridional circulation is not driven, as Gough & McIntyre (1998) suggest, by the thermal wind but rather by Ekman-Hartman pumping on the outer boundary. This obvious discrepancy with the model proposed by Gough & McIntyre stems from the high magnetic field as well as the boundary conditions used in this simulation. The viscous, impermeable walls imposed on the flow and on the magnetic field on the top boundary imply that an Ekman-Hartman layer must develop in which the magnetic stresses largely dominate over thermal-wind driving. In the model proposed by Gough & McIntyre, on the other hand, the circulation is not confined by impermeable walls and can penetrate into the convection zone: in this case, there is no boundary layer, and the principal driving mechanism is the thermal wind.

6.3.2 The low-field case, $\Lambda_c = 1/500$

This second simulation is shown in Fig. 6.7, which presents the result in the case of a low Elsasser number. This corresponds to $B_0 = 0.25$ T. The local Elsasser number near the surface is of order of 7×10^{-4} (which is a factor of 10 larger than the surface Elsasser number for the same interior field strength in the incompressible case).

In this simulation, the dynamics of the system are dominated by thermal-wind driving, which can be seen clearly in Fig. 6.6. Although an Ekman-Hartman layer still subsist near each boundary, thermal-wind driving is more efficient than Ekman-Hartman pumping near the top boundary, and a wholly different structure appears. As predicted by Gough & McIntyre (1998), the circulation pattern driven by thermal-wind effects near the top

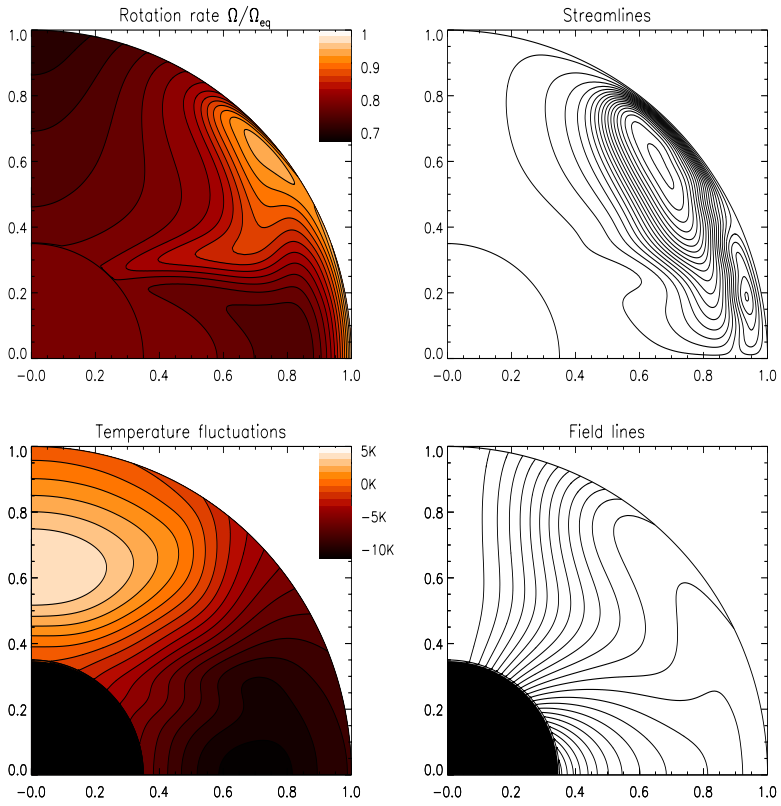

Figure 6.7: Simulation results for $\Lambda_c = 1/500$, $E_\nu = 2.5 \times 10^{-4}$, and $E_\eta = 2.5 \times 10^{-4}$.

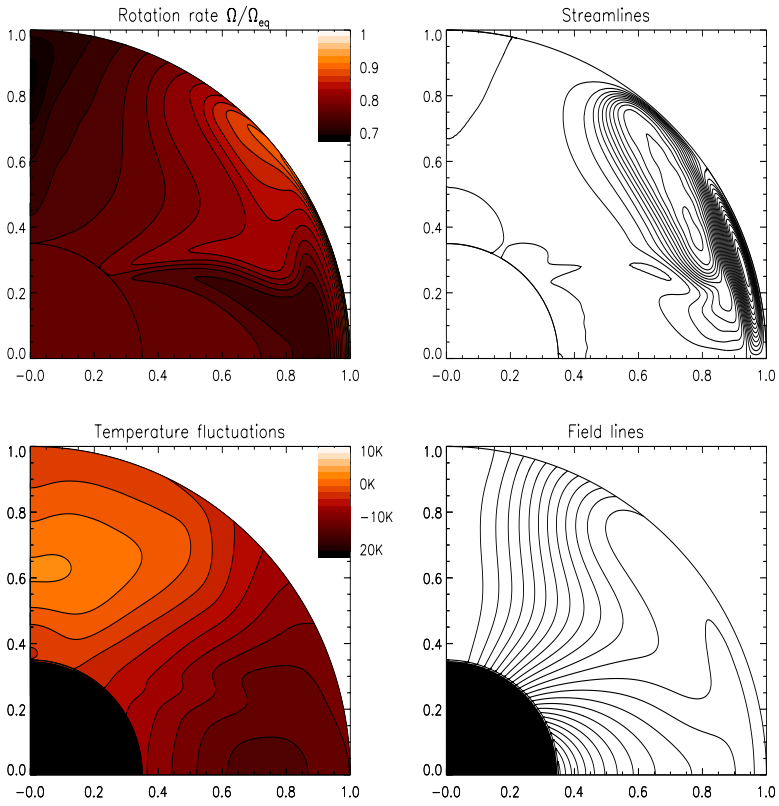

Figure 6.8: Simulation results for $\Lambda_c = 1/500$, $E_\nu = 6.25 \times 10^{-5}$, and $E_\eta = 6.25 \times 10^{-5}$.

of the radiative zone has two cells, with an upwelling region near the surface at mid-latitude. As in Section 5.2.2, this circulation advects the magnetic field away from the boundary, evacuating a shallow region from magnetic flux in the equatorial region. The field in the interior, however, remains strong enough to impose (to some extend) uniform rotation, confining the shear to the magnetic free tachocline. The typical circulation velocities are higher than expected: near the surface, the latitudinal velocity is of order of $10^{-1} r_c \Omega_c$. This is essentially due to the large heat conductivity, which strongly reduces the effects of stratification on radial motions. As before, the structure of the temperature fluctuations can be explained simply by looking at the direction of the meridional flow: at the poles, the downwards flow entrains lighter (hotter) fluid into the radiative zone, whereas at the equator (below the tachocline), the upwelling motion brings denser (colder) fluid from the deep interior to larger radii.

This simulation bears a strong resemblance to the model proposed by Gough & McIntyre, although, as expected from the high diffusivities used in this simulations, the sharpness of the features (thin tachocline, magnetic diffusion layer, upwelling region) cannot be reproduced. In order to acquire some insight as to how the system would behave were the diffusivities reduced to their true solar values, an additional simulation is presented in Fig. 6.8 for $E_\nu = E_\eta = 6.25 \times 10^{-5}$. The results call for the following comments: as in the incompressible case, reducing the magnetic diffusivity increases the connection between the fluid and the field. This enforces a larger region of the fluid to rotate nearly uniformly, and confines the shear to a thinner tachocline. As described in Section 5.2.2, the circulation is confined to shallower layers of the radiative zone in the low-diffusivity case than in the high-diffusivity case. It is interesting to notice that the position of the upwelling region moved from a latitude of about 30° when $E_\eta = 2.5 \times 10^{-4}$ to about 40° when $E_\eta = 6.25 \times 10^{-5}$.

In this Chapter, the effects of stratification, thermal-wind driving and heat transport on the dynamics of the tachocline were studied. Two regimes can be found, which depend essentially on the Elsasser number. When the Elsasser number is large, the system is dominated by Lorentz forces in the momentum equation, and magnetic stresses in the vorticity equation. thermal-wind driving is negligible (in particular close to the boundaries) so that the energy transport equation decouples from the system and the solutions are qualitatively similar to those obtained in the incompressible case.

For a low Elsasser number, however, the thermal wind drives the meridional circulation. In that case, the dynamics of the system are qualitatively very similar to those studied by Gough & McIntyre (1998). However, quantitative predictions are again strongly biased by the high diffusivities used in the simulations. As a result, as in the incompressible case, the radiative zone still sustains some shear in particular near the polar regions and the tachocline is not as thin as observations suggest. The meridional motions are much faster than expected in the tachocline region, due to the abnormally high heat conductivity used in the simulations. Quantitative predictions for the interior rotation rate also fall short of the observations, as can be seen in Fig. 6.9.

As the qualitative results improve, reducing the discrepancy between quantitative predictions from the simulations and observations becomes a priority for future work. The first step towards this goal is obvious: in order to represent more accurately the interaction between magnetic fields and fluid motions in the sun, the abnormally high diffusivities used in the simulations *must* be reduced. In doing so, the typical angular scale and radial scale of variation of all the quantities in the flow is also reduced, which implies that the numerical method of resolution must be capable of resolving smaller and smaller scales. The difficulty in the radial direction consists in the existence of the boundary

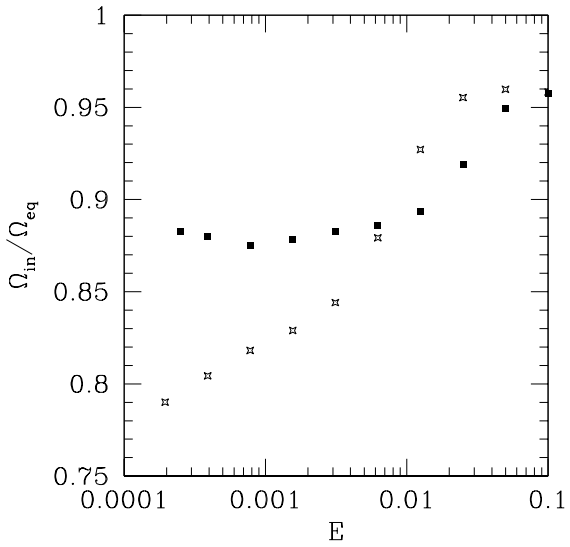

Figure 6.9: Predictions for the interior rotation rate in the high field case (squares) and in the low field case (stars) as a function of the Ekman numbers $E = E_\nu = E_\eta$ of the simulations.

layers on the two spherical boundaries, since their width tend to vary as $\delta \sim (E_\nu E_\eta)^{1/2}$, which corresponds to $\delta \sim 10^{-14} r_c$ in the sun. Jump conditions across these layers may need to be used in further simulations. The principal difficulty, however, lies in the latitudinal direction. As the angular scale of variation is decreased, a gradually larger number of Fourier modes must be kept to avoid numerical instabilities, which increases the memory requirements of the simulations as well as the computer time (both of which tend to increase roughly as N^2). A possible method for reducing this problem would be to project the MHD equations onto a different set of orthogonal functions, which must be chosen carefully to follow more adequately the latitudinal variations of the solution. Another way of improving on quantitative predictions consists in trying to determine a more realistic set of boundary conditions for the system; in particular, the interaction between the convection zone and the tachocline should be carefully modeled.

Conclusion

The work presented in this dissertation reviews and discusses the current state of research on the internal rotation of the sun, focusing in particular on the region of transition between the convection zone and the radiative zone: the tachocline.

Previous models of the solar tachocline failed to represent the dynamical interactions which are thought to be in play in that region of the sun. These models can be separated into two classes: the purely hydrodynamical models, and the MHD models (see Chapters 2 and 3). In the former case, the rapid quenching of the latitudinal shear below the convection zone is thought to be due to the effect of anisotropic Reynolds stresses only (either due to gravity waves, Kumar, Talon & Zahn (1999) or to turbulent motions, Spiegel & Zahn, 1992). This idea stems naturally from the fact that small scale motions in the radiative zone are intrinsically anisotropic, due to the strongly stratified temperature profile in that region. However, there are two principal shortfalls to this idea. Firstly, it has been established that two-dimensional motions transport not angular momentum but potential vorticity (see the review by McIntyre, 1998). This has a tendency to enhance rather than quench any shear. Moreover, although it is likely that gravity waves are indeed excited by the impact of convective motions on the top of radiative zone, it is not yet clear whether the tachocline may or may not undergo fully developed turbulence (Garaud, 2001). Secondly, numerical investigations (Elliott 1997, Dajka & Petrovnay, 2000) have revealed that the typical angular momentum fluxes required to explain the observe thickness of the tachocline are significantly

larger than what could normally be expected from turbulent motions, or gravity waves, below the convection zone. These shortfalls suggest that, although Reynolds stresses may have some effects on the dynamics of the tachocline, other mechanisms must be in play to explain the observed rotational structure of the sun below the convection zone.

The other class of models of the tachocline involves the MHD interaction between fluid motions and large-scale magnetic fields in the radiative interior. The presence of a large-scale poloidal field in the radiative zone provides the most straightforward explanation for the uniform rotation observed deep in the interior and the quenching of the shear observed in the tachocline: Ferraro's theorem states that angular velocity should be constant on field lines in a perfectly conducting fluid, which is nearly the case of the radiative zone. In the hydrodynamical case, the interaction of small scale motions with rotation could be described with ad-hoc models of the Reynolds stresses, which usually lead to a linear problem (provided the non-linear advection terms are small enough). In the MHD case however, the Lorentz force and the advection equations are intrinsically nonlinear: numerical analysis is then the only possible approach. Even with a numerical approach, the problem remains extremely complicated, and many authors still chose to use various degrees of approximation. Rüdiger & Kitchatinov (1997) (and, subsequently, McGregor & Charbonneau, 1999) fixed the poloidal field and neglected the existence of a meridional circulation, which enabled them to solve only the angular momentum equation and the azimuthal component of the advection equation, for the angular velocity and the toroidal field. Their model shows that the shear imposed by the convection zone is indeed quenched by the magnetic field within a small lengthscale which depends essentially on the strength of the magnetic field. Unfortunately, at the heart of the problem is the interaction between the poloidal field and the meridional circulation, which cannot be treated through this approach. Indeed, meridional motions not only ad-

vect the poloidal field, which can therefore not be assumed to be fixed, but also transport angular momentum. This process was illustrated in Chapter 5, where the full incompressible MHD equations are solved: in Section 5.2.1.2 in particular, it is shown how the meridional circulation driven near the base of the convection zone by Ekman-Hartman pumping advects fast rotating fluid into the radiative zone, hereby creating a shear layer at mid-latitudes which persists throughout the radiative zone.

In Chapter 5, I showed that taking into account the interaction between *all* fluid motions (including the circulation) and the magnetic field leads to the emergence of three distinct regimes, which depend on the Elsasser number (the ratio of the magnetic to Coriolis forces), at a fixed value of the magnetic and viscous Ekman numbers. When the Elsasser-number is low, the flow is dominated by the Taylor-Proudman constraint, which enforces a rotation profile roughly constant on cylindrical surfaces. When the Elsasser number is high, the magnetic field imposes uniform rotation in the interior according to the iso-rotation law of Ferraro, and Ekman-Hartman pumping at the top boundary drives a circulation near the equator which redistributes angular momentum along field lines. A shear layer appears in mid-latitude as a result of this meridional motion. In the intermediate-Elsasser-number case, the interior is again rotating nearly uniformly, but the magnetic field is now weak enough to be advected by the equatorial meridional circulation. As a result, instead of being strongly constrained to flow along field lines, the circulation evacuates a region near the top of the radiative zone from magnetic field, pushing poloidal flux deeper into the interior. This region contains most of the shear, and can be likened to the tachocline. Conversely, the circulation is kept from burying into the radiative zone by the accumulation of magnetic flux below the tachocline, which explains why the shear layer observed in the high-Elsasser-number case is now confined to the surface regions. This complex dynamical interaction between the circulation, the rotation and the magnetic

field could not have been predicted through the simplified analysis proposed by Rüdiger & Kitchatinov (1997).

Gough & McIntyre (1998) were the first to stress the importance of thermal-wind driving with respect to the tachocline dynamics. Differential rotation causes the baroclinicity of the flow, which in turns drives a circulation along isopycnal lines to advect the excess heat. They suggested that as the circulation evacuates the tachocline from poloidal magnetic flux, thermal-wind driving would dominate over Ekman-Hartman driving, leading to a two-cell circulation pattern within the tachocline, with an upwelling region in mid-latitudes. The extreme complexity of the dynamics of their model precluded all but a simple boundary layer analysis, which was summarized in Chapter 3. Gough & McIntyre found that the thickness of the tachocline can be uniquely related to the interior field strength as $\Delta \propto B_0^9$, but failed to predict the interior angular velocity as all information depending on the latitudinal variation of the various quantities is lost through the boundary layer approach. In Chapter 6, following their model I proposed the first numerical MHD model of the sun in which heat transport, compressibility and stratification effects can be studied self-consistently (Hujeirat & Yorke (1998) also attempted to study the tachocline dynamics through a similar model, but neglecting heat diffusion, they were forced to consider an adiabatically stratified background as well as adiabatic motions only, which is fundamentally different from what is thought to occur in the tachocline). I have shown that in the "compressible" case it is possible to find a parameter regime for which the results of the simulations follow closely the lines of the model proposed by Gough & McIntyre (1998), at least qualitatively (see Section 6.3.2). The remaining quantitative discrepancy with the observations is principally due to the high diffusivities used in the simulations, but could also be due to the boundary conditions chosen. In the high Elsasser number case for example, it was shown that the magnetic term in the vorticity equation dominates clearly over the thermal wind

term; as a result, the meridional circulation is driven by Ekman-Hartman pumping rather than by thermal-wind driving. This phenomenon is to some extent artificial, since it could be supressed simply by allowing the walls to be permeable (in which case the Ekman-Hartman layer disappears).

This example stresses the importance of the boundary conditions used in the model. The boundary conditions studied in this dissertation have been carefully chosen to represent a model for which a solution is known to exist; they provide a first solution which can be used as a basis for studying the most important phenomena believed to take place in the radiative interior, and also a solution which can be used as a starting point (a guess) for further numerical investigations of more complex boundary conditions. I do not claim that they represent an accurate representation of the interaction between the tachocline and the convection zone. In fact, it is not yet clear observationally whether the tachocline extends into the convection zone or not (Charbonneau et al. 1999). In this dissertation, and for the purpose of the following discussion, it will be assumed that no radial shear is present in the convective zone and that the top of the tachocline coincides with the top of the stably stratified region. In future work, it will be necessary to study carefully the interface between the tachocline and the convection zone in order to determine more realistic boundary conditions. Several aspects of this interface should be kept in mind.

- The convection zone, and to some extend the overshoot region below is the seat of fully developed turbulence. It does not behave as an impermeable wall to the circulation in the tachocline, but rather, perhaps, as a "porous media". In any case, a more realistic model should study the interaction of the circulation with the convective motions, possibly through an ad-hoc Reynolds stresses prescription, as it is suggested by Dajka & Petrovnay (2000), for instance.
- Due to strong mixing by downwelling plumes, the overshoot region is nearly adiabatically stratified, despite being

located in the stably stratified zone. This leads to a singularity in the energy equation, which corresponds to the point at which the buoyancy frequency tends to zero, or in other words, the point near which the inhibition of radial motions due to the stratification vanishes. This singularity was avoided in the simulations presented in Chapters 4 to 6, and to some extent in all other works related to the tachocline, by placing the tachocline safely *below* the overshoot region. As the width of the overshoot region has not yet been successfully determined observationally, it is by default a reasonable assumption. However this assumption needs to be studied more carefully by future analyses.

- Finally, the boundary conditions for the magnetic field need to be carefully studied; in the simulations presented above, it was simply assumed that the convective zone behaves as a conducting media with the same conductivity as the radiative zone (to avoid current sheets on the boundary). This is clearly the simplest type of boundary condition, but fails to represent the complexity of the interaction between the convective motions and the magnetic field. It is for example widely believed that the interface of the tachocline and the convection zone is the seat of the solar dynamo, which is a non-steady magnetic structure oscillating between two configurations of opposite polarity in a 22 years cycle. How can this structure be matched with the assumed steady, nearly dipolar field of the interior?

This final point also raises one of the major issues of the dynamics of the tachocline: to which extent can a steady model represent the system? This question raises several issues. Firstly, how can the interior field be represented by a steady field when part of it diffuses, or is advected away into the convection zone? The diffusion of the magnetic field out of the radiative zone is impeded by the confining action of the circulation on the poloidal field, which supports the steady-state assumption. However, the upwelling region discussed by Gough & McIntyre drags the poloidal magnetic field into the convection zone, where it oc-

casionally reconnects. This phenomenon is intrinsically non-steady, although possibly quasi-periodic. Secondly, the hydrodynamical stability of the solution to various instabilities should be assessed. The stability of the shear flow tends to be upset by the presence of a magnetic field, as suggested by Gilman & Fox (1997). In a stratified fluid, the buoyancy of toroidal flux tubes may lead to a magneto-convective instability. Finally, Alfvèn waves can propagate along the magnetic field and lead to the presence of either "localized" oscillations, or global torsional oscillations. Observational studies of the evolution with time of the structure of the shear below the convection zone have revealed an oscillatory pattern near the equator, with opposite phases below and above the tachocline (Howe et al. 2000). It is not yet clear whether this study is evidence for a true oscillation of the solar rotational structure, or an artefact of the inversion processes. However, the observed oscillation period is of order of 1.3 yr; the typical period of oscillation of global torsional Alfvèn waves in that region being $\tau = \lambda\sqrt{\rho}/B$, where λ is the typical lengthscale of oscillation, the amplitude of the magnetic field required to explain the presence of these waves is of order of 1 kG (Gough, 2000). The values obtained for the amplitude of the magnetic field in the tachocline are not unreasonable and correspond both to current estimates (Schüssler et al. 1994) and to the typical values used in my simulations.

Finally the long-term evolution of the sun may also affect the structure of the tachocline, for two principal reasons: the solar spin-down and the decay of the interior field. It is not clear from the simulations whether, as Gough & McIntyre suggest, the magnetic field is essentially well contained within the radiative zone (expect, maybe in the upwelling region) and kept from diffusing outwards, or whether magnetic flux is allowed to escape from the "polar" regions. According to Gough & McIntyre, however, the thickness of the tachocline varies little with the amplitude of the magnetic field, so for the sake of the following argument, this amplitude can be assumed to be constant.

The solar rotation rate is proportional to $t^{-1/2}$, according to the Skumanich law (Skumanich, 1972), which implies that the young sun was not only rotating much faster than now, but also that the braking timescale was much shorter than today. A faster rotating sun implies on the one hand a different latitudinal shear in the convection zone (i.e. different boundary conditions for the tachocline), and on the other hand stronger thermal wind driving at the top of the radiative zone. The effects of a different latitudinal rotation profile at the top boundary are unlikely to change the results qualitatively, but the effect of stronger driving is to increase the thickness of the tachocline. As the braking timescale decreases, the total magnetic torque applied by the convection zone on the radiative zone may not be negligible any more, and the steady state analysis may be invalidated. The effect of such braking would be to accelerate the meridional circulation through Ekman pumping within the tachocline – but this effect should remain small due to the low Ekman numbers. As a result, MHD models (Gough & McIntyre, 1998, as well as the simulations presented in Chapters 4 to 6) predict a thicker tachocline for the young sun than the present sun. This may have significant influence on light-element mixing (see Brun, Turck-Chièze & Zahn (1999)).

To conclude, although the dynamical behaviour of the sun is likely to be far more complex than that of the simulations presented in this dissertation, I believe that these simulations can grasp, and explain, some of the *fundamental* aspects of the dynamics of the observed solar differential rotation. Moreover, they lay a strong basis for future improvements of the models along the lines described above, that I (and others, perhaps) will strive to develop.

Appendix A

Commonly used solar parameters

All quantities used in this dissertation are in *cgs* unis.

The following universal constants are used:

- the gravitational constant $G = 6.672 \times 10^{-8}$ dyne-cm^2/g^2,
- the Stefan-Boltzmann constant $\sigma_{\rm B} = 5.67 \times 10^{-5}$ erg/cm^2.

The parameters most commonly used in this work are the following, with the corresponding values used in all calculations:

- the solar radius: $r_\odot = 6.96 \times 10^{10}$ cm,
- the solar mass: $M_\odot = 1.99 \times 10^{33}$ g,
- the radius of the solar convection zone (as derived by Christensen-Dalsgaard *et al.* (1991)): $r_{\rm c} = 0.713 r_\odot$,
- the depth of the solar tachocline (as derived by Elliott & Gough (1999)): $\Delta = 0.02 r_\odot$,
- the value of the angular velocity of the radiative interior: $\Omega_{\rm c}/2\pi = 430$ nHz.

In most of the models proposed, the dynamical structure of the tachocline is treated as a perturbation on the background hydrostatic equilibrium state. For this reason, the variation with depth of various hydrostatic equilibrium quantities needs to be known (see Fig.A.1), as well as an average value of these quantities within the tachocline (see Table A.1).

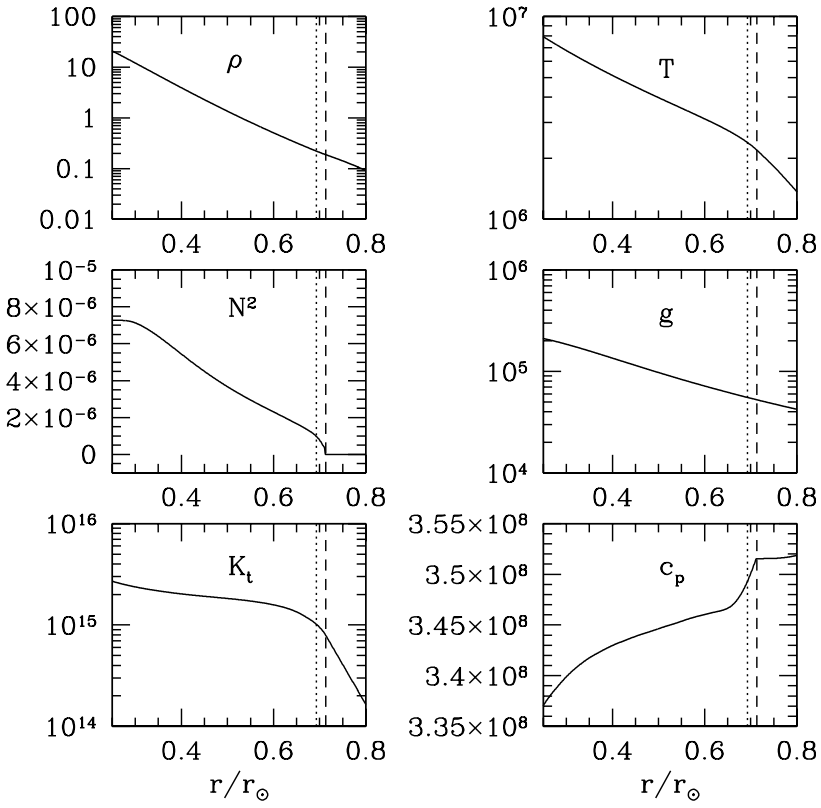

Figure A.1: Variation of the following hydrostatic equilibrium quantities with radius: the density ρ (in g/cm^3), the temperature T (in K), the square of the buoyancy frequency N^2 (in s^{-2}), the gravitational attraction g (in cm s^{-2}), the thermal conductivity K_t (in erg s^{-1} K^{-1} cm^{-}1) and the heat capacity $c_{\rm p}$ (in erg g^{-1} K^{-1}). The dashed line represents the position of the bottom of the convection zone as calculated by Christensen-Dalsgaard *et al.* (1991) and the dotted line marks the lower edge of the tachocline, using the width of the tachocline derived by Elliott & Gough (1999).

ρ	0.2
T	2.2×10^6
N^2	10^{-6}
g	5.5×10^4
K_t	10^{15}
$c_{\rm p}$	3.5×10^8

Table A.1: Average values of the following hydrostatic equilibrium quantities with radius: the density ρ (in g/cm^3), the temperature T (in K), the square of the buoyancy frequency N^2 (in s^{-2}), the gravitational attraction g (in cm s^{-2}), the thermal conductivity K_t (in erg s^{-1} K^{-1} cm^{-1}) and the heat capacity $c_{\rm p}$ (in erg g^{-1} K^{-1}).

Appendix B

Miscellaneous Chebischev Polynomials formulae

B.1 Basic Formulae

Definitions, multiplications:

$$T_m(\mu) = T_m(\cos\theta) = \cos(m\theta)\ , \tag{B.1}$$

$$T_{-m}(\mu) = T_m(\mu) \text{ by definition,} \tag{B.2}$$

$$2T_m(\mu)T_n(\mu) = T_{m+n}(\mu) + T_{m-n}(\mu)\ . \tag{B.3}$$

Projection:

$$\int_{-1}^{1} \frac{T_n(\mu)T_m(\mu)}{\sqrt{1-\mu^2}}\mathrm{d}\mu = \frac{\pi}{2}\delta_{n,m} + \frac{\pi}{2}\delta_{n,m}\delta_{n,0}\ . \tag{B.4}$$

First few polynomials:

$$T_0 = 1\ ,\ T_1 = \mu\ ,\ T_2 = 1+\mu^2\ , \tag{B.5}$$

$$1-\mu^2 = \frac{1}{2}(T_0 - T_2)\ . \tag{B.6}$$

Commonly used product:

$$(1-\mu^2)T_n = \frac{T_n}{2} - \frac{T_{n+2}}{4} - \frac{T_{n-2}}{4}\ . \tag{B.7}$$

B.2 Commonly used differentiation formulae

$$(1-\mu^2)\frac{\partial T_n}{\partial \mu} = \frac{n}{2}(T_{n-1}-T_{n+1}) \ , \tag{B.8}$$

$$\frac{\partial}{\partial \mu}\left[(1-\mu^2)T_n\right] = \frac{n-2}{2}T_{n-1}-\frac{n+2}{2}T_{n+1} \ . \tag{B.9}$$

B.3 Usefull projection formulae

B.3.1 Calculation of $C_{k,n}$

where

$$C_{k,n} = \int_0^\pi \cos(k\theta)\,\cos^n\theta \mathrm{d}\theta \tag{B.10}$$

for $n > 0$.

$$C_{k,n} = \int_0^\pi \frac{\cos(k\theta)}{2^n}\left[C^n_{\frac{n}{2}} + 2\sum_{j=1}^{n}\cos(j\theta)C^n_{\frac{n+j}{2}}\right]\mathrm{d}\theta \tag{B.11}$$

$$= \begin{cases} \frac{1}{2^n}C^n_{\frac{n}{2}} & \text{if } k=0, \\ \frac{1}{2^n}C^n_{\frac{n+|k|}{2}} & \text{if } 0<|k|\leq n. \end{cases} \tag{B.12}$$

B.3.2 Calculation of $B_{k,n}$

where

$$B_{k,n} = \int_{-1}^{1}\frac{T_k}{\sqrt{1-\mu^2}}\frac{\mathrm{d}T_n}{\mathrm{d}\mu}\mathrm{d}\mu \ . \tag{B.13}$$

Rewriting this using θ yields

$$B_{k,n} = n\int_0^\pi \cos(k\theta)\frac{\sin(n\theta)}{\sin\theta}\mathrm{d}\theta \ . \tag{B.14}$$

Now use

$$\begin{aligned}
\sin(n\theta) &= \sin((n-1)\theta)\,\cos\theta + \sin\theta\,\cos((n-1)\theta) \\
&= \sin((n-2)\theta)\,\cos^2\theta \\
&+ \sin\theta\,[\,\cos\theta\,\cos((n-2)\theta + \cos((n-1)\theta)] \\
&= \ldots \\
&= \sin\theta\left[\sum_{p=1}^{n}\cos((n-p)\theta)\,\cos^{p-1}\theta\right] , \qquad \text{(B.15)}
\end{aligned}$$

so that

$$\begin{aligned}
B_{k,n} &= \frac{n}{2}\int_0^\pi \left[\sum_{p=1}^{n}\cos((n-p+k)\theta)\,\cos^{p-1}\theta\right. \\
&+ \left.\sum_{p=1}^{n}\cos((n-p-k)\theta)\,\cos^{p-1}\theta\right]\mathrm{d}\theta \\
&= \frac{n}{2}\sum_{p=1}^{n}\left(C_{k+n-p,p-1} + C_{k+p-n,p-1}\right) . \qquad \text{(B.16)}
\end{aligned}$$

B.3.3 Calculation of $A_{k,n}$

where

$$A_{k,n} = \int_{-1}^{1}\frac{T_k(\mu)}{\sqrt{1-\mu^2}}\frac{\mathrm{d}^2}{\mathrm{d}\mu^2}\left((1-\mu^2)T_m(\mu)\right)\mathrm{d}\mu . \qquad \text{(B.17)}$$

$$\begin{aligned}
A_{k,n} &= \int_{-1}^{1}\frac{T_k(\mu)}{\sqrt{1-\mu^2}}\frac{\mathrm{d}}{\mathrm{d}\mu}\left[\frac{m-2}{2}T_{m-2} - \frac{m+2}{2}T_{m+1}\right]\mathrm{d}\mu \\
&= \frac{m-2}{2}B_{k,m-1} - \frac{m+2}{2}B_{k,m+1} . \qquad \text{(B.18)}
\end{aligned}$$

B.3.4 Calculation of $I_{k,n}$

where

$$I_{k,n} = \int_{-1}^{1} P_k(\mu) T_n(\mu) \mathrm{d}\mu \ , \tag{B.19}$$

where $P_k(\mu)$ is the Legendre polynomial of order k. The following relation holds:

$$P_k(\ \cos\theta) = \frac{1}{4^k} \sum_{p=0}^{k} C_p^{2p} C_{k-p}^{2k-2p} \ \cos((k-2p)\theta) \ , \tag{B.20}$$

so that

$$\begin{aligned} I_{k,n} =& \frac{1}{4^k} \sum_{p=0}^{k} \int_0^{\pi} \ \cos(n\theta) \ \sin\theta C_p^{2p} C_{k-p}^{2k-2p} \ \cos((k-2p)\theta) \mathrm{d}\theta \\ =& \frac{1}{4^{k+1}} \sum_{p=0}^{k} C_p^{2p} C_{k-p}^{2k-2p} \left[\frac{(-1)^{1+n+k-2p} - 1}{1+n+k-2p} + \frac{(-1)^{1+n+2p-k} - 1}{1+n+2p-k} \right. \\ &+ \left. \frac{(-1)^{1-n+k-2p} - 1}{1-n+k-2p} + \frac{(-1)^{1-n+2p-k} - 1}{1-n+2p-k} \right] \ . \end{aligned} \tag{B.21}$$

Of course, C_n^k is only defined when n is an integer smaller than k. Otherwise, it is null.

B.3.5 Calculation of $D_{k,n}$

where

$$D_{k,n} = \int_{-1}^{1} P_k(\mu) \frac{\mathrm{d}}{\mathrm{d}\mu} \left((1-\mu^2) T_n(\mu) \right) \mathrm{d}\mu \ . \tag{B.22}$$

Using the differentiation relations it is easy to obtain

$$D_{k,n} = \frac{n-2}{2} I_{k,n-1} - \frac{n+2}{2} I_{k,n+1} \ . \tag{B.23}$$

where

$$\gamma_m = \int_{-1}^{1} T_m(\mu)(1-\mu^2)\mathrm{d}\mu \ . \tag{B.24}$$

Using the definition of $I_{k,n}$ it is easy to get

$$\gamma_m = \frac{2}{3}\int_{-1}^{1} T_m(\mu)(P_0(\mu) - P_2(\mu))\mathrm{d}\mu = \frac{2}{3}(I_{0,m} - I_{2,m}) \ . \tag{B.25}$$

Bibliography

Andrews, D. G., Holton, J. R., Leovy, C. B., 1987, *Middle Atmosphere Dyna mics*, Academic Press Inc.

Abramowitz, M & Stegun, I. A., 1972, *Handbook of Mathematical Functions*, ed. Wiley Interscience Publications

Acheson, D. J. & Hide, R., 1973, Rep. Prog. Phys., 36, 159

Basu, S., 1997, MNRAS, 288, 572

Boruta, N., 1996, ApJ, 458, 832

Brown, T. M., Christensen-Dalsgaard, J., Dziembowski, W. A.,Goode, P., Gough, D. O. & Morrow, C. A., 1989, ApJ, 343, 526

Brun, A. S., Turck-Chièze, S., & Zahn, J.-P., 1999, ApJ, 525, 1032

Carslaw, H. S., Jaeger, J. C., 1959, *Conduction of heat in solids*, (Oxford University Press)

Carrington, R. C., 1863, *Observations of the Spots on the Sun from November 9, 1853, to March 24, 1861, made at Redhill*, ed. William & Norgate

Chandrasekhar, S., 1956, ApJ, 124, 244

Chaplin W.J., Elsworth Y., Isaak G.R., Miller B.A., New R., 2000, MNRAS, 313, 32

Charbonneau, P., Christensen-Dalsgaarg, J., Henning, R., Larsen, R. M., Schou, J., Thompson, M. J., & Tomczyk, S., 1999, ApJ, 527, 445

Charbonneau, P., Dikpati, M., Gilman, P. A., 1999, ApJ, 528, 523

Christensen-Dalsgaard, J. et al., 1996, Science, 272, 1286

Christensen-Dalsgaard, J., Gough, D. O. & Thompson, M. J., 1991, ApJ, 378, 413

Corbard, T., Berthomieu, G., Provost, J. & Morel, P., 1998, A&A, 330, 1149

Cowling, T. G., 1957, *Magnetohydrodynamics* (Interscience, New York)

Cowling, T. G. & Newing, R. A., 1948, MNRAS, 109, 149

Dajka, E., & Petrovnay, K., 2000, in *Proceedings of the SOHO-10/GONG-2000 conference on Helio- and Asteroseismology at the dawn of the Millennium*, ESA Publications.

Däppen, W. & Nayfonov, A., 2000, ApJ Supp. Ser., 127, 287

Dormy, E., Cardin, P. & Jault, D., 1998, Earth & Planetary Sci. Letters, 160, 15

Drazin, P.G., Ried, W.H., 1981, *Hydrodynamical Stability*, C.U.P.

Dudorov, A. E., et al., 1989, Astr. Zhurn., 66, 809

Duvall, T. L. Jr., Dziembowski, W. A., Goode, P. R., Gough, D. O., Harvey, J. W. & Leibacher, J. W., 1984, Nature, 310, 22

Duvall, T. L. Jr. & Harvey, J. W., 1984, Nature, 310, 19

Dziembowski, W., Kosovichev, A., 1987, Acta Astron., 37, 341

Eddington, A. S., 1926, *The internal constitution of the stars*, CUP

Elliott, J. R., 1996, PhD Thesis

Elliott, J. R., 1997, A&A, 327, 1222

Elliot, J. R., Gough, D. O., 1999, ApJ, 516, 475

Ferraro, V. C. A., 1937, MNRAS, 97, 458

Garaud, P. 1999, MNRAS, 304, 583

Garaud, P., 2001, MNRAS, *in press*

Gilman, P. A. & Fox, P. A., 1997, ApJ, 484, 439

Gough, D. O., 1985, Solar Phys., 100, 65

Gough, D. O., 1997, Nature, 388, 324

Gough, D. O., 2000, Science, 287, 2434

Gough, D. O., et al., 1996, Science, 272, 1296

Gough, D. O. & Kosovichev, A. G., 1995, *Proceedings of the 4th SOHO Workshop, Pacific Grove, California, 1995*, ESA SP-376

Gough, D. O., McIntyre, M. E., 1998, Nature, 394, 755

Gough, D. O., Spiegel, E. A. & Toomre, J., 1974, Lecture Notes in Phys., 35, 191

Gough, D. O., & Thompson, M. J., 1991, *Solar interior and atmosphere* (ed. A.N. Cox, W.C. Livingston and M.S. Matthews, Univ. Arizona Press, Tucson), pp. 519

Haynes, P. H., 1989, JFM, 207, 231

Hinata, S., 1986, A&A, 169, 161-163

Houdek G., Chaplin W.J., Appourchaux T., Christensen-Dalsgaard J., Däppen W., Elsworth Y., Gough D.O., Isaak G.R., News R., Rabello-Soares M.C., 2001, MNRAS, *submitted*

Howe, R., Basu, S., Christensen-Dalsgaard, J., Hill, F., Komm, R. W., Larsen, R. M., Schou, J., Thompson, M. J. & Toomre, J., 2000, *Proceedings of the SOHO-10/GONG-2000 conference on Helio- and Asteroseismology at the dawn of the Millennium*, ESA Publications.

Howe, R., Christensen-Dalsgaard, J., Hill, F., Komm, R. W., Larsen, R. M., Schou, J., Thompson, M. J. & Toomre, J., 2000, Science, 287, 2456

Hujeirat, A. & Yorke, H. W., 1998, New Astronomy, 3, 671

Killworth, P. D., McIntyre, M. E., 1985, JFM, 161, 449

Kitchatinov, L. L. & Rüdiger, G., 1993, A&A, 276, 96

Kumar, P., Quataert, E. J., 1997, ApJ, 475, L143

Kumar, P., Talon, S., Zahn, J.-P., 1999, ApJ, 520, 859

Ledoux, P., 1951, ApJ, 114, 373

Ledoux, P. & Perekis, C. L., 1941, ApJ, 94, 124

Leighton, R. B., Noyes, R. W., Simon, G. W., 1962, ApJ, 135,474

Lord Rayleigh, 1880, Proc. London Math. Soc., 11, 57

Lynden-Bell, D. & Ostricker, J. P. 1967, MNRAS, 136, 293

MacGregor, K.B., Charbonneau, P., 1999, ApJ, 519, 911

Matsuno, T., 1971, J. Atmos. Sci., 28, 1479

McIntyre, M. E., 1998, Progress in Theo. Phys., 130, 137

Mestel, L., 1953, MNRAS, 113, 716

Mestel, L., Moss, D. L., 1983, MNRAS, 204, 575

Mestel, L., Weiss, N. O., 1987, MNRAS, 226, 123

Miesch, M. S., et al., 2000, ApJ, 532, 593

Moreau, R., 1990, *Magnetohydrodynamics*, ed. Kluwer pp. 313

Morel, P., Pichon, B., Provost, J. & Berthomieu, G., 1999, A&A, 350, 275

Newton, H. W. & Nunn, M. L., 1951, MNRAS, 111, 413

Parker, E. N., 1993, ApJ, 408, 707

Plumb, R. A. & McEwan, A. D., 1978, J. Atmos. Sci., 35, 1827

Proudman, I., 1956, JFM, 1, 505

Ross, J. E. & Aller, L. H., 1976, Science, 191, 1223

Rüdiger, G., Kitchatinov, L. L., 1997, Astr. Nachr. 318, 273

Schatzman, E., 1993, A&A, 279, 431

Schou, J., Christensen-Dalsgaard, J. & Thompson, M. J., 1994, ApJ, 433, 389

Schou, J., Kosovichev, A.G., Goode, P.R. & Dziembowski, W.A., 1997, ApJ, 489, L197

Schou, J. et al., 1998, ApJ, 505, 390

Schüssler, M., Caligari, P., Ferriz-Mas, A., Moreno-Insertis, F., 1994, A&A, 281, L69-L72

Skumanich, A., 1972, ApJ, 171, 565

Snodgrass, H. B., 1984, Solar Phys., 94, 13

Spiegel, E. A., Zahn, J.-P., 1992, A&A, 265, 106

Spitzer, L., 1962, *Physics of fully ionized gases* (Interscience, New York).

Stewartson, K., 1966, JFM, 26, 131

Stix, M., 1989, *The Sun, an Introduction*, (Springer Verlag).

Sweet, E., 1950, MNRAS, 110, 548

Thompson, M. J., et al., 1996, Science, 272, 1301

Tobias, S. M., et al., 1998, ApJ, 502, L177

Tripathy, S. C. & Christensen-Dalsgaard, J., 1998, A&A, 337, 579

Watson, M., 1981, GAFD, 161, 285

Weiss, N.O., 1994, in *Lectures on Solar and Planetary Dynamos*, ed. M.R.E. Proctor & A.D. Gilbert, pp. 59, CUP.

Weiss, N.O., 1996, *Magnetohydrodynamic Phenomena in the Solar Atmosphere - Prototypes of stellar magnetic activity*, (Kluwer Academic Publishers) 387

Zahn, J.-P., Talon, S., Matias, J., 1997, A&A, 322, 320